COPPE
Instituto Alberto Luiz Coimbra de Pós-Graduação e Pesquisa de Engenharia
UFRJ

EFFECT OF FLOW ON THE CORROSION BEHAVIOUR OF API 5L X80 STEEL IN SUPERCRITICAL CO_2 SYSTEMS

Jonas da Silva de Sá

Tese de Doutorado apresentada ao Programa de Pós-graduação em Engenharia Metalúrgica e de Materiais, COPPE, da Universidade Federal do Rio de Janeiro, como parte dos requisitos necessários à obtenção do título de Doutor em Engenharia Metalúrgica e de Materiais.

Orientadores: José Antônio da Cunha
Ponciano Gomes
Richard Barker

Rio de Janeiro
Março de 2022

EFFECT OF FLOW ON THE CORROSION BEHAVIOUR OF API 5L X80 STEEL IN SUPERCRITICAL CO_2 SYSTEMS

Jonas da Silva de Sá

TESE SUBMETIDA AO CORPO DOCENTE DO INSTITUTO ALBERTO LUIZ COIMBRA DE PÓS-GRADUAÇÃO E PESQUISA DE ENGENHARIA DA UNIVERSIDADE FEDERAL DO RIO DE JANEIRO COMO PARTE DOS REQUISITOS NECESSÁRIOS PARA A OBTENÇÃO DO GRAU DE DOUTOR EM CIÊNCIAS EM ENGENHARIA METALÚRGICA E DE MATERIAIS.

Orientadores: José Antônio da Cunha Ponciano Gomes
Richard Barker

Aprovada por: Prof. José Antônio da Cunha Ponciano Gomes
Prof. Richard Barker
Prof. Achilles Junqueira Bourdot Dutra
Prof. Alysson Helton Santos Bueno
Prof. Hamilton Ferreira Gomes de Abreu

RIO DE JANEIRO, RJ – BRASIL
MARÇO DE 2022

Sá, Jonas da Silva de

Effect of flow on the corrosion behaviour of API 5L X80 steel in supercritical CO_2 systems/Jonas da Silva de Sá. – Rio de Janeiro: UFRJ/COPPE, 2022.

XIV, 88 p.: il.; 29, 7cm.

Orientadores: José Antônio da Cunha Ponciano Gomes
Richard Barker

Tese (doutorado) – UFRJ/COPPE/Programa de Engenharia Metalúrgica e de Materiais, 2022.

Referências Bibliográficas: p. 77 – 88.

1. dióxido de carbono. 2. fluido supercrítico. 3. corrosão. 4. aço carbono. I. Gomes, José Antônio da Cunha Ponciano *et al.* II. Universidade Federal do Rio de Janeiro, COPPE, Programa de Engenharia Metalúrgica e de Materiais. III. Título.

Resumo da Tese apresentada à COPPE/UFRJ como parte dos requisitos necessários para a obtenção do grau de Doutor em Ciências (D.Sc.)

EFEITO DO FLUXO NA CORROSÃO DO AÇO API 5L X80 EM MEIOS DE CO_2 SUPERCRÍTICO

Jonas da Silva de Sá

Março/2022

Orientadores: José Antônio da Cunha Ponciano Gomes
Richard Barker

Programa: Engenharia Metalúrgica e de Materiais

Neste trabalho, foi investigado o efeito do fluxo de CO_2 supercrítico e do fluxo de água saturada de CO_2 na corrosão do aço API 5L X80 a uma temperatura de 35 ^{o}C e pressão de 80 bar. Os testes foram realizados com as amostras presas a um eixo giratório dentro de uma autoclave. Os resultados indicam que aumentar o fluxo de água saturada de CO_2 elevou a taxa inicial de corrosão, mas posteriormente favoreceu a precipitação de uma camada de carbonato cristalino densa e mais protetora. Além disso, a presença de Ca^{2+} na água favoreceu a precipitação de um filme misto de carbonato de ferro-cálcio ($Fe_xCa_{1-x}CO_3$) que ofereceu melhor proteção ao aço carbono quando comparado ao carbonato de ferro puro ($FeCO_3$). Por outro lado, em sistemas de dióxido de carbono supercrítico, o aumento do fluxo não teve influência significativa nas taxas de corrosão uniforme/localizada nas diferentes condições consideradas, pois o tamanho das gotas de água condensada era muito menor do que o tamanho crítico de gota calculado necessário para ser deslocado pelo fluxo de CO_2 supercrítico.

Abstract of Thesis presented to COPPE/UFRJ as a partial fulfillment of the requirements for the degree of Doctor of Science (D.Sc.)

EFFECT OF FLOW ON THE CORROSION BEHAVIOUR OF API 5L X80 STEEL IN SUPERCRITICAL CO_2 SYSTEMS

Jonas da Silva de Sá

March/2022

Advisors: José Antônio da Cunha Ponciano Gomes
Richard Barker

Department: Metallurgical and Materials Engineering

In this work,the effect of water-saturated supercritical CO_2 and CO_2-saturated water flow rate on the corrosion behaviour of API 5L X80 steel at a temperature of 35 ^{o}C and pressure of 80 bar was investigated. Tests were carried out with the samples attached to a rotating shaft inside an autoclave. Results indicate that increasing the CO_2-saturated water flow rate increased the corrosion rate in the absence of a corrosion product film, but later favoured the precipitation of a dense and more protective crystalline carbonate layer. Besides that, the presence of Ca^{2+} in the brine favoured the precipitation of a mixed iron-calcium carbonate ($Fe_xCa_{1-x}CO_3$) film with increasingly calcium molar mass that offered better protectiveness to the carbon steel when compared to the pure iron carbonate ($FeCO_3$). On the other hand, in water-saturated supercritical carbon dioxide systems, increasing the flow rate had no significant influence on the general/localized corrosion rate under the various dynamic conditions considered, because the size of the condensed water droplets, were much smaller than the calculated critical droplet size needed to be displaced by the supercritical CO_2 flow.

Contents

List of Figures

List of Tables

1. Introduction

1.1 Carbon Capture and Storage

Global warming has become a wide public concern, one of the biggest culprits behind it is the carbon dioxide (CO_2) emission into the atmosphere. Carbon capture and storage (CCS) technology is currently a feasible and economic method for reducing the greenhouse gas emissions. It consists of capturing CO_2 from large point sources, such as fossil fuel power plants, compressing it into a liquid or supercritical state and transporting it to a storage site for sequestration or to enhance oil recovery. In this scenario, the implementation of CCS technology has the potential to reduce CO_2 emissions into the atmosphere, whilst also facilitating the recovery of hydrocarbons through the application of EOR.

One technological interest in supercritical CO_2 ($scCO_2$) relies on its solvent properties. The $scCO_2$ has several advantages versus traditional solvents in industrial processes, it is non-toxic, non-flammable, abundant and inexpensive. The null surface tension and high diffusivity allows exceptionally effective penetration. The low viscosity facilitates mass transport. The relatively low critical temperature allows most compounds to be extracted with little damage. The solubility of many extracted compounds in $scCO_2$ varies with pressure, allowing selective extractions. It can also be easily recycled. Some of the current industrial applications of $scCO_2$ include: extraction of solids and liquids using dense gases, high pressure technologies for polymer processing, supercritical drying and cleaning, chemical and biochemical reactions in supercritical fluids and supercritical fluid applications in the energy domain.[1, 2]

1.1.1 Capture and Separation Technology

The first stage of the CO_2 capture process consists of separating CO_2 from other gases in power generation plants. The four primary routes for CO_2 capture are illustrated in Figure 1.1. [3]

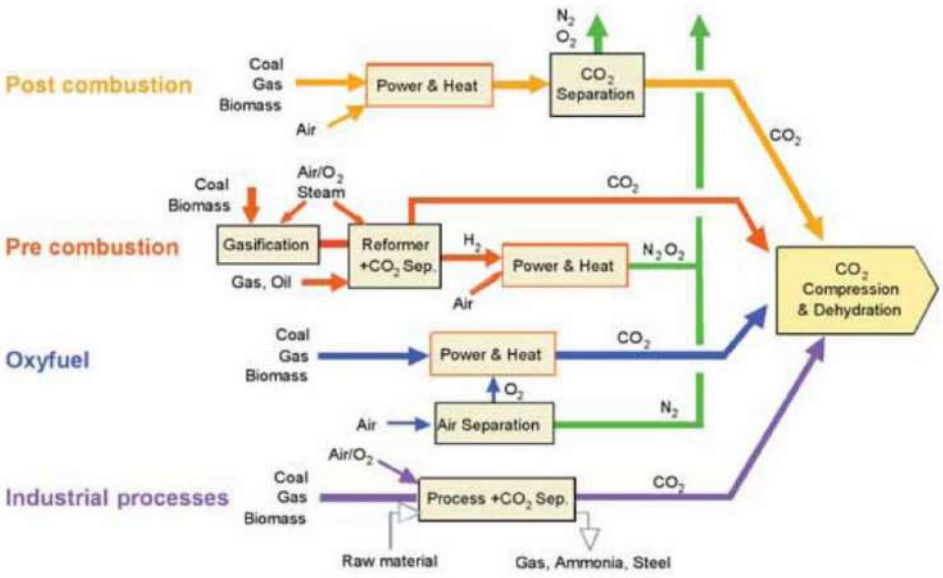

Figure 1.1: CO_2 capture technology options. [3]

The chemical composition of CO_2 streams currently being transported is highly dependent on its source. Hua et al. [4] compiled a list of CO_2 compositions transported in existing pipelines (Table 1.1). CO_2 from natural sources is typically high purity, only impurities such as CO_2, nitrogen (N_2), methane (CH_4), water (H_2O) and hydrogen sulfide (H_2S) are to be expected, requiring minimal treatment. However CO_2 from anthropogenic sources can have a very distinct composition, as the stream can be contaminated by gas impurities such as: sulphur oxides (SO_x), nitrogen oxides (NO_x), oxigen (O_2), carbon monoxide (CO), argon (Ar), hydrogen (H_2) and others, due to the associated combustion process. So, the exact composition will inevitably depend on the capture process, source and level of gas treatment applied. [4, 5]

Table 1.1: CO_2 compositions transported in existing pipelines. [4]

	Canyon reef carriers	Central basin pipeline	Sheep mountain	Weyburn	Sleipner*
Location	USA	USA	USA	USA/Canada	Norway
Operator	Kinder Morgan	Kinder Morgan	BP	Dakota gasification company	Statoil
Source	Anthropogenic	Natural	Natural	Anthropogenic	Separation from natural gas
CO_2	85-98	98.5	96.8-97.4	96	93-96
CH_4	2-15	0.2	1.7	0.7	0.5-2.0
N_2	<0.5	1.3	0.6-0.9	<300 ppm	3-5
H_2S	<260 ppm	<26 ppm	-	9000 ppm	150 ppm
O_2	-	<14 ppm	-	<70 ppm	-
NO_X	n.a.	-	-	n.a.	-
SO_X	n.a.	-	-	n.a.	-
H_2O	122 ppm	630 ppm	315 ppm	20 ppm	Water-saturated

* Corrosion resistant alloy pipeline

However, there is no general consensus on the allowable CO_2 stream impurities content, so companies set their own limits for CO_2 streams. To ensure safe transportation different CO_2 streams quality specifications have been proposed. In Table 1.2 a selected set of CO_2 requirements is shown. ENCAP project proposed a limit for all non-condensable gases, they together should not exceed 4 vol%. The limitation for the given NO_x, SO_x, H_2S and CO concentration is only based on health and safety considerations in a release scenario. The water content should be low enough such as it prevents the risks of free water formation, leading to corrosion. [6, 7]

Table 1.2: Different proposed CO_2 specifications. [7]

Compound	Specification (Kinder Morgan)	Specification (Ecofys)	Specification (Dynamis)	Reason
CO_2	min 95%	min 95%	min 95,5%	-
H_2O	257 ppm wt	max 500 ppm	max 500 ppm	Technical(Corrosion)
O_2	10 ppm wt	max 4 vol%	min 100-1000 ppm	Technical
SO_x	-	-	max 100 ppm	Health & safety
NO_x	-	-	max 100 ppm	Health & safety
H_2S	10-200 ppm	-	max 200 ppm	Health & safety
CO	-	-	max 2000 ppm	Health & safety
CH_4	max 5%	max 4%	max 2%	ENCAP project
N_2	max 4%	max 4%	max 4%	ENCAP project
H_2	-	max 4%	max 4%	ENCAP project
Ar	-	max 4%	max 4%	ENCAP project
Temperature	max 50°C	max 30°C	-	-

1.1.2 Transport Methods

After the capture process the CO_2 has to be transported to a suitable storage site. During transport, CO_2 is usually compressed to a supercritical state, in order

to increase density, and consequently reduce transportation costs. The CO_2 can be transported by pipeline, ship, rail or road, depending on the quantity, distance and the quality of CO_2 stream. It has been suggested that the best cost-effective choice would be the construction of a large-scale pipeline network shared by a number of different industries. These pipelines include old natural gases pipelines that were converted for CO_2 operations, or new ones that were built specifically for CO_2. Such technologies have been used for over 40 year. [3, 8]

Pipelines were selected as the preferred transportation method due to the large quantity it is able to transport at a relatively low cost. As of today, there are over 7000 km of operational CO_2 pipelines around the world. Most of them are located in the USA and Canada, while a few shorter pipelines can be found in Norway, Algeria, Hungary and Turkey. Figure 1.2 shows the location and size of CO_2 sources in the USA. They include natural gas processing, ethanol fermentation at bio-refineries, and hydrogen or ammonia production, which account for 87 Mt emissions per year. The map also shows potential locations for storage and existing pipelines. [9]

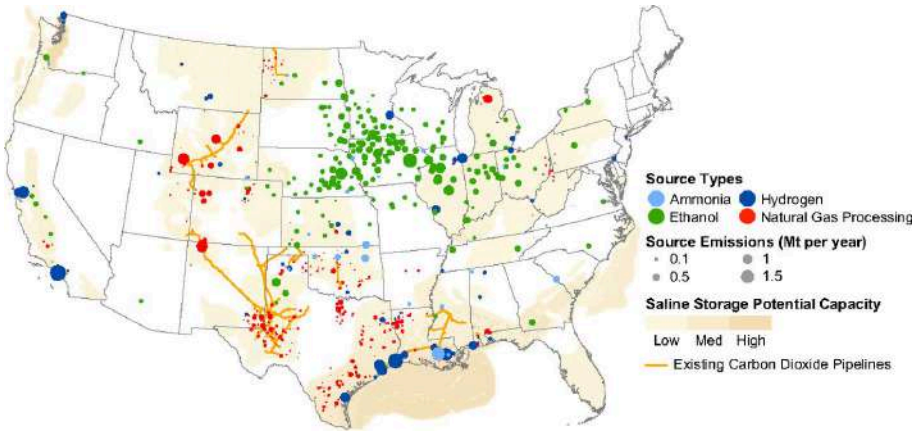

Figure 1.2: Map of CO_2 emissions sources, existing CO_2 pipelines, and potential saline storage formations in the USA. [9]

Most of CO_2 pipelines to this date are made of carbon-manganese pipeline grade steel. Its choice is based on its relatively low cost and favourable mechanical properties, however, carbon steel may be susceptible to corrosion. In order to avoid that, the water content is controlled to prevent free water formation in the pipeline.[8, 10]

For wet or sour service corrosion resistant alloys are more appropriate. Since they are more expensive than carbon steels, their use is limited to sections of the pipeline and compressors in which there is a risk of aqueous phase formation or water ingress. Such solution was chosen in the Sleipner project (Table 1.1), as the captured wet CO_2 needs to be transported only over a short distance.[4, 8]

DNV [10] listed material types and compatibility for CO_2 applications, this is shown in Table 1.3. Carbon steel is only recommended where there is no free water present, otherwise, stainless steel or nickel based alloys should be used. Low temper-

atures may result where rapid expansion of CO_2 occurs due to the Joule–Thomson effect, leading to freeze-up of valves and joints. Materials near these regions should be resistant to low temperatures. e.g. high-nickel carbon steel or austenitic stainless steels.[11]

Table 1.3: Candidate material types for CO_2 transport. [10]

	No free water		With free water	
Material	Pure CO_2	$CO_2 + H_2S$	Pure CO_2	$CO_2 + H_2S$
Carbon and low alloy steel	•	•		
316	•	•	•	•
13Cr	•	•	•	•
22Cr (duplex)	•	•	•	•
25Cr (duplex)	•	•	•	•
Nickel based alloy	•	•	•	•

1.1.3 Storage Process

After transportation, the CO_2 is usually stored safely and permanently in geological formations. Suitable storage sites may include depleted oil and gas fields and deep saline formations. CO_2 can be stored in a variety of geological formations, such as: oil fields, depleted gas fields, deep coal seams and saline formations (Figure 1.3). [3]

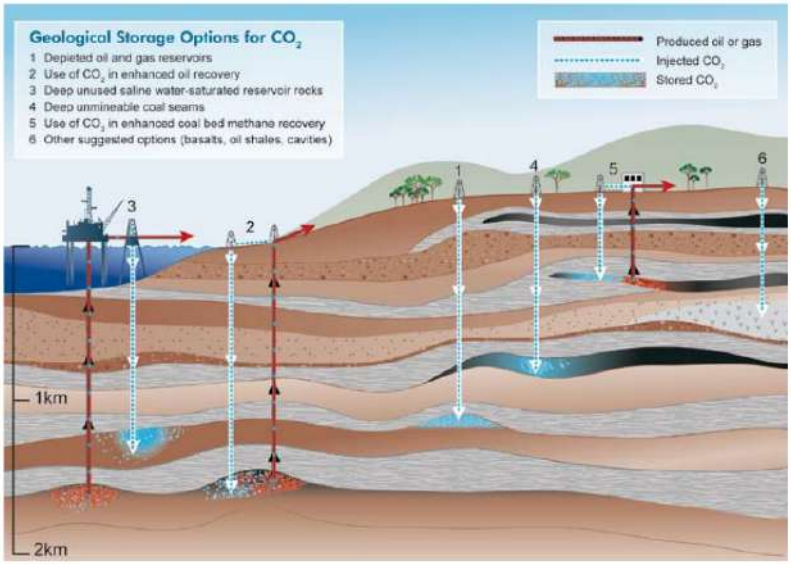

Figure 1.3: Options for storing CO_2. [3]

CO_2 can also be used for enhanced oil recovery (EOR), which is also called tertiary recovery. EOR consists of injecting CO_2 into near-depleted oil and gas fields to increase production. The extra oil that this technique allows to recover can help to offset some of the costs of CO_2 storage. Several companies have a vast

experience in injecting CO_2, for example, the Statoil's Sleipner project has safely stored over 7 $MtCO_2$ since 1996. [3, 12, 13]

In EOR operations CO_2 and water may be alternatively flooded into the injection wells. Typically, given the right physical conditions, CO_2 will mix miscibly with oil, acting as a thinning agent. After miscible mixing, the fluid is displaced by a chase phase, typically water (Figure 1.4). This cycle is repeated as determined by the operator. Over time, residual water will be dissolved in the CO_2 phase, and the well injection tube would be periodically immersed in corrosive CO_2 fluids with different degrees of water.[14]

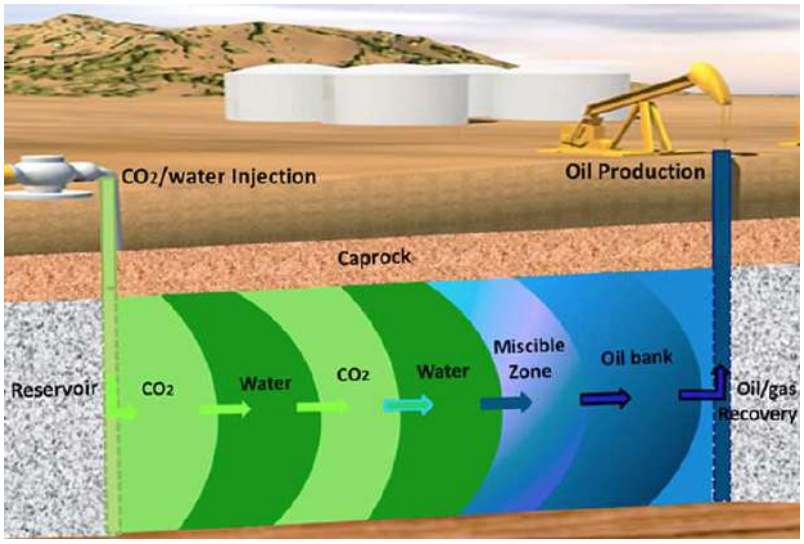

Figure 1.4: Schematic of the water-alternating-gas process for enhanced oil recovery. [15]

The water injected is usually produced water, which have a high Cl^- content. In the literature, when the test was intended to simulate field injection conditions, Liu et al.[14] used 0.1 mol NaCl + 0.01 mol $NaHCO_3$ + 0.01 mol $CaCl_2$ solution to mimic the produced water in Shengli oilfield, Hassani et al.[16] used 42.809 mg/L Cl^- + 3.624 mg/L SO_4^{2-} + 2.020 mg/L Ca^{2+} + 492 mg/L Mg^{2+} + 612 mg/L K^+ + 23.035 mg/L Na^+ solution to simulate down hole conditions within the Weyburn-Midale system, while Wei et al.[17] used 3.5% NaCl solution.

1.1.4 Challenges

The transport of CO_2 to a storage location needs to be safe. Johnson et al. [7] compiled a list of 29 incidents related to CO_2 transport from 1986 to 2008. The statistics in Figure 1.5 show that the major cause of failures was attributed to corrosion. Therefore, it is essential to evaluate the corrosion risk in CO_2 transport and injection pipelines to avoid any leakage. [5]

These corrosion incidents are usually associated with the formation of free water.

Therefore, most operations try to control the humidity content on the CO_2 stream. Although dry CO_2 is not corrosive to steels, some CO_2 applications admit the presence of water, so the presence of it in small quantities is expected. When liquid water is present it becomes saturated with CO_2, producing carbonic acid which increases the corrosivity of the environment. [14, 18–20]

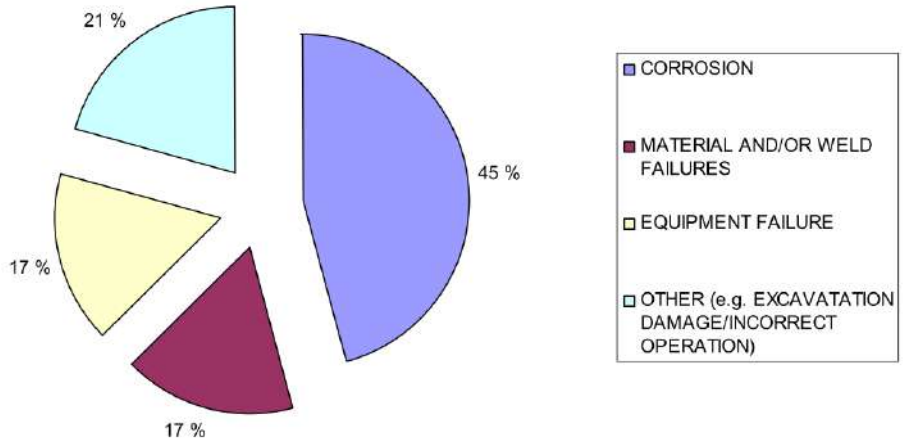

Figure 1.5: Failure modes for CO_2 pipeline systems in the US. [7]

The presence of additional impurities such as: O_2, SO_2, H_2S and NO_x, represent a further risk to the pipeline integrity. The severity of CO_2 corrosion also depends on the process variables and is influenced by a complex interaction of environmental parameters such as pH, temperature and CO_2 partial pressure. The CO_2 corrosion leads to the formation of corrosion products which can be protective or not depending on environmental parameters. [14, 18–20]

1.2 Contribution to the Literature

The effect of water content, impurities, temperature, pressure, on the corrosion of the steel in static $scCO_2$ has been studied in recent years. However, the effect of flow rate on the $scCO_2$ corrosion behaviour of the steel has rarely been reported.

This research intended contribution to the literature is to provide a further understanding of the corrosion in $scCO_2$ systems under flow regime. Including the influence of the flow on the condensation of water droplets and on film growth. This was carried out through the use of a rotating cage setup, designed to generate a flow in a closed system under high pressure and high temperature similar to those found in $scCO_2$ injection pipelines.

1.3 Objectives

This study goal is to provide a comprehensive understanding of the flow effect on the corrosion behaviour of carbon steels under supercritical conditions, attempting to make an insight into the corrosion mechanisms in CO_2 transportation and injection conditions. A methodology is proposed to accurately simulate CO_2 transportation and injection conditions in lab-scale tests. The specific objectives are outlined below, and the overall framework is summarised Figure 1.6.

- Develop a methodology to study the effect of fluid flow rate on the corrosion behaviour of steels in CO_2 transportation and injection.
- Correlate the effect of the fluid flow and/or fluid impurities content with the morphology of the corrosion scale formed.

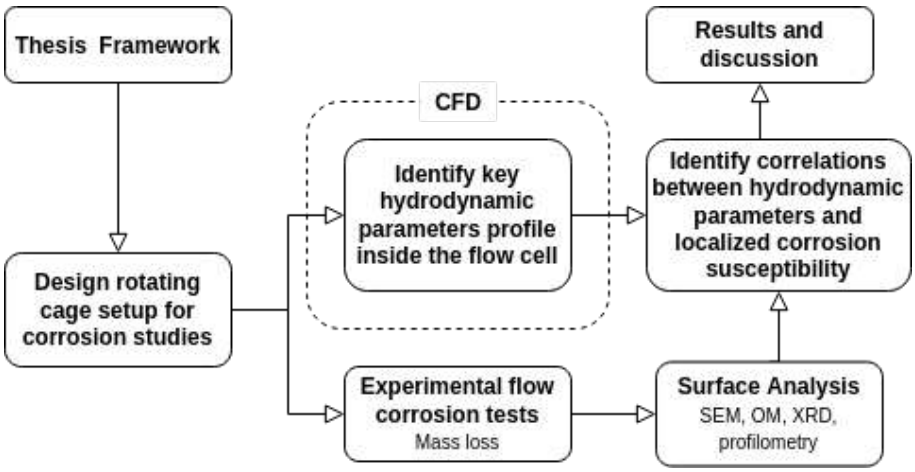

Figure 1.6: Schematic showing thesis objectives and structure.

1.4 Thesis Outline

Chapter 2 provides a literature review of the mechanisms of $scCO_2$ corrosion in the oil and gas industry and the description of computational fluid dynamics (CFD) techniques used to model fluid behaviour. Chapter 3 describes the experimental technique procedures used in this research, from cell design to surface analysis. While Chapter 4 provides the summary of the findings and the conclusions found in this work and proposes possible directions for future academic studies.

2. Literature review

2.1 Supercritical CO_2 corrosion

Several papers have been published in relation to CO_2 corrosion of of carbon and low alloy steels used in CO_2 transport pipelines that allowed a better understanding of several aspects of this phenomenon. While the older ones consider only the effect of CO_2 and H_2O, the latter account for the effect of some impurities in the corrosion process.

When the CO_2 dissolves in water, it is hydrated to form carbonic acid (H_2CO_3) (Equation (2.1)). As a weak acid, carbonic acid partially dissociates into hydrogen, bicarbonate and carbonate ions following a two step reaction (Equations (2.2) and (2.3)) [21]. The undissociated carbonic acid is known to acts as a "reservoir" of hydrogen ions ("buffering effect"), by replenishing them when they get depleted by the reduction reaction at the metal surface [22].

$$CO_2 + H_2O \leftrightarrows H_2CO_3 \tag{2.1}$$

$$H_2CO_3 \leftrightarrows H^+ + HCO_3^- \tag{2.2}$$

$$HCO_3^- \leftrightarrows H^+ + CO_3^{2-} \tag{2.3}$$

It most often has been assumed that the corrosion of steel in H_2O-CO_2 systems involves two cathodic reactions (Equations (2.4) and (2.5)) and an anodic reaction (Equation (2.6)). In CO_2 systems at low pH (<4) the Equation (2.4) is the dominant reaction due to the high H^+ concentration. At intermediate pH ($4 < pH < 6$), in addition to the hydrogen reduction, the Equation (2.5) provides an additional source of H^+ ions. [21]

$$H^+ + e^- \leftrightarrows H \tag{2.4}$$

$$H_2CO_3 + e^- \leftrightarrows H + HCO_3^- \tag{2.5}$$

$$Fe \leftrightarrows Fe^{2+} + 2e^- \tag{2.6}$$

When the concentration of Fe^{2+} and CO_3^{2-} in the bulk is sufficiently high, exceeding the saturation ratio with respect to $FeCO_3$ (SR > 1), the ferrous ion can

react directly with carbonate ions (Equation (2.7)) or react with bicarbonate ions following a two step process (Equation (2.8) and (2.9)) and precipitate on the steel surface. [23]

$$Fe^{2+} + CO_3^{2-} \rightarrow FeCO_3 \tag{2.7}$$

$$Fe^{2+} + 2HCO_3^- \rightarrow Fe(HCO_3)_2 \tag{2.8}$$

$$Fe(HCO_3)_2 \rightarrow FeCO_3 + CO_2 + H_2O \tag{2.9}$$

Corrosion rate can be significantly reduced when $FeCO_3$ precipitation occurs, due to the formation of a dense pseudo-passive film. This film acts as a diffusion barrier preventing corrosive species from reaching the steel surface [23]. Like other protective films, these $FeCO_3$ films are susceptible to damage that can lead to severe uniform or localised corrosion, which can pose a significant threat to the pipeline integrity. [24, 25]

The film morphology can differ depending on environmental conditions. Pessu et al. [26] carried out tests in NaCl 3.5% solution at 50 ^oC while varying the pH and observed three different morphologies (Figure 2.1): at pH 3.8 a Fe_3C scale with traces of $FeCO_3$ was observed, at pH 6.6 a protective $FeCO_3$ film was formed, which resulted in a reduction of uniform corrosion, with a few regions of localized corrosion in small regions without film, at pH 7.5 a passive and protective $FeCO_3$ film with a layer of Fe_3O_4, and very few pits were observed. [26]

2.1.1 Effect of water content

Although dry CO_2 is not corrosive to steels, the presence of free water has been regarded as a particular cause for concern for supercritical CO_2 applications. Therefore, most applications focus on sufficiently drying the CO_2 before using it. However, in some applications, such as in water-alternating-gas (WAG) enhanced oil recovery (EOR), the well is flooded alternatively with CO_2 and water. In such applications residual water cannot be avoided and the injection lines would be periodically exposed to CO_2 fluids with different water contents [5, 14].

Spycher and Pruess [27] compiled a database of $H_2O - CO_2$ mutual solubilities for various temperatures and pressures. Above the solubility limit the H_2O and CO_2 tends to separate, creating free water. If water is present, it quickly becomes saturated with CO_2, producing carbonic acid, thus creating a local corrosive environment that may affect the pipeline integrity [5]. This leads to three main scenarios of interest:

H_2O-undersaturated scCO_2: In this scenario the water content is well bellow the dew point, therefore only the supercritical CO_2 phase is present. Studies have shown that corrosion of carbon steel can still take place in conditions

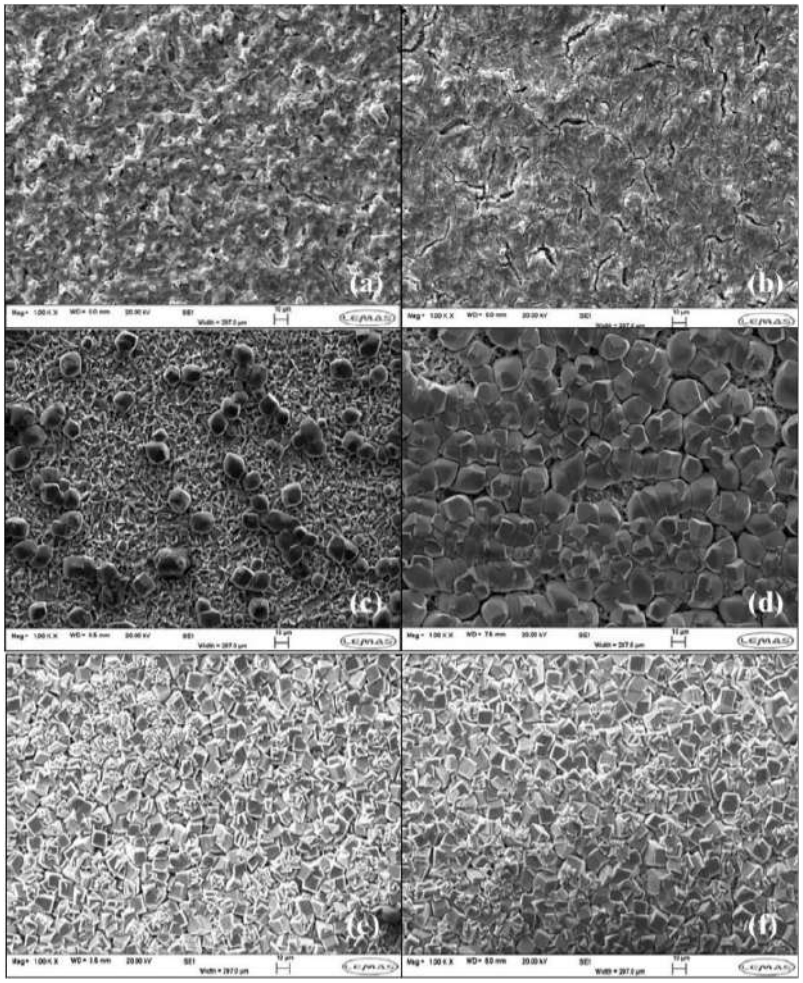

Figure 2.1: Corrosion product on the surface of API 5L X65 steel after imersion in NaCl 3.5% solution at 50 ^{o}C at pH 3.8: (a) 36h and (b) 72h, pH 6.6: (c) 36h and (d) 72h and pH 7.5: (e) 36 h and (f) 72 h. [26]

where the water content is well below the solubility limit of H_2O in $scCO_2$, however general corrosion rates would be very small in such environments (< 0.04 mm/y). [4, 28]

H_2O-saturated or near saturated $scCO_2$: In this scenario, the water can locally exceed the solubility limit and condensate in droplets on the steel surface. When this happens, water quickly becomes saturated with CO_2, producing carbonic acid. The presence of additional impurities such as: O_2, SO_2, H_2S and NO_2, represent a further risk to the pipeline integrity. Under dewing conditions, corrosion occurs at a higher rate, while it is speculated that the higher corrosion happens where a condensed water droplet is attached to the steel surface. The pitting mechanism of carbon steel in $scCO_2$ is portrayed in Figure 2.2. It shows that after the formation of water droplets, acid gas impurities dissolve in water droplets to produce a corrosive environment. The steel surface covered by the droplets is corroded first, leading to pitting formation.

[28, 29]

scCO$_2$-saturated H$_2$O: In the third scenario the water content is so high that the aqueous phase becomes the main corrosive medium. In this scenario corrosion rate of carbon steel can be very high, and even some stainless steels may be susceptible to corrosion depending on the impurities content. [30]

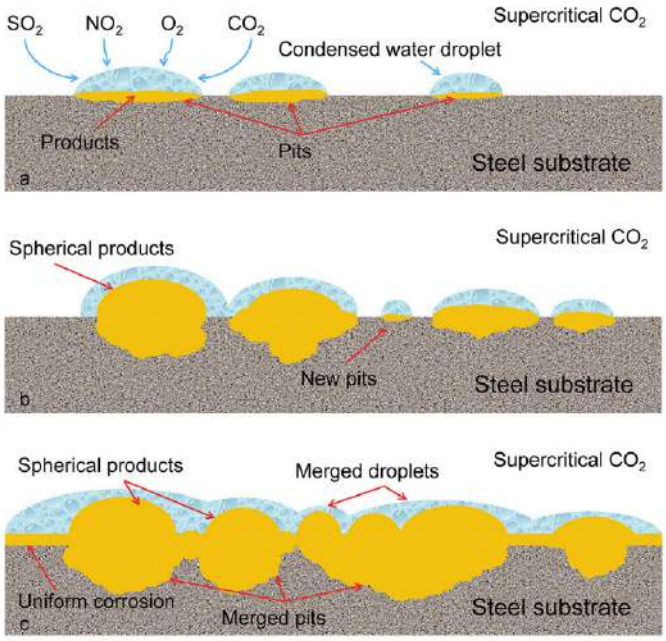

Figure 2.2: Illustration of pitting corrosion mechanism of steel in water-saturated supercritical CO_2 with impurities: (a) initial stage, (b) increasing in droplet amount, (c) merged pits. [29]

2.1.2 Effect of temperature

The main effects of temperature on the corrosion of steels under scCO$_2$ conditions are controlling the activity of the reactants and the solubility of the corrosion products. The activity of the reactants is highly dependent on the temperature. At low temperatures the activity of the reactants is very low, resulting in a low reaction rate. At the same time, the solubility limit of Fe^{2+} and CO_3^{2-} is higher, taking longer before its concentrations exceeds the solubility limit needed so that the precipitation of $FeCO_3$ crystals becomes thermodynamically favorable. [31, 32]

On the other hand, as the temperature increases, the activity of the reactants increases, and the reaction rate increases accordingly. Furthermore, at higher temperatures the saturation of the solution is reached much earlier, leading to the precipitation of $FeCO_3$ crystals. At some point, the precipitation of $FeCO_3$ crystals may form a dense and protective corrosion scale on the steel surface, which hinders the mass transfer between the bulk and the steel surface, decreasing the corrosion

rate. [30, 32]

In summary, the corrosion rate of steels under $scCO_2$ conditions as a function of temperature, firstly increases and then decreases, with a maximum value in the middle. This trend have been reported by Zhang et al. [31], where they assessed the corrosion rates of API 5L X65 steel under static $scCO_2$ conditions and found that the corrosion rate increased from 50°C to 80 °C and then decreased from 80°C to 130 °C. While Ingham et al. [33] analysis indicates that films formed at lower (< 40 °C) have a porous structure, while those formed at increasing solution temperatures are thinner and denser films, offering a greater degree of protection.

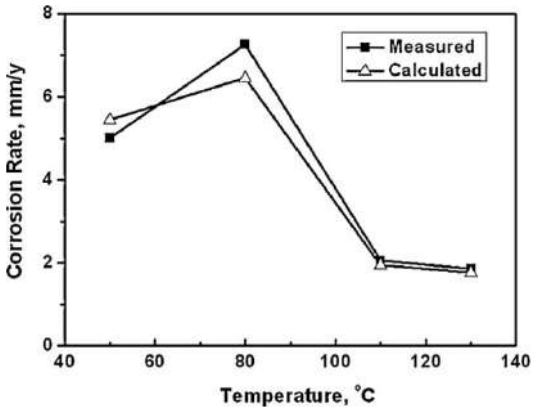

Figure 2.3: The comparison between the measured and the calculated corrosion rate of X65 pipeline steel under supercritical CO_2 conditions at various temperatures. [31]

2.1.3 Effect of CO_2 partial pressure

The mutual solubility of H_2O and CO_2 have been compiled by Spycher et al. [27] in a database for various temperature and pressure. It shows that the solubility of CO_2 in H_2O increases with the pressure. Choi and Nesic [34] showed (Figure 2.4) that not only the CO_2 solubility, but also the H_2CO_3 and HCO_3^- solubility in water increased with the increase of CO_2 partial pressure.

However, the effect on the Fe^{2+} concentration is is not as straight forward, Dugstad [35] showed (Figure 2.5) that in some instances, an increase in CO_2 partial pressure may increase or decrease the formation of a protective $FeCO_3$ film. For a pH level of 6 the solubility decreases as pressure increases, for a pH level of 4 the solubility increases as pressure increases and for intermediary values goes through a maximum value as pressure increases.

Li et al. [36] carried out tests of 110S steel in CO_2/H_2S environments at 130°C while varying the CO_2 partial pressure. It can be seen from Figure 2.6 that the average corrosion rate at 8 MPa CO_2 partial pressure was almost twice the corrosion

rate at 4 MPa. This was explained by the corrosion product scale transformation from compact fine-grain scale into a less protective bulky-grained scale.

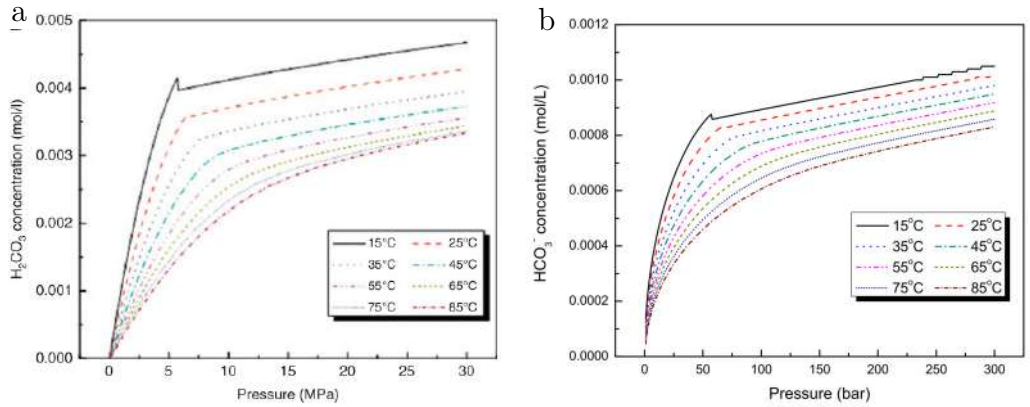

Figure 2.4: Solubility of (a) H_2CO_3 and (b) HCO_3^- in water as functions of pressure and temperature. [34]

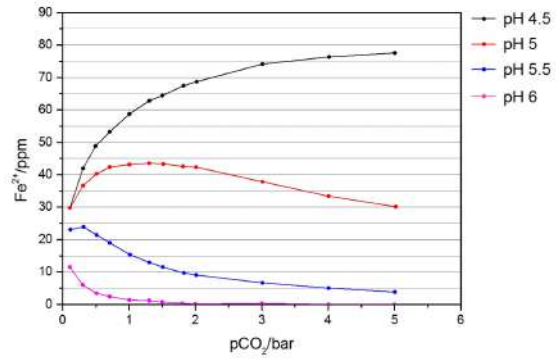

Figure 2.5: Fe^{2+} solubility as a function of CO_2 partial pressure for various pH. [35]

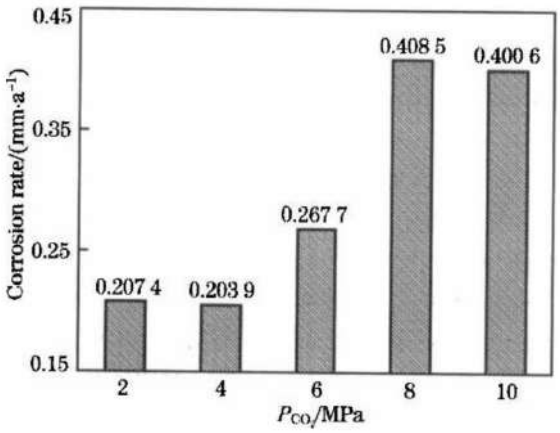

Figure 2.6: Average corrosion rates of 110S steel at different CO_2 partial pressures. [36]

While Choi and Nesisc [37] results showed that at 50°C the corrosion rate of

carbon steels didn't significantly change when was within the 4 to 8 MPa range. Choi et al. [38] studied the corrosion properties of carbon steel under different CO_2 partial pressures (4, 8, and 12 MPa) and temperatures (65°C and 90°C) in 25 wt% sodium chloride (NaCl) solution, they found little effect of CO_2 partial pressure. As shown in Figure 2.7, at 65°C the corrosion rate was higher at higher pressures. However, at 90°C the corrosion rates followed the same trend in the first couple hours, but rapdly decreased due to $FeCO_3$ scale formation, and exhibited higher values at lower pressure, which is the oposite of the 65°C results. They also found that corrosion scale morphologies were almost identical regardless of the pressure.

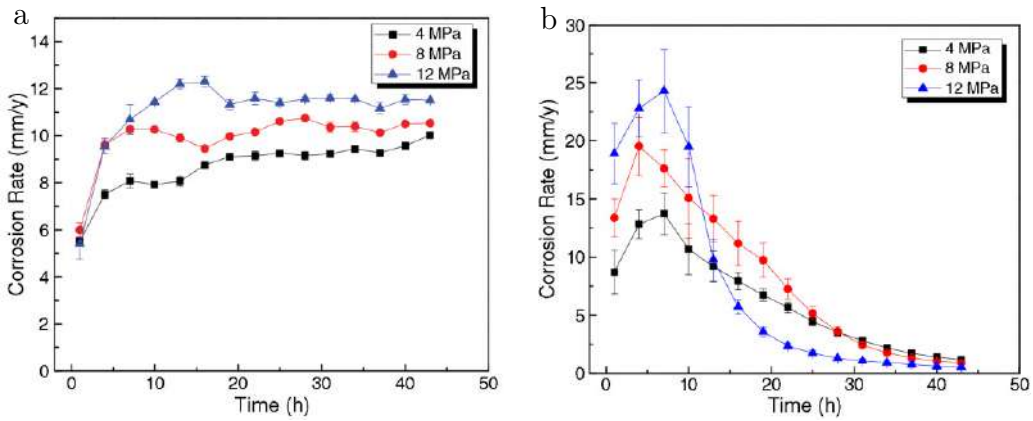

Figure 2.7: Variations of corrosion rate for carbon steel with different CO_2 partial pressures at (a) 65°C and (b) 90°C. [38]

2.1.4 Effect of CO_2 impurities

2.1.4.1 Addition of O_2

The two major effects of the introduction of O_2 in the CO_2 corrosion systems are: the introduction of a cathodic reaction (Equation 2.10), which can increase the corrosion rate. Along with the inhibition of $FeCO_3$ formation by the sequestration of Fe ions, forming a non-protective porous iron oxide layer, resulting in a increase of corrosion rate as well.[30]

$$O_2 + 4H^+ + 4e^- \rightarrow 2H_2O \tag{2.10}$$

Dugstad et al.[39] results showed that when the H_2O content in $scCO_2$ was far bellow the solubility limit, the presence of O_2 had no effect on the corrosion. However, as the H_2O content increases to values closer to the solubility limit, the influence of O_2 gets more noticeable. In this case, the addition of 100-200ppm O_2 in the autoclave increased the corrosion rate of X65 steel by 50-120%. They also found deeper localized attack due to the destabilisation of $FeCO_3$ film.

Choi et al. [40] results showed that O_2 inhibited the formation of a $FeCO_3$ layer on the steel surface. Instead, the surface was covered by a porous iron oxide scale, as shown in Figure 2.8.

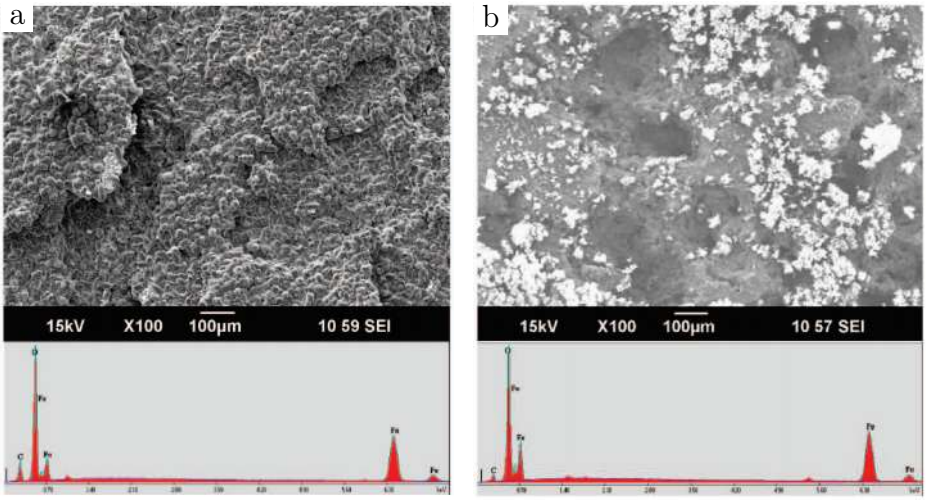

Figure 2.8: SEM image and EDS spectra of API 5L X65 steel coupons surface after exposure in CO_2-saturated water for 120 h: (a) without oxygen, (b) with oxygen. [40]

2.1.4.2 Addition of SO_2 + O_2

When SO_2 is present in the system, it can promote the formation of $FeSO_4$ film, which is known to be less protective than the $FeCO_3$ film. Additionally, when both SO_2 and O_2 are present in the system, there is also the risk of sulphurous H_2SO_3 and/or suphuric H_2SO_4 acid formation. These acids can lower the solution pH further, increasing the corrosivity of the system. [5]

The minimum H_2O content required for such acid formation is not known. However, $FeSO_3$ and/or $FeSO_4$ have been detected on the corroded steel surface of some experiments at H_2O concentrations far below the H_2O solubility. The $FeSO_3$ and/or $FeSO_4$ formation has been represented by the reaction shown in Equations (2.11) to (2.16). First SO_2 dissolves to sulphite ions in water following a two step reaction (Equations (2.11) and (2.12)).[5, 41]

$$H_2O + SO_2 \rightarrow H^+ + HSO_3^- \tag{2.11}$$

$$HSO_3^- \rightarrow H^+ + SO_3^{2-} \tag{2.12}$$

When O_2 is present in the system, it can oxidize sulphite ions to sulphate ions (Equation (2.13)).

$$2SO_3^{2-} + O_2 \rightarrow 2SO_4^{2-} \tag{2.13}$$

Fe^{2+} ions can react with either SO_3^{2-} or SO_4^{2-} and precipitate via the reactions in Equations (2.14) and (2.15).

$$Fe^{2+} + SO_3^{2-} \rightarrow FeSO_3 \tag{2.14}$$

$$Fe^{2+} + SO_4^{2-} \rightarrow FeSO_4 \tag{2.15}$$

Choi et al.[40] also believe that $FeSO_4$ can undergo further oxidation via the reaction in Equation (2.16)

$$4FeSO_4 + 6H_2O + O_2 \rightarrow 4FeOOH + 4H_2SO_4 \tag{2.16}$$

Three distinct corrosion morphologies have been reported in systems containing SO_2 and O_2: a thin sulphur-rich cracked film (Figure 2.9a), columnar $FeSO_3$/$FeSO_4$ crystals (Figure 2.9b) and globular $FeCO_3$ crystals (Figure 2.9c).

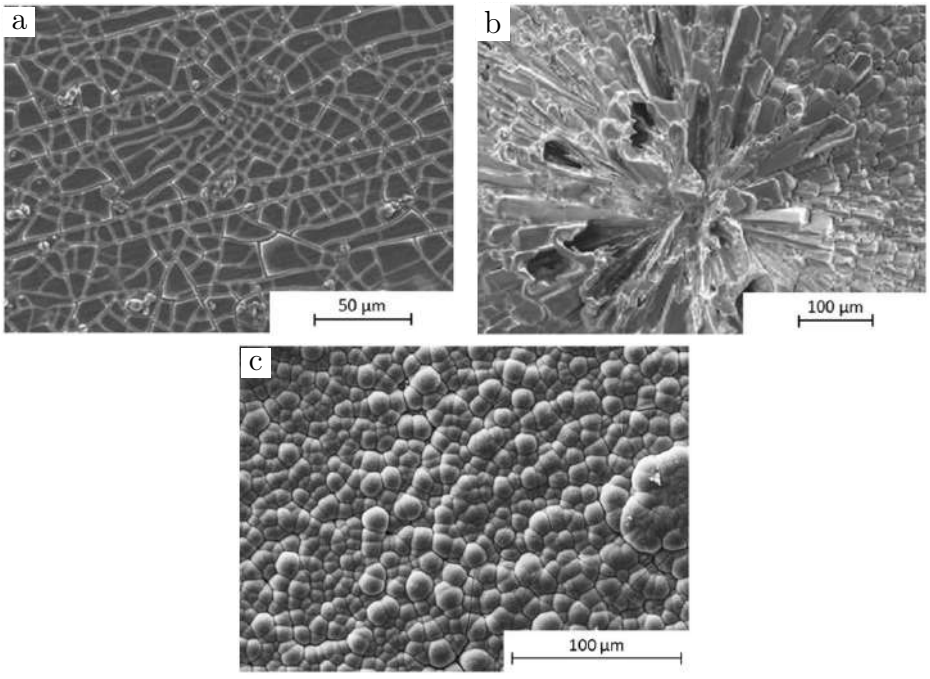

Figure 2.9: Corrosion products formed on carbon steel surfaces under $scCO_2$ conditions containing water, SO_2 and O_2; (a) thin sulphur-rich cracked film [42], (b) columnar $FeSO_3$ crystals [40] and (c) globular $FeCO_3$ crystals [4].

The globular $FeCO_3$ crystals have only been observed at low SO_2 concentrations (<100ppm). The presence of SO_2 is capable of changing the morphology of $FeCO_3$ from the typical cubic like crystals. [43, 44]

At higher concentrations, it has been shown that SO_2 dominates the corrosion process and prevent any $FeCO_3$ formation. Not much is known about the protectiveness of both thin sulphur-rich cracked film and columnar $FeSO_3$ crystals. The cracks in the thin sulphur-rich film may expose the steel surface to the bulk solution,

however its not clear if the cracks appear during the test or due to the dehydration after removing from the autoclave. [45]

Choi and Nesic [46] assessed the corrosion behavior of X65 steel under $scCO_2$ conditions containing SO_2 and O_2 at 8MPa and 50°C for 24h. Results are shown in Figure 2.10. When the water content is far below the solubility limit the corrosion rate was lower than 0.01mm/year. When 0.08MPa of SO_2 was added, the corrosion rate increased to 3.48mm/year. When 0.033MPa of O_2 was added on top of the SO_2 the corrosion rate slightly increased to 3.70mm/year. This shows that the corrosion rate increased dramatically in the presence of SO_2.

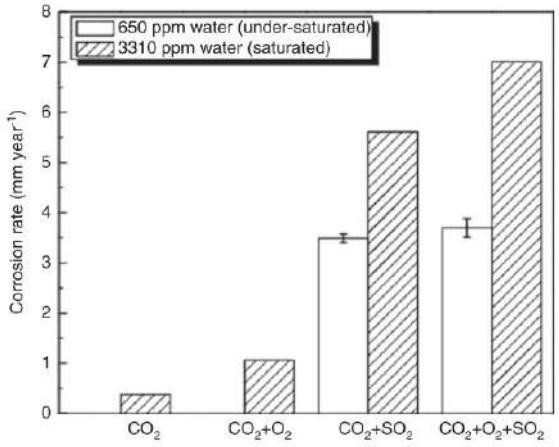

Figure 2.10: Effects of O_2, SO_2, and their mixtures on the corrosion rates of carbon steel under $scCO_2$ conditions.[46]

2.1.4.3 Addition of NO_2

Similarly to the previous one, when NO_2 is present in the system, it can dissolve to form nitric acid in water following the reaction in Equation (2.17). This will reduce the pH of the system and accelerate the cathodic reactions.[41]

$$3NO_2 + H_2O \rightarrow 2HNO_3 + NO \tag{2.17}$$

Ayello et al.[47] compared the effect of impurities such as O_2, SO_2 and NO_2 in the corrosion rate of a 1010 steel at 75.8bar and 40°C by using electrochemical measurements. They found that 100ppm of O_2 did not affect the corrosion rate, but it increased from 2.3 to 4.6mm/year in the presence of SO_2, additionally, it increased even further, to 11.6mm/year in the presence of NO_2.

The typical corrosion product morphology under $scCO_2$ in the presence of NO_2 is shown in Figure 2.11. It is a brown/orange colored dusty, porous film with little adherence to the steel surface. Dugstad et al.[48] EDX analysis revealed no nitrogen compounds present on the film. They suggested that the nitric acid oxidised Fe^{2+}

ions within the solution.

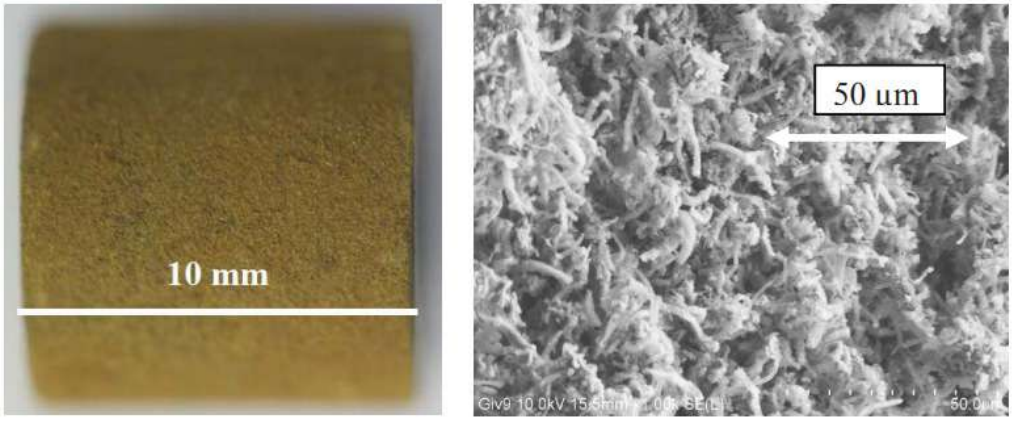

Figure 2.11: (a) photograph and (b) SEM image of the corrosion product morphology under $scCO_2$ in the presence of NO_2. [48]

Brown et al.[49] tested several carbon steels under $scCO_2$ conditions at various concentrations of O_2, SO_2 and NO_2. They reported that the corrosion rates were highest in the presence of NO_2. Based on the literature seems like NO_2 is the most aggressive species in terms of how they influence the corrosion kinetics.

2.1.4.4 Complex mixtures

In the context of carbon capture and storage, depending on the CO_2 emission source, all those impurities mentioned above may coexist mixed with CO_2. Most studies focused on the investigation of the effect of a single species. However, little is known about the combined effect of the impurities. The synergistic effect of them may increase the degradation of the material.

The reactions are not limited to the steel-electrolyte interface. There is also the possibility of numerous reactions within the bulk phase, resulting in the formation of sulphuric/sulphurous acid, nitric acid and elemental sulphur when water, SO_2, NO_2, NO, O_2 and H_2S are present together. Currently not much is known about which reaction is the most thermodinamically favourable. [50]

2.1.5 Effect of brine chemistry

Typical oilfield brines can have a complex chemical composition, that may include NaCl, $CaCl_2$, $MgCl_2$, $CaCO_3$, among other salts and dissolved inorganic content. The presence of divalent cations has been shown to facilitate the precipitation of mixed carbonates, and this results in corrosion products with distinct morphology and chemical properties when compared to the pure counterparts. [51–53]

Esmaeely et al. [54, 55] investigated the influence of Ca^{2+} concentrations (up to 10000 ppm) on the corrosion of a carbon steel at 80 ^{o}C and room pressure. They

reported that at low Ca^{2+} concentrations the corrosion rate decreased with time due to the formation of a protective scale. However, at high concentrations of Ca^{2+} the corrosion rate increased with time due to formation of a non-protective scale and attributed this effect to the Ca^{2+} rather than CL^{-}.

Shamsa et al. [56] made similar observations when evaluating the corrosion of carbon steel at 80 and 150 ^{o}C in brine solutions with Ca^{2+} concentrations varying between 0 and 1.83 (wt.%). The addition of Ca^{2+} resulted in the formation of a thicker and less protective corrosion product layer consisting of $Fe_xCa_yCO_3$, but these effects were smaller at higher temperatures. HUA *et al.* [51] observed that at 100 bar and 60 ^{o}C the addition of Ca^{2+} (from 0 to 10000 ppm) reduced the general corrosion rate of carbon steel in the beginning of the tests, but the values converged for longer exposure times (up to 96 h). And also, observed that Ca^{2+} was more likely to co-precipitate in conjunction with $FeCO_3$ compared to Mg^{2+}.

In Tavares et al. [52] observations, although the presence of $CaCO_3$ decreased the general corrosion rate, it increased the localised corrosion rate. Which was attributed to the greater porosity of mixed carbonate films, making them more susceptible to chloride permeation.

2.1.6 Effect of fluid flow

The fluid flow can significantly alter the kinetics of precipitation, modify the film morphology, or even prevent its formation, either by the acceleration of dissolution, or due to mechanical erosion forces generated by fluid flow.

The fluid flow of the corroding system affects the corrosion process in two ways. In the absence of corrosion product layers an increase of fluid flow velocity was found to enhance transport of species towards and away from the metal surface. This will lead to an increase in the corrosion rate due to the decrease of local pH (transport of H^{+} ions to the surface [57]), and the reduced precipitation rate of corrosion products (transport of Fe^{2+} away from the surface lowers the surface saturation rate [58]). This makes it more difficult to form a protective layer under high fluid flow velocities.

The second point is that, once a protective layer is formed on the surface the question is whether it will remain protective. Above a certain critical fluid flow intensity, the turbulence elements acting on the surface can prevent the precipitation of protective films or even damage the integrity of the already formed films [58–60].

Tanupabrungsun [61] investigated the influence of flow on CO_2 corrosion behaviour of carbon steel at 120^{o}C using RCE. It was reported that the $FeCO_3$ crystals appeared to be damaged after increasing the flow velocity of system (Figure 2.12). However, the damage was attributed to the chemical dissolution rather than

a mechanical damage. Without flow, the surface pH is expected to increase faster than the bulk pH. But, under flow conditions the local pH at the steel surface could decrease to the point that the solution becomes under-saturated for the $FeCO_3$ formation.

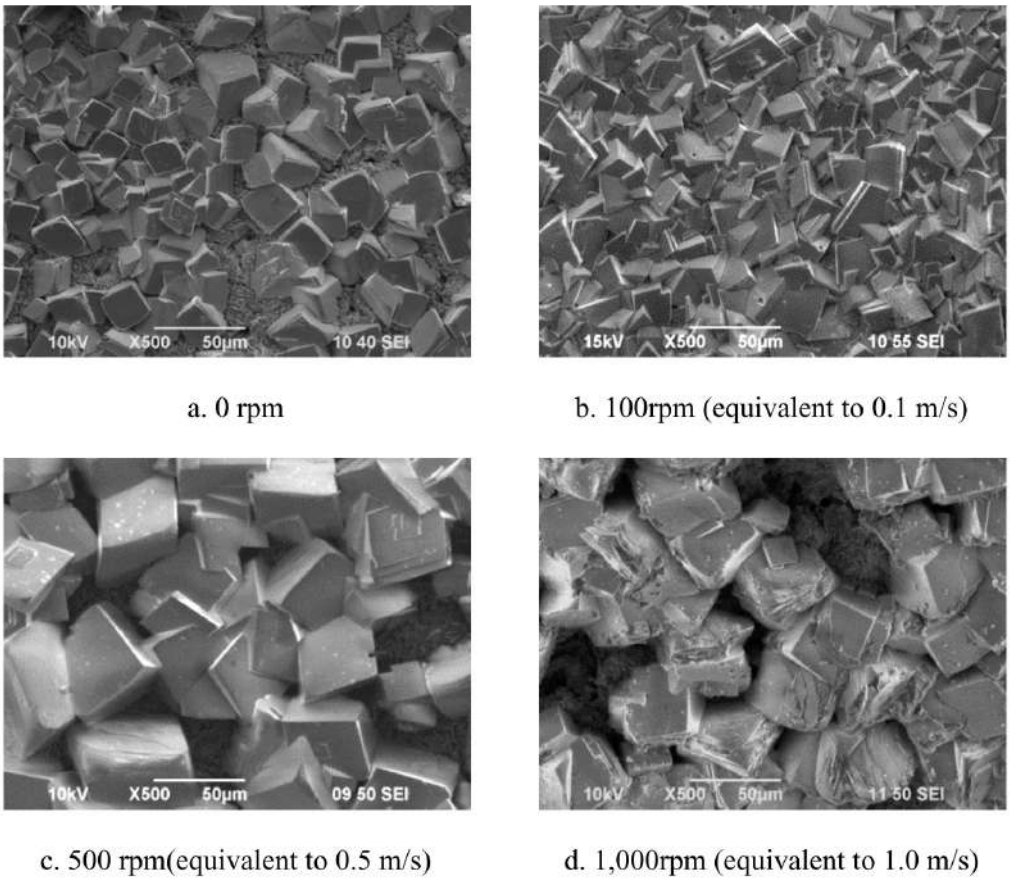

Figure 2.12: SEM images showing the effect of flow velocity on the morphology of $FeCO_3$. [61]

Wei et al. [17], also noticed a change in the predominant corrosion type of carbon steel in the supercritical CO_2-saturated aqueous phase, from uniform corrosion under static condition, to localised corrosion under the dynamic condition. These areas of localised corrosion under the dynamic condition originated from damaged areas of the dense $FeCO_3$ film that happened even considering that the wall shear stresses generated at the surface were several orders of magnitude smaller than the adhesion strength of $FeCO_3$.

2.2 Computational Fluid Dynamics

Computational fluid dynamics (CFD) is a branch of fluid mechanics that uses numerical analysis to analyse and solve problems that involve fluid flows. It is a cost-effective way for researchers to understand, develop, optimise, and control designs

and processes. Often the flow itself is not the main focus in a simulation. Instead it is how the flow affects other process and application parameters that is important.

2.2.1 Governing Flow Equations

2.2.1.1 Continuity Equation

The continuity equation, which is also known as the conservation of mass equation is based on two fundamental principles: mass that enters the system per unit of time should be equal to the mass leaving the system, meaning that mass cannot be created or destroyed and that there are no empty spaces between the fluid elements, that is, the flow is continuous, and can be expressed as: [62]

$$\frac{\partial \rho}{\partial t} + \nabla \cdot \rho \mathbf{u} = 0 \tag{2.18}$$

where ρ is the density, and u is the flow velocity. In an incompressible fluid the density is constant, so the equation (2.18) becomes:

$$\nabla \cdot \mathbf{u} = 0 \tag{2.19}$$

2.2.1.2 Momentum Equation

The momentum Equation can be derived from Newton's second law of motion which states that the rate of change of momentum of a body is directly proportional to the force applied: [62, 63]

$$\mathbf{F} = \frac{dp}{dt} = \frac{d(m\mathbf{v})}{dt} = m\frac{d\mathbf{v}}{dt} = m\mathbf{a} \tag{2.20}$$

Assuming the body is a fluid, it is convenient to divide the equation per unit of volume as follows:

$$\rho \frac{D\mathbf{u}}{Dt} = \mathbf{F}_{\text{surface}} + \mathbf{F}_{\text{body}} \tag{2.21}$$

where u is the velocity, $F_{surface}$ and F_{body} are the forces per unit of volume applied on the body and the surface of the fluid particles respectively. The gravity produces the most common body force, but for other applications additional body forces (e.g. electrostatic fields) may also be important. External forces on the other hand are expressed by pressure and viscous forces;

$$\mathbf{F}_{\text{body}} = \rho \mathbf{g} \tag{2.22}$$

$$\mathbf{F}_{\text{surface}} = \nabla \cdot \tau \tag{2.23}$$

where τ is a stress tensor that, for Newtonian fluids, can be expressed in terms of the dynamic viscosity μ: [64]

$$\tau = \mu(\nabla u + (\nabla u)^{T}) - \frac{2}{3}\mu(\nabla \cdot u)I \tag{2.24}$$

On incompressible flows the Equation (2.19) can substituted into Equation (2.24), and substituting the Equations (2.22), (2.23) and (2.24) into Equation (2.21) results in the Navier-Stokes equation for incompressible fluids [62]:

$$\rho\left(\frac{\partial \mathbf{u}}{\partial t} + \mathbf{u}\cdot\nabla\mathbf{u}\right) = -\nabla P + \nabla\cdot\tau + \rho\mathbf{g} \tag{2.25}$$

2.2.1.3 Conservation of Energy

Equation 2.26 describes the conservation of energy, formulated in terms of temperature. However, for the purpose of this study the temperature variations are small and unimportant (isothermal) such that the energy equation can be neglected. [62]

$$\rho C_p\left(\frac{\partial T}{\partial t} + (\mathbf{u}\cdot\nabla)T\right) = -(\nabla\cdot\mathbf{q}) + \tau : \mathbf{S} - \frac{T}{\rho}\frac{\partial\rho}{\partial T}\bigg|_p\left(\frac{\partial p}{\partial t} + (\mathbf{u}\cdot\nabla)p\right) + Q \tag{2.26}$$

2.2.1.4 Reynolds number

The Reynolds number is defined as the ratio of inertial forces to viscous forces, which, for a standard rotating cage apparatus is shown in Equation (2.27).

$$Re = \frac{2r\nu\rho}{\mu} \tag{2.27}$$

where ρ is the fluid density, μ is the dynamic viscosity, r is the radius of the cage and ν is the coupon tangential velocity.

This dimensionless value is used to indicate the flow regime. Bellow a critical value ($Re_{crit} \approx 10^4$) the flow is classified as laminar, where the fluid flows in parallel layers, with no disruption between those layers. Above the critical value, the inertia forces dominate the viscous forces, irregular and chaotic fluctuations appear in the flow, and it becomes a turbulent flow. [62]

2.2.2 Turbulence Modeling

The equations shown previously can be used to solve laminar flow, where the fluid flows in parallel layers, with no disruption between those layers. However, in a turbulent flow the motion can be characterized by time-dependent irregular and chaotic fluctuations in flow velocity. The presence of turbulence usually dominates

all other flow features and results in increased energy dissipation, mixing, heat transfer and drag.[63, 65, 66]

Since turbulent flows are highly irregular, turbulence problems are normally treated statistically rather than deterministically. In order to do that Reynolds [67] introduced the idea of decomposing the velocity vector (u) into a mean ($\overline{u}$) and fluctuating part (u'):

$$u = \overline{u} + u' \tag{2.28}$$

This can be applied to the Navier Stokes equations to obtain the Reynolds-averaged Navier–Stokes (RANS) equation:

$$\frac{\partial \overline{u}}{\partial t} + \overline{u} \cdot \nabla \overline{u} = -\nabla \overline{P} + \nabla \cdot (\nu \nabla \overline{u}) - \nabla \cdot (\overline{u'u'}) + g \tag{2.29}$$

where the term $\overline{u'u'}$ is known as the Reynolds stress tensor. The commonly described Boussinesq approximation [68] proposes that those Reynolds stresses are proportional to the mean rates of deformation:

$$\overline{u'u'} = \nu_t(\nabla u + (\nabla u)^T) + \frac{2}{3}kI \tag{2.30}$$

where ν_t is the kinematic eddy viscosity and k is the turbulent kinetic energy per unit mass, defined as:

$$k = \frac{1}{2}\overline{u'u'} \tag{2.31}$$

and the kinematic eddy viscosity can be evaluated in:

$$\nu_t = C_\mu \frac{k^2}{\varepsilon} \tag{2.32}$$

$$\varepsilon = \nu \tag{2.33}$$

The Reynolds-Averaged Navier-Stokes (RANS) equations can be solved numerically using a suitable turbulent model.

2.2.2.1 The $k-\varepsilon$ Model

The standard $k-\varepsilon$ turbulence model is currently the most popular turbulence model because it is widely established and has excellent performance against a range of flow situations. It was proposed by Chou [69] and then later on refined by Launder and Sharma [70], the latter version is generally referred as the standard k–ε model. It is a two-equation model that uses the turbulence kinetic energy (k), as first variable and the rate of dissipation of turbulent kinetic energy (ε), as the second variable. The evolution of k and ε is modeled as [62]:

Kinematic Eddy Viscosity:

$$\mu_t = \rho C_\mu \frac{k^2}{\varepsilon} \tag{2.34}$$

Turbulence Kinetic Energy:

$$\rho \frac{\partial k}{\partial t} + \rho \mathbf{u} \cdot \nabla k = \nabla \cdot \left(\left(\mu + \frac{\mu_t}{\sigma_k} \right) \nabla k \right) + P_k - \rho \varepsilon \tag{2.35}$$

Dissipation Rate:

$$\rho \frac{\partial \varepsilon}{\partial t} + \rho \mathbf{u} \cdot \nabla \varepsilon = \nabla \cdot \left(\left(\mu + \frac{\mu_t}{\sigma_\varepsilon} \right) \nabla \varepsilon \right) + C_{\varepsilon 1} \frac{\varepsilon}{k} P_k - C_{\varepsilon 2} \frac{\varepsilon^2}{k} \rho \tag{2.36}$$

Closure Coefficients and Auxiliary Relations:

$$C_{\varepsilon 1} = 1.44, \quad C_{\varepsilon 2} = 1.92, \quad C_\mu = 0.09, \quad \sigma_k = 1.0, \quad \sigma_\varepsilon = 1.3 \tag{2.37}$$

Despite being the most used turbulence model, the $k-\varepsilon$ model has a term which can not be calculated at the wall, so wall functions must be used, and is also not appropriate for use in flows with strong separation, large curvature or large pressure gradients due to it's poor performance. Some variants were proposed that aim to reduce these limitations, such as the Realisable $k-\varepsilon$ model and the RNG $k-\varepsilon$ model. [71, 72]

2.2.2.2 The $k-\omega$ Model

The $k-\omega$ model was proposed by Kolmogorov [73] and then further developed by Wilcox [74]. It is a two-equation model that uses the turbulence kinetic energy (k), as first variable and the turbulence frequency (ω), as the second variable. The evolution of k and ω is modeled as [62]:

Kinematic Eddy Viscosity:

$$\mu_t = \rho \frac{k}{\omega} \tag{2.38}$$

Turbulence Kinetic Energy:

$$\frac{\partial k}{\partial t} + \rho \mathbf{u} \cdot \nabla k = P_k - \rho \beta^* k \omega + \nabla \cdot ((\mu + \sigma^* \mu_t) \nabla k) \tag{2.39}$$

Specific Dissipation Rate:

$$\frac{\partial \omega}{\partial t} + \rho \mathbf{u} \cdot \nabla \omega = \alpha \frac{\omega}{k} P_k - \rho \beta \omega^2 + \nabla \cdot ((\mu + \sigma \mu_t) \nabla \omega) \tag{2.40}$$

Closure Coefficients and Auxiliary Relations:

$$\alpha = \frac{13}{25}, \quad \beta = \beta_o f_\beta, \quad \beta^* = \beta_o^* f_\beta, \quad \sigma = \frac{1}{2}, \quad \sigma^* = \frac{1}{2} \tag{2.41}$$

$$\beta_o = \frac{13}{125}, \qquad f_\beta = \frac{1+70\chi_\omega}{1+80\chi_\omega}, \qquad \chi_\omega \equiv \left|\frac{\Omega_{ij}\Omega_{jk}S_{ki}}{(\beta_o^*\omega)^3}\right| \tag{2.42}$$

$$\beta_o^* = \frac{9}{100}, \quad f_\beta = \begin{cases} 1, & \chi_k \leq 0 \\ \frac{1+680\chi_k^2}{1+400\chi_k^2}, & \chi_k > 0 \end{cases}, \quad \chi_k = \frac{1}{\omega^3}(\nabla k \cdot \nabla \omega) \tag{2.43}$$

$$\varepsilon = \beta^* \omega k, \qquad \ell_{mix} = \frac{k^{\frac{1}{2}}}{\omega} \tag{2.44}$$

The $k-\omega$ model is also very popular because may be accurate and robust in some cases where $k-\varepsilon$ model is not accurate, such as internal flows, flows that exhibit strong curvature, separated flows, and jets. It does not contain a term that is undefined at the wall, so it can be resolved all the way to the wall without the need of wall functions. However, it's main draw-backs reside in it's non-linearity nature, that combined with it's sensitivity to the initial conditions, makes it more difficult to converge when compared to the $k-\varepsilon$ model. [71, 72]

2.2.2.3 Wall Functions

Turbulent flows are significantly affected near solid walls because at the wall the no-slip condition that has to be satisfied. Near the walls the effect of the viscous effects on the flow become more predominant, and the velocity profile continuously decreases as it gets closer to the solid surface. This region on the surface of a solid body in which viscous effects are important is known as the boundary layer. Typical boundary layer structure over a flat plate is shown in Figure 2.13 and can be divided into three regions. [75]

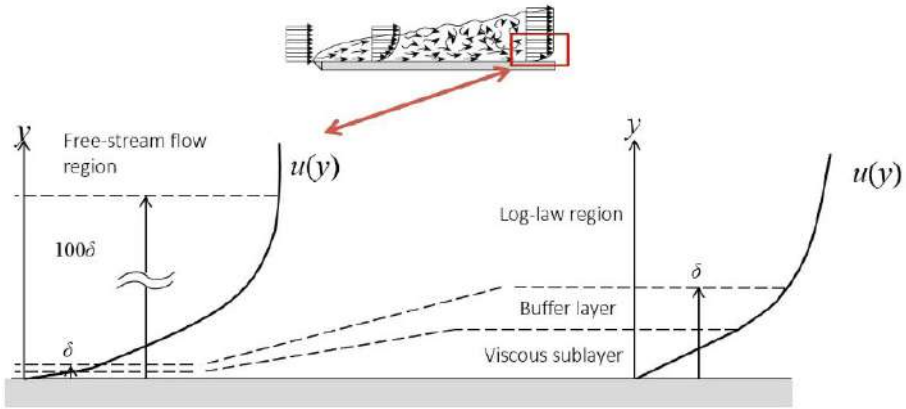

Figure 2.13: Flow regions near the wall. [76]

The law of the wall defines an important concept to distinguish the different regions of the boundary layer, which is the dimensionless wall distance (y^+), described in Equation 2.45.

$$y^+ = \frac{yu_\tau}{\nu}, \qquad u_\tau = \sqrt{\frac{\tau_w}{\rho}}, \qquad u^+ = \frac{u}{u_\tau} \tag{2.45}$$

where y is the distance from the wall, u_τ is the friction velocity, τ_w is the wall shear stress, ρ is the density, ν is the viscosity and y^+ is dimensionless. The three regions shown in Figure 2.14 are:

The viscous sublayer ($y^+ < 5$): In this region the flow is dominated by the viscous forces and the following linear relation holds:

$$u^+ = y^+ \tag{2.46}$$

The logarithmic area ($30 < y^+ < 200$): In this region the turbulence stress dominate the flow and velocity profile varies following a logarithmic function:

$$u^+ = \frac{1}{\varkappa}\ln(Ey^+) \tag{2.47}$$

The Buffer layer ($5 < y^+ < 30$): The viscous and turbulent forces have similar magnitude, creating complex velocity profiles that are not well defined.

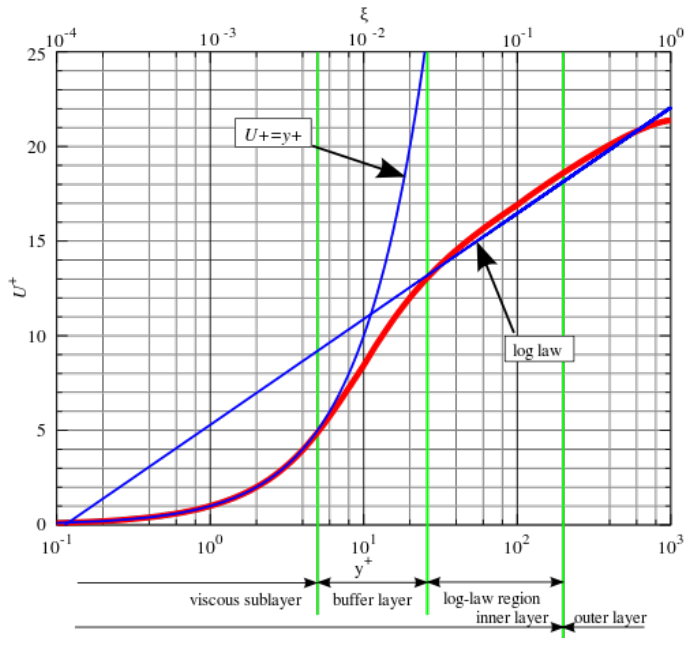

Figure 2.14: Relation between u^+ and y^+ in the three regions of the boundary layer. [77]

In order to accurately resolve the near wall regions, two solutions are usually proposed (Figure 2.15). One way is to use a very fine and dense mesh near the wall

so that almost all the effects are captured, which means a substantial computational cost is needed. In order to reduce computational costs, the second approach involves the use of wall functions. An offset is defined over the wall surface where the mesh is not resolved inside this offset. Instead, empirical relations are used to bridge the gap between the wall and the turbulent region. However, since wall functions are a compromise between computational cost and accuracy, they must be used with careful consideration. For y^+ values within the range of 1 wall functions are not required as the grid is fine enough to resolve the boundary layer. [63, 78, 79]

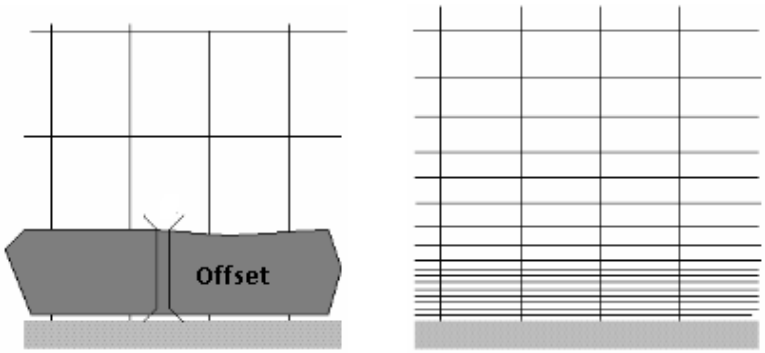

Figure 2.15: Illustration of the (a) use of wall functions and (b) refined mesh near the wall. [78]

3. Experimental Procedure

This chapter is intended to present the materials and methodology used in this study, as well as the description of each experimental procedure.

3.1 Material

The material used in this research was X80 steel. Figure 3.1 shows the optical microscopy of the samples after the etching with 2% Nital solution, and the chemical composition is shown in Table 3.1. Figure 3.1a shows the distribution of various inclusions in the steel matrix. The low magnification micrograph (Figure 3.1b) shows a fine and homogeneous microstructure free of banding structure. The high magnification micrograph (Figure 3.1c) revealed a microstructures are composed of ferrite and granular bainite comparable to the ones found in studies with similar material [80, 81].

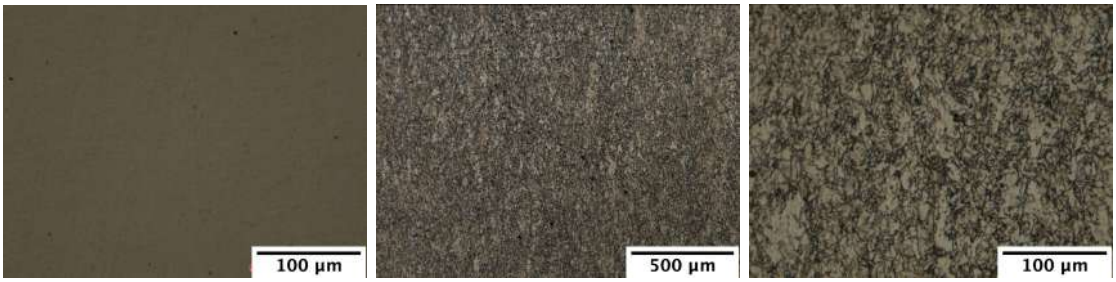

(a) (b) (c)

Figure 3.1: Optical micrography characterization of the X80 steel: (a) polished, (b) etched (2% Nital solution) and (c) etched (2% Nital solution).

Table 3.1: Chemical composition of the steel used. (wt. %)

	C	**Mn**	**P**	**S**	**Si**	**Ni**	**Cr**	**Mo**	**V**	**Nb**
API 5L X80	0.041	1.56	0.010	0.001	0.300	0.251	0.057	0.201	0.001	0.037

Each test was carried out using six 22 x 9 x 3 mm^3 samples (a 2 mm diameter hole was drilled for mounting) with all surfaces ground progressively following 220, 400 and 800 grit silicon carbide paper. The samples were degreased with acetone, washed with deionised water, and dried before weighing using an electronic balance

with an accuracy of 0.01 mg and then stored in a desiccator until use.

The microstructure was characterized using optical microscopy (OM) and scanning electron microscopy (SEM) in order to identify the phases present in the material. For metallographic observations, the sample surface was polished by successive silicon carbide paper up to 1200 mesh. Followed by polishing with diamond paste of 6 μm, 3 μm and 1 μm successively. Then it was etched using 2% Nital solution.

3.2 Methodology

3.2.1 Autoclave testing procedures

In order to assess the corrosion behaviour of the X80 steel in aqueous or supercritical CO_2 phases under dynamic flow conditions, a methodology based on rotating cage tests was used. Figure 3.2a shows the schematic experimental setup used for the tests. The system consists of a conditioning cell, an autoclave, a temperature and speed controller and CO_2 cylinders. Tests were performed in a 1 L Hastelloy C276 autoclave with a rotating shaft. In each test six samples were fixed in a sample holder made of PEEK (polyether ether ketone) that was then fixed onto a shaft which can rotate inside the autoclave, as shown in Figure 3.2b. This allowed a symmetrical weight distribution to stabilize the stirrer and the coupons. Tests were carried out in static and dynamic conditions for comparison, and the full list of experimental conditions are listed in Table 3.2.

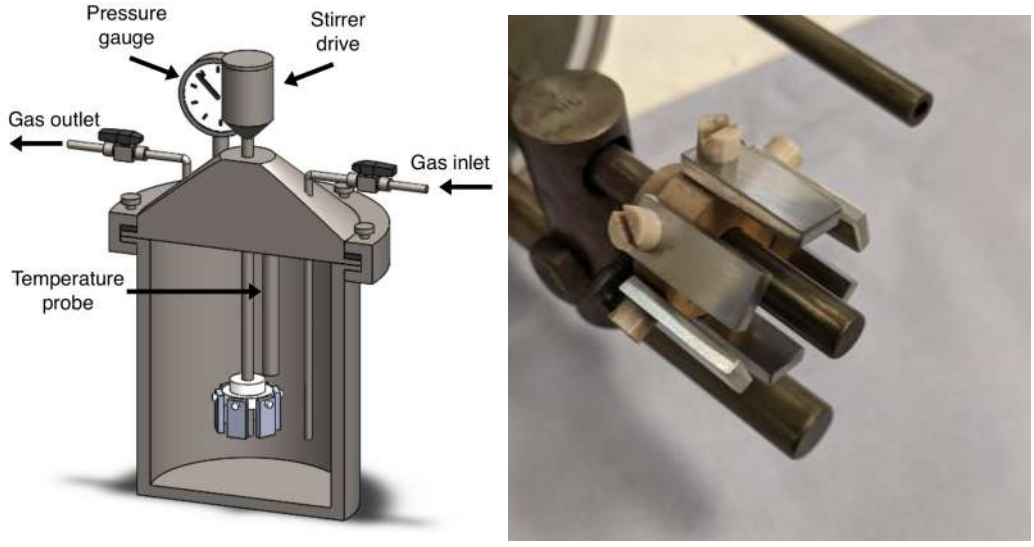

(a) (b)

Figure 3.2: (a) Schematic experimental setup and (b) detail showing the samples attached to the holder and rotating shaft.

Table 3.2: Test matrix for corrosion tests in aqueous or supercritical CO_2 phases under dynamic flow conditions.

Type	Temperature (°C)	Pressure (bar)	Brine composition (g/L)		Flow rate (m/s)	Duration (h)
			NaCl	$CaCl_2 \cdot 2H_2O$		
Aqueous	35	80	30.00	0	0	48
			27.08	3.67	0.5	
			15.42	18.34	1	
			30.00	0	0	96
			27.08	3.67	0.5	
			15.42	18.34	1	
$scCO_2$			-	-	0 0* 0.15 0.3 0.5 1.0	48

* Fast initial rotation for a very short period.

3.2.1.1 Aqueous phase tests

Tests were carried out in CO_2-saturated brines that were prepared using deionized water and analytical grade reagents, where the contents were balanced so that it contained 0, 1000 or 5000 ppm of Ca^{2+} and maintained a constant chloride ion concentration. The brine was prepared by bubbling it with CO_2 for at least 2 h/L in a separate container (conditioning cell). Once saturated with CO_2, 500 mL of the brine was transferred to the autoclave, then the autoclave was pressurised up to 30 bar using CO_2 and vented twice to purge any oxygen in the system. After that the autoclave was pressurised to 80 bar and heated to the desired temperature.

3.2.1.2 Supercritical CO_2 phase tests

Testing procedure was similar to the described in the previous section, but a lower amount of aqueous phase was used. Spycher et al. [27] calculated the mutual solubilities of H_2O and CO_2 from 12 to 100 °C and up to 600 bar, they found that the saturated water concentration in supercritical CO_2 at 35 °C and 80 bar is 3437 ppm. However, to ensure complete saturation of supercritical CO_2, once saturated with CO_2, 10 mL of solution was introduced in the bottom of the autoclave using a pipette, without direct contact with the samples, which was enough to keep the $scCO_2$ saturated, while the excess free water level at the bottom of the autoclave was low enough to not touch the coupons. Then, the autoclave was pressurised up to 30 bar and vented twice to purge any remaining oxygen. After that the autoclave was pressurised to 80 bar using CO_2 and heated to a temperature of 35 °C.

Tests setups for supercritical CO_2 have been shown to face some challenges, Morland and Svenningsen [82] reported that wetting of the sample surface may happen in the initial step of the test setup either due to accidental splashing of the water located at the bottom of the autoclave, caused by the injection of CO_2 or condensation of water droplets may occur during the depressurisation of the test systems at the end of experiments, and can contribute to misleading corrosion rates. However, since all the tests in this study followed the same setup and stop procedure, they can be readily compared.

3.2.2 Mass loss measurements

At the end of each test, the autoclave was depressurised before removing the samples, rinsing with deionized water and drying with compressed air. After that the samples were weighed, then chemically cleaned with the aid of Clarke's solution (20 g antimony trioxide, 50 g stannous chloride and 1000 ml hydrochloric acid) to remove corrosion products, followed by rinsing and drying one more time, before weighing again. The average corrosion rate was determined using Equation 3.1, as described in ASTM Standard G1 [83], where Δm is the mass difference in g, ρ is the material density in g/cm^3, A is the sample surface area in cm^2, t is the test duration in hours and C_{rate} is the corrosion rate in mm/y. To minimize the error associated with the cleaning process, an uncorroded control coupon was cleaned by the same procedure used on the test coupon. The mass loss resulted from the cleaning process was used to adjust the corrosion mass loss of the test coupons.

$$C_{rate} = \frac{87600 \cdot \Delta m}{\rho \cdot A \cdot t} \tag{3.1}$$

3.2.3 Electrochemical measurements

As the test time progresses, the species formed/consumed in the corrosion electrochemical reactions are expected to change the brine chemistry, surface pH and bulk pH over time [84]. Such that at the end of the test period the test cell will have a complex chemical composition which is highly dependent on the initial conditions. This scenario would impose a challenge to compare the corrosion scales formed under different test conditions.

Therefore, to eliminate influence from brine chemistry, it was decided that after each test, one of the corroded samples was transferred to a cell containing a standardized brine (CO_2-saturated 30 g/L NaCl solution at 25 ^{o}C, room pressure and pH 3.8), to investigate the electrochemical properties of the corrosion scales using linear polarization resistance and potentiodynamic polarization techniques. The

samples were prepared by soldering a wire to it and coating all the unwanted surfaces were covered with an electrical insulating resin. A typical three electrode cell was used where the pre-corroded samples were used as working electrodes (WE), a platinum wire as counter electrode (CE) and an Ag/AgCl (1M KCl) reference electrode (RE). A potentiostat was used to run linear polarization resistance (LPR) and potentiodynamic sweeps. This method used a potentiodynamic sweep over a range of potentials from OCP to -300mV in the cathodic direction followed by another from OCP to 150mV in the anodic direction.

The average corrosion rate by electrochemical measurements was determined using Equation 3.2 [85], where M_{Fe} is the iron atomic mass in g/mol, n is the number of electrons transferred in the reaction, ρ is the material density in g/cm^3, A is the working electrode exposed area in cm^2 and i_{corr} is the corrosion current density in mA/cm^2 determined by Equation 3.3, where β_a and β_c are the anodic and cathodic Tafel constants respectively and R_p is the polarization resistance in $\Omega \cdot cm^2$. The polarization resistance (R_p) was determined by LPR measurements, which were made using a scan rate of 0.2 mV/s in the potential range of $E_{corr} \pm 15mV$. The response is approximately a straight line where the slope is the polarization resistance (R_p). Potenciodynamic measurements were used to determine the anodic (β_a) and cathodic (β_c) Tafel constants, in mV/decade. [85]

$$C_{rate} = 3.27 \frac{i_{corr} M_{Fe}}{n \rho A} \tag{3.2}$$

$$i_{corr} = \frac{\beta_a \beta_c}{2.303(\beta_a + \beta_b) R_p} \tag{3.3}$$

3.2.4 Surface analysis

After each test the coupons were rinsed with distilled water, followed by ethanol and then dried with the help of a hot air gun. Then they were stored in desiccator until needed. The morphology and chemical composition of the corrosion products were analyzed by a combination of scanning electron microscopy (SEM), surface profilometry and X-ray diffraction (XRD).

3.2.4.1 Scanning electron microscopy

The surface morphology of the samples was observed using a Carl Zeiss EVO MA15 scanning electron microscope (SEM). The images were captured using secondary electron mode at an accelerating voltage of 20 kV at an average working distance of 8 mm.

Due to the number of features observed on some images, ImageJ [86] version

1.53c software was used to process the images allowing a statistical analysis of the size distribution of corrosion patches on the surface. Figure 3.3 shows the steps used in the analysis. First the corrosion features were manually selected (Figure 3.3b, then the background was removed, leaving only the selected areas (Figure 3.3c) and then the software was used for automatic object counting and measuring (Figure 3.3d).

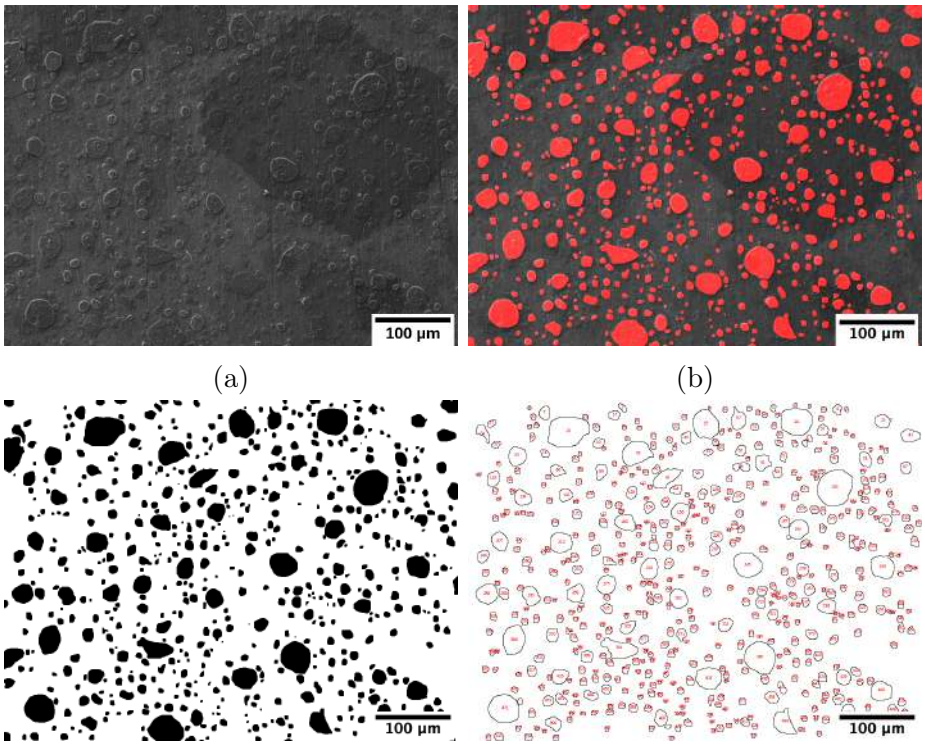

(a) (b)

(c) (d)

Figure 3.3: Steps of the image processing, (a) raw unprocessed image, (b) feature selection, (c) segmentation and (d) feature analysis.

Cross section energy-dispersive X-ray spectroscopy (EDX) analysis was also used in order to identify and quantify the chemical composition of the corrosion products. This technique allows the mapping of individual elements distribution as shown in Figure 3.4. Line scans of the corrosion product were prepared either by coating samples with platinum before cutting a trench in the corrosion product layer using a FEI Nova200 dual beam FIB/SEM or mounting the sample in epoxy resin before cutting and polishing a cross section of the sample.

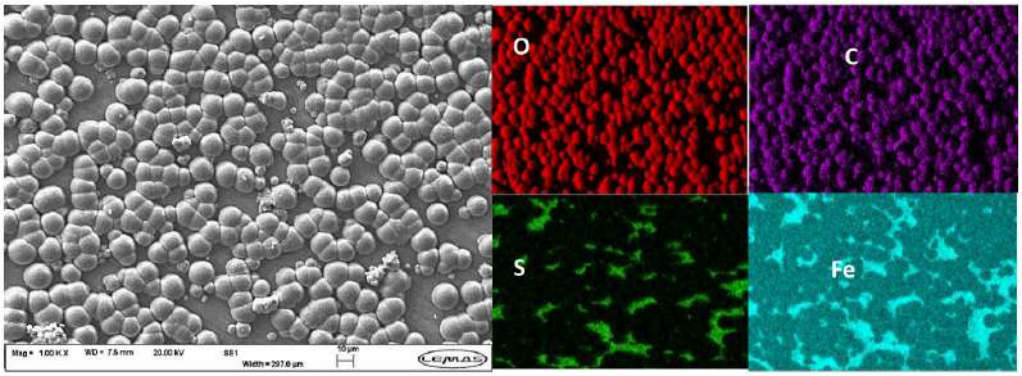

Figure 3.4: Example of EDX map showing areas rich in O, C, S and Fe. [87]

3.2.4.2 X-ray diffraction

A Bruker D8 X-ray diffractometer was used to identify the corrosion products on the surface of the coupons after each test. Measurements were made with K_α of 1.54187Å and the angle was adjusted continuously from 20^o to 70^o.

To calculate the molar fraction of Ca in $Fe_xCa_{x-1}CO_3$ the Equation 3.4 [56] was used. This equation considers that the $FeCO_3$ and $CaCO_3$ share hexagonal lattice structure, consequently, the introduction of Ca into $FeCO_3$ matrix will result in an increase of the d-spacing and shift the peak positions associated with the diffraction patterns of such crystalline planes towards lower values of 2Θ. The peaks used in the equation were the most intense Bragg peaks for $CaCO_3$ and $FeCO_3$, which are located at 2Θ positions 29.42^o and 32.07^o respectively, which correspond to the [104] inter-planar spacing. [55, 56]

$$\frac{1}{d^2} = \frac{4}{3}\left(\frac{2.924y + 26.626}{148.214y + 582.680}\right) + \frac{16}{(1.688y + 15.373)^2} \tag{3.4}$$

3.2.4.3 Surface profilometry

A Bruker NPFlex 3D optical profilometer was used to identify pitting or preferential attack areas on the sample's surface. It allows the capture of multiple two-dimensional images at different depths, that are used for the reconstruction of three-dimensional structures within the object.

Prior to taking profilometric measurements, the samples were cleaned in Clarke's solution. The NPFlex was used to assess the profile along 3 rectangular areas of the specimen surface facing the outer side of the rotating frame. The built-in software was then be used to determine the profile of sub areas within the scanned areas, as shown in Figure 3.5, then count and measure the pits in each of those sub areas.

To determine the extent of localised corrosion, pitting detection and analysis was completed using a non-contact profilometer (NPFLEX 3D Surface Metrology

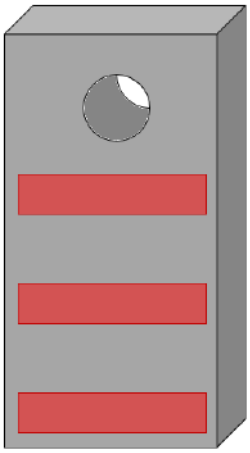

Figure 3.5: Schematic sample highlighting the profilometric measurement area.

System) across the sample surface, after removing the corrosion products. On each sample, three 1x1 mm^2 sample areas were scanned, which were then used to estimate characteristics of the whole surface. The pit penetration rate was calculated using Equation 3.5 [88], where C_{pit} is the pit penetration rate in mm/year, h is the pit depth in μm, and t is the exposure time in hours.

$$C_{pit} = \frac{8.76h}{t} \tag{3.5}$$

3.3 CFD modelling

CFD models were used to simulate the fluid flow in a virtual environment, allowing the identification of conditions that may affect the corrosion kinetics on the surface of the specimens inside the test cell. COMSOL Multiphysics® version 5.4 [62] was used to create the simulation and solve for the flow of fluid within the test cell (autoclave). The $k-\varepsilon$ turbulence model was selected to numerically solve the turbulent fluid flow due to its good convergence rate and relatively low memory requirements. It is a two-equation model that solves for two variables: k, the turbulence kinetic energy (Equation 2.35); and ε the rate of dissipation of turbulence kinetic energy (Equation 2.36).

3.3.1 Boundary conditions

A summary of the boundary conditions used are shown in Figure 3.6b. A no-slip condition ($\mathbf{u} = 0$) was applied at the autoclave walls, sample holder, samples and shaft (fluid-solid interfaces). A flow continuity was applied to the boundary between the rotating and static domains. The rotating speed was set to either 90, 180, 300 or 600 rpm, to achieve the flow velocities shown in Table 3.2.

The fluid was modelled as single-phase flow for both aqueous and supercritical CO_2 (water content is much smaller than the volume of CO_2) scenarios, assuming an incompressible fluid flow (speed of the flow is much smaller than the speed of sound) with density, ρ, of 994.3 [62] and 524.6 kg/m^3 [89] and dynamic viscosity, μ, of 71.9 [62] and 2.9 $\cdot 10^{-5}$Pa $\times$ s [90], used to replicate the aqueous and supercritical CO_2, respectively, at a temperature of 35 ^{o}C and pressure of 80 bar. It was also assumed there were no mechanical vibrations of the apparatus.

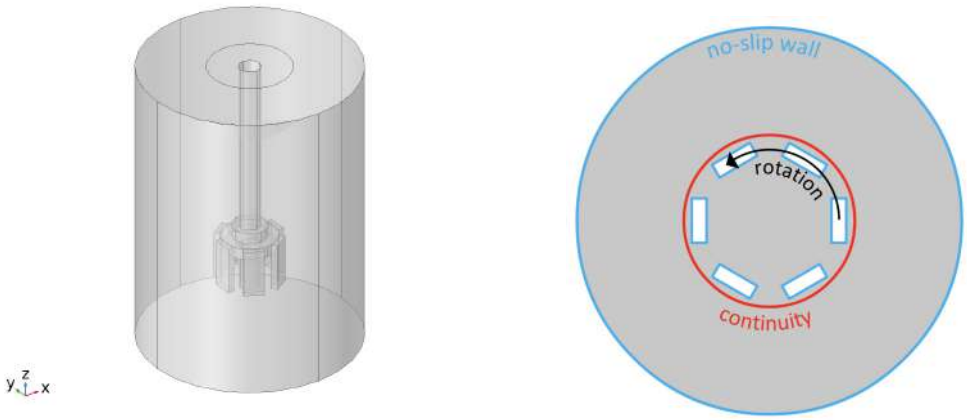

(a) (b)

Figure 3.6: Geometry of the CFD model used to simulate fluid flow and (b) sketch of the problem set-up on an horizontal section.

3.3.2 Model mesh

The $k-\varepsilon$ model uses wall functions to solve the fluid flow adjacent to the wall. Wall functions ignore the flow field in the buffer region and analytically compute a fluid velocity at the wall [75]. In order to achieve accurate results using wall functions a finer mesh was used adjacent to the walls to ensure that the dimensionless wall distance is appropriate (i.e. $y^+ \leqslant 11.06$) so that the first node falls outside the boundary layer region [62]. Tetrahedral elements were used for the bulk fluid flow domain and prismatic boundary elements were used adjacent to the wall (Figure 3.7a).

3.3.3 Model validation

3.3.3.1 Mesh sensitivity analysis

The quality of a mesh is the basis of a CFD simulation, as it directly influences the accuracy of the results. In order to obtain the precise results, it is necessary that a chosen mesh sufficiently fine to guarantee results with good resolution. However,

the finer the mesh, the longer the processing time required to compile the model. Therefore, a balance between the computational cost and the mesh density has to be considered when working with CFD simulations. [63, 78, 79]

A mesh sensitivity analysis was carried out to investigate the compromise between accuracy and computational cost. Figure 3.7b shows that the predicted velocity 0.5 mm ahead of the sample leading surface ($u_{leading}$) for a fixed rotating speed (600 rpm) did not change significantly after increasing the number of elements used in the mesh past 231,408. Therefore, such mesh resolution was deemed suitable, since the extra computational cost associated with the increasing the mesh density would not affect significantly the predicted results.

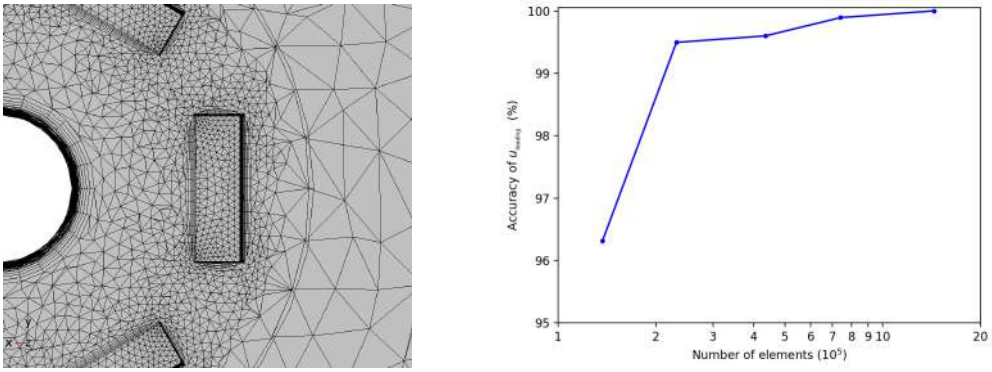

(a) (b)

Figure 3.7: Horizontal section of the mesh showing region adjacent to the sample and (b) mesh sensitivity study showing the predicted velocity 0.5 mm ahead of the sample leading surface as a percentage accuracy compared to the predicted velocity at the same position using the most refined mesh ($1,4 \times 10^6$ elements)

3.3.3.2 Flow structure analysis

To validate the flow structures observed, the velocity profiles along an horizontal mid-plane of the samples and wall shear stress profile on the sample surface are compared to previous literature results. Figure 3.8 compares the flow fields results to the ones calculated by Kumar et al. [91].

Although the size, shape and number of samples are different for this research, similar behaviour between both results can be observed. They both show that the highest velocity occurs in the region between the leading surface of a specimen and the trailing surface of the adjacent specimen, and that the fluid loses momentum as it moves away from the samples towards the stationary autoclave walls. The standard rotating cage design also includes a hole in the top and bottom plates of the cage to increase the turbulence on the inside surface of the coupon, but since the main focus in this study are the surfaces facing the outside of the cage, this was

not included in the design.

Figure 3.9 compares the wall shear stress results to the ones calculated by Kumar et al. [91] and Runstedtler et al. [92]. The higher wall shear stress values found near the leading surface are consistent with similar studies in the literature. For all of them, the higher velocity gradients near the leading face produce a region with higher shear stress near this face on both internal and external faces. It's worth noting that the maximum values observed are much lower than the adhesion strength of $FeCO_3$ film, and therefore, it would not be enough to cause damage to a film that has already fixed itself on the surface. [17]

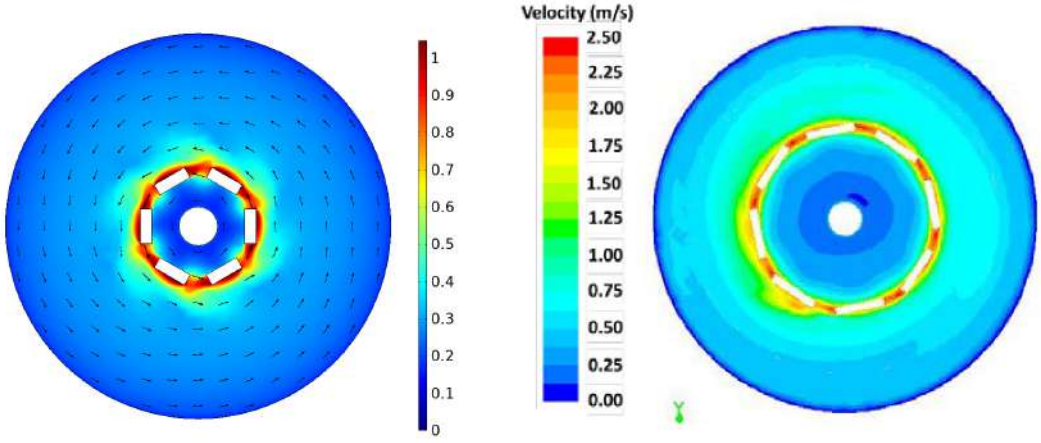

(a) (b)

Figure 3.8: CFD simulation velocity field results at horizontal mid-plane of the samples at 600 rpm, (a) from our model (arrows indicate flow direction) and (b) calculated by Kumar et al. [91].

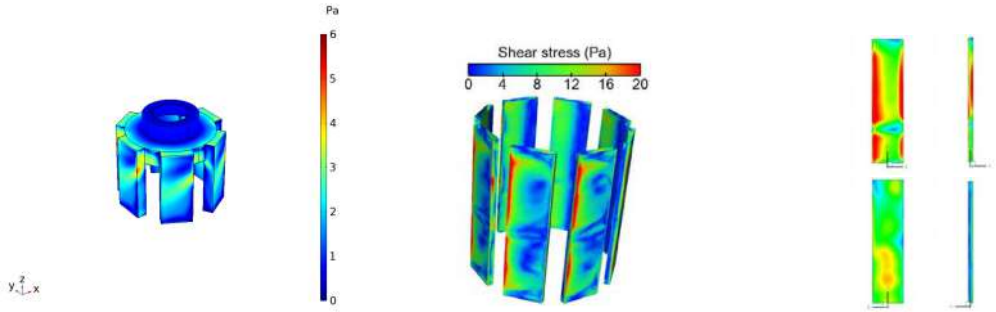

(a) (b) (c)

Figure 3.9: CFD simulation wall shear stress at 600 rpm, (a) from our model, (b) calculated by Kumar et al.[91] and (c) calculated by Runstedtler et al. [92].

3.3.4 Parametric study

The parametric study presented in this section seeks to use the CFD model developed previously to analyse the effect of each parameter on different hydrodynamic

parameters.

3.3.4.1 Effect of rotational speed

The influence of rotational speed was analysed by calculating the average fluid velocity along a line 0.5 mm ahead of the sample leading surface ($u_{leading}$) and the maximum wall shear stress on the sample surface facing the autoclave walls (τ_{max}). Figure 3.10 shows the predicted $u_{leading}$ as a function of rotational speed and clearly shows that fluid flow velocities near the sample surface increases linearly with rotational speed.

The mass transfer coefficient relates the rate of a diffusion-controlled reaction to the concentration driving force, including both diffusional and turbulent transport processes. By definition, the mass transfer coefficient in the concentration boundary layer (k_c) is inversely proportional to the thickness of the concentration boundary layer, the concentration boundary layer on the other hand is inversely proportional to the flow velocity to the power of a constant. Accordingly, $k_c \propto u^{0.5}$, for laminar flow and, $k_c \propto u^{0.8}$, for turbulent flow. [93, 94]

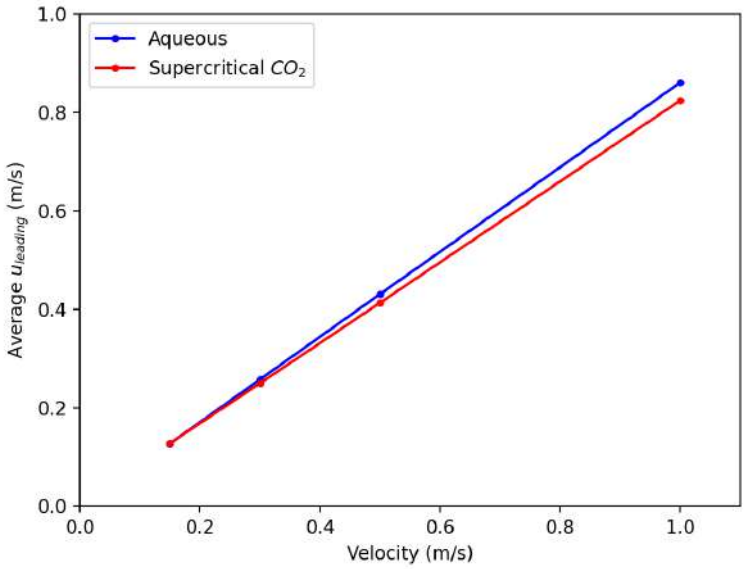

Figure 3.10: Predicted fluid velocity along a line 0.5 mm ahead of the sample leading surface ($u_{leading}$) as a function of rotational speed.

The fluid flow creates a wall shear stress on the sample surface that can be seen in Figure 3.9. The high velocity fields observed close to the leading and outer surfaces contribute to a high wall shear stress on these surfaces. Figure 3.11 displays the maximum predicted wall shear stress results as a function of rotational speed, showing that it increases exponentially with the rotational speed. However, the maximum predicted values values (5.4 and 1.8 Pa for aqueous and supercritical

CO_2, respectively) are much lower than the adhesion strength measured by Gao et al. [95] (1.5 – 9MPa), Schmitt et al. [96] (1 – 30MPa) and Schmitt et al. [97] (8.4–18.3MPa). Despite this, it can still significantly affect kinetic of film formation in these regions [17, 98].

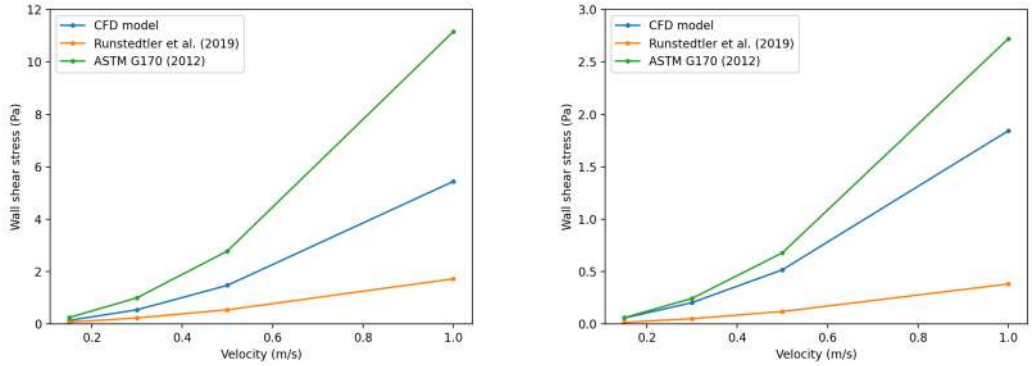

(a) (b)

Figure 3.11: Predicted maximum wall shear stress on the surface of the sample exposed to (a) aqueous and (b) supercritical CO_2 fluids at 35°C and 80bar as a function of rotational speed.

3.3.4.2 Droplet displacement

In the $scCO_2$ systems, the main focus is on the condensation of water droplets, since, according to the literature, corrosion will only occur on the area of the surface in direct contact with the water droplets. At any given time the steel samples exposed to water-saturated supercritical CO_2 are expected to be covered by a distribution of water droplets with different sizes. Their size distribution is controlled by the nucleation and growth rate (condensation rate) and by the forces acting on them (such as: gravity, drag and centrifugal forces), that may lead to their removal from the surface.

Zhang et al. [99] mechanistic droplet formation model allows the calculation of the lifetime, or critical radius, of the droplets before they slide away, fall down or detach from a surface based on the forces acting on its volume (Figure 3.12a).

The drag force (F_d^x) represents the force exerted on a body by the flowing fluid, and is given by Equation (3.6) where D_d is the drag coefficient, A is the frontal area of the droplet, and V_g is the gas velocity. The drag coefficient (C_d) depends on the shape of the body and Reynolds number, but for the ones considered it is typically 0.44. [99]

$$F_d^x = \frac{1}{2} C_d \rho_g A V_g^2 \tag{3.6}$$

The friction force (F_f^x) represents the adhesion between droplet and the sample wall that opposes the drag force and keeps the droplet in place. It is given by Equation (3.7), where γ is the surface tension, r is the droplet radius and k_f is the friction coefficient, which is a function of the surface roughness, and can be aproximated as 1.5. [99]

$$F_f^x = F_f^y = k_f \gamma r \tag{3.7}$$

The gravity force (F_g^y) tends to pull the droplet downwards as to make it slide down and fall, and is given by Equation (3.8). [99]

$$F_g^y = \rho \frac{4}{6} \pi r^3 g \tag{3.8}$$

The buoyancy (F_b^y) for a suspended hemispherical droplet can be calculated using Equation (3.9), where ρ_g is the gas density. [99]

$$F_b^y = \frac{4}{6} \pi r^3 \rho_g \tag{3.9}$$

The centrifugal force acts on objects in a rotating frame of reference, and is directed radially outwards from the rotation axis. The magnitude of centrifugal force is given by Equation (3.10), where V_t is the tangential velocity and r_{cage} is the cage radius. [99]

$$F_c^z = \rho \frac{4}{6} \pi r^3 \frac{V_t^2}{r_{cage}} \tag{3.10}$$

The surface tension force (F_γ^z) keeps the droplet attached to the wall, and is given by Equation (3.11). [99]

$$F_\gamma^y = \pi r^2 \frac{2\gamma}{r} \tag{3.11}$$

All the forces shown are a function of the droplet radius, but they increase at different rates. For small droplets the forces that hold it in place (surface tension and friction) are much larger than the others, so the droplet remains stationary on the surface. As the droplet grows due to condensation, the forces that are proportional to the volume increase faster, until a critical size is reached, at which the droplet will begin to move. Figure 3.12b shows the critical radius in each direction as a function of the tangential velocity. The direction in which the critical radius (R_c) has the lowest value will control the motion mechanism. If the force balance in y direction is reached first, the droplet will slide along the sample surface in the direction of the flow. If the force balance in z direction is reached first, the droplet will fall down due to the gravity force. If the force balance in x direction is reached first, the droplet will detach from the surface due to the centrifugal forces.

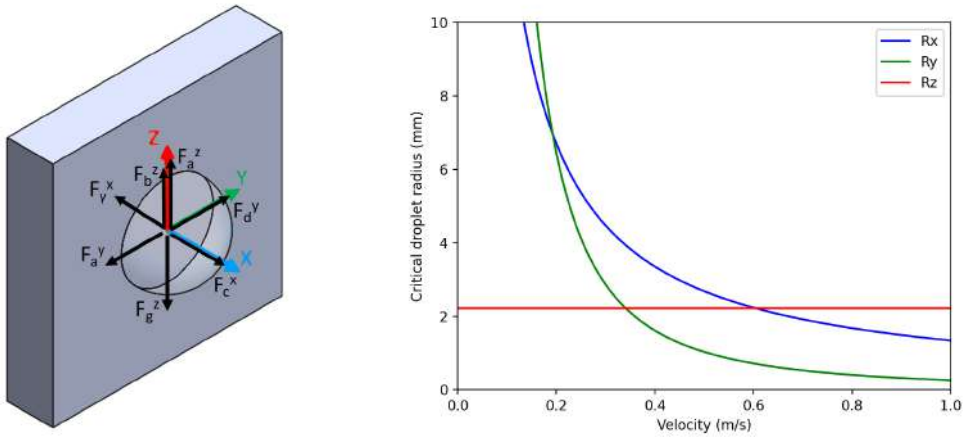

(a) (b)

Figure 3.12: (a) Force analysis on a single droplet. F_c^x: centrifugal force; F_γ^x: surface tension force; F_d^y: flow drag force; F_b^z: buoyancy; F_g^z: gravity force; F_a^y and F_a^z: friction force between the liquid droplet and the solid wall and (b) critical droplet size as a function of the supercritical CO_2 velocity for the proposed test setup at 35 ^oC and 80 bar.

4. Results and discussion

This chapter presents the experimental results from the corrosion behaviour of X80 steel in high CO_2 partial pressure environments, to simulate conditions that may occur in the CO_2 injection field conditions for CO_2-EOR. The effect of fluid flow on CO_2 corrosion behaviour of X80 steel at 35 ^oC and 80 bar was studied using an adapted rotating cage setup followed by a detailed assessment of both corrosion product morphology and general/localised corrosion behaviour. The test matrix is listed in Table 3.2 and the results in each fluid (aqueous and supercritical CO_2) were analysed separately because the predominant corrosion mechanism differ.

4.1 Samples exposed to CO_2-saturated water

This section focus on understanding the effect of the supercritical CO_2-saturated water flow on both general and localised corrosion of X80 steel simulating conditions where significant amount of water is present in the CO_2 transportation pipeline. It focus on the role of the fluid flow and brine chemistry and how these parameters influences the corrosion product scale morphology and its protectiveness in reducing the overall X80 steel corrosion rates.

4.1.1 Surface analysis

4.1.1.1 X-ray diffraction

Figures 4.1, 4.2 and 4.3 shows the XRD patterns of the samples immersed in brines with different Ca^{2+} concentrations (0, 1000 and 5000 ppm) at 35 ^oC and 80 bar for 48 or 96 h and distinct fluid velocity fields. All the XRD patterns of the samples tested exhibit the characteristic XRD peaks of α-iron that can be associated with the steel substrate.

The XRD patterns for the samples exposed for 48 h shows mainly the peaks associated with the steel substrate and barely any surface film could be resolved, indicating that the surface film could be too thin to resolve by this technique. However, the XRD patterns for the samples exposed for 96 h show other narrow sharp peaks besides the ones associated with the steel substrate, indicating that the cor-

rosion product on the surface is crystalline.

Results show that the main by-product in the corrosion of carbon steel in presence of only CO_2 is the formation of an iron carbonate film ($FeCO_3$). Evidenced by the peaks associated with the corrosion products of the samples exposed to the

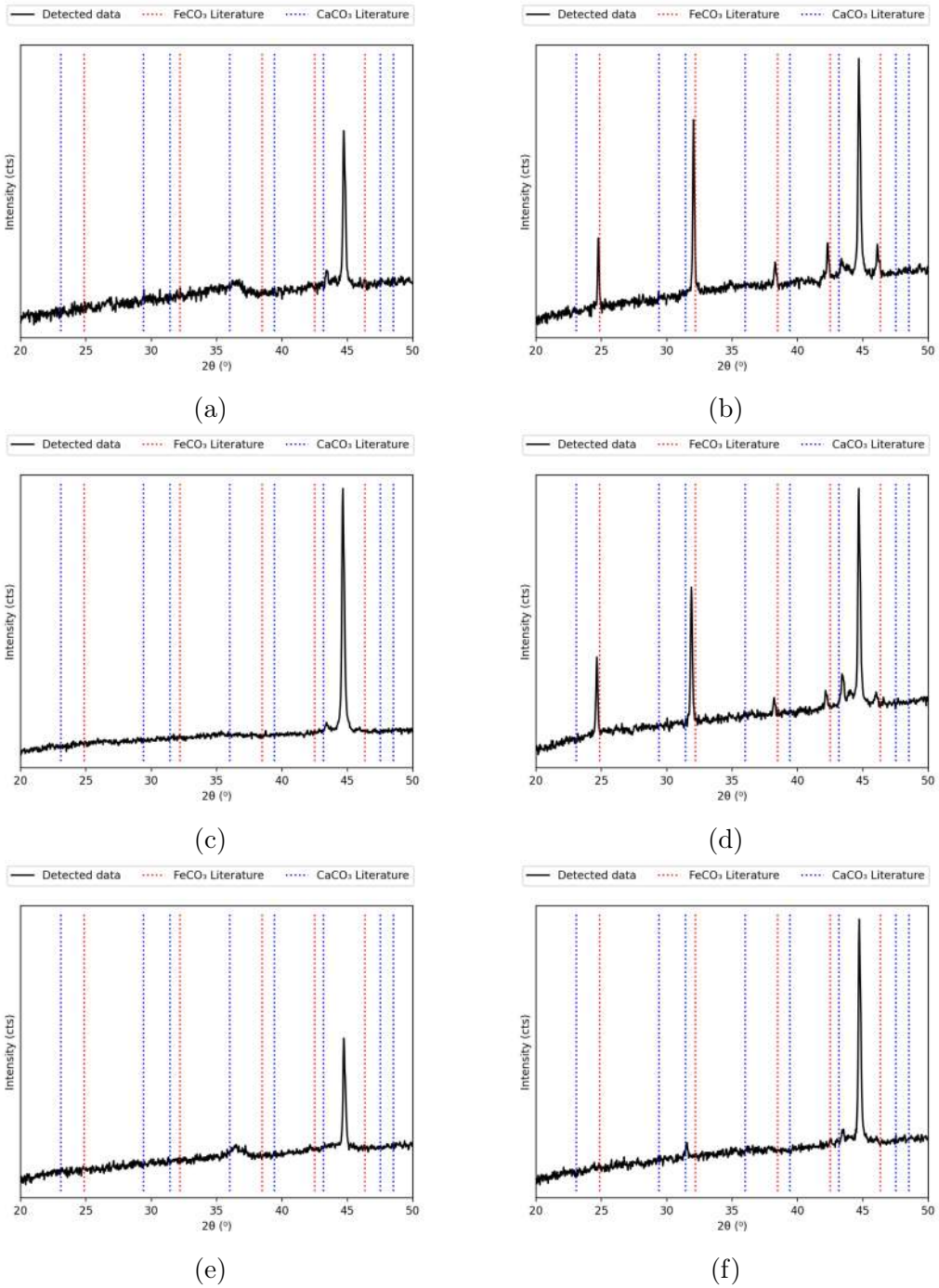

Figure 4.1: XRD patterns collected from X80 carbon steel surfaces exposed to a CO_2-saturated brines at 35 ^{o}C and 80 bar for different exposure time and brine composition, (a) 0 ppm Ca^{2+} for 48 h, (b) 0 ppm Ca^{2+} for 96 h, (c) 1000 ppm Ca^{2+} for 48 h, (d) 1000 ppm Ca^{2+} for 96 h, (e) 5000 ppm Ca^{2+} for 48 h, (f) 5000 ppm Ca^{2+} for 96 h and a flow of 0 m/s.

brine without Ca^{2+} being aligned with the $FeCO_3$ peaks in the literature.

However, addition of Ca^{2+} results in the $FeCO_3$ peaks position shifting to lower values of 2ϑ with increasing Ca^{2+} addition. Given that $FeCO_3$ and $CaCO_3$ share a hexagonal lattice structure, the introduction of Ca into $FeCO_3$ matrix increases

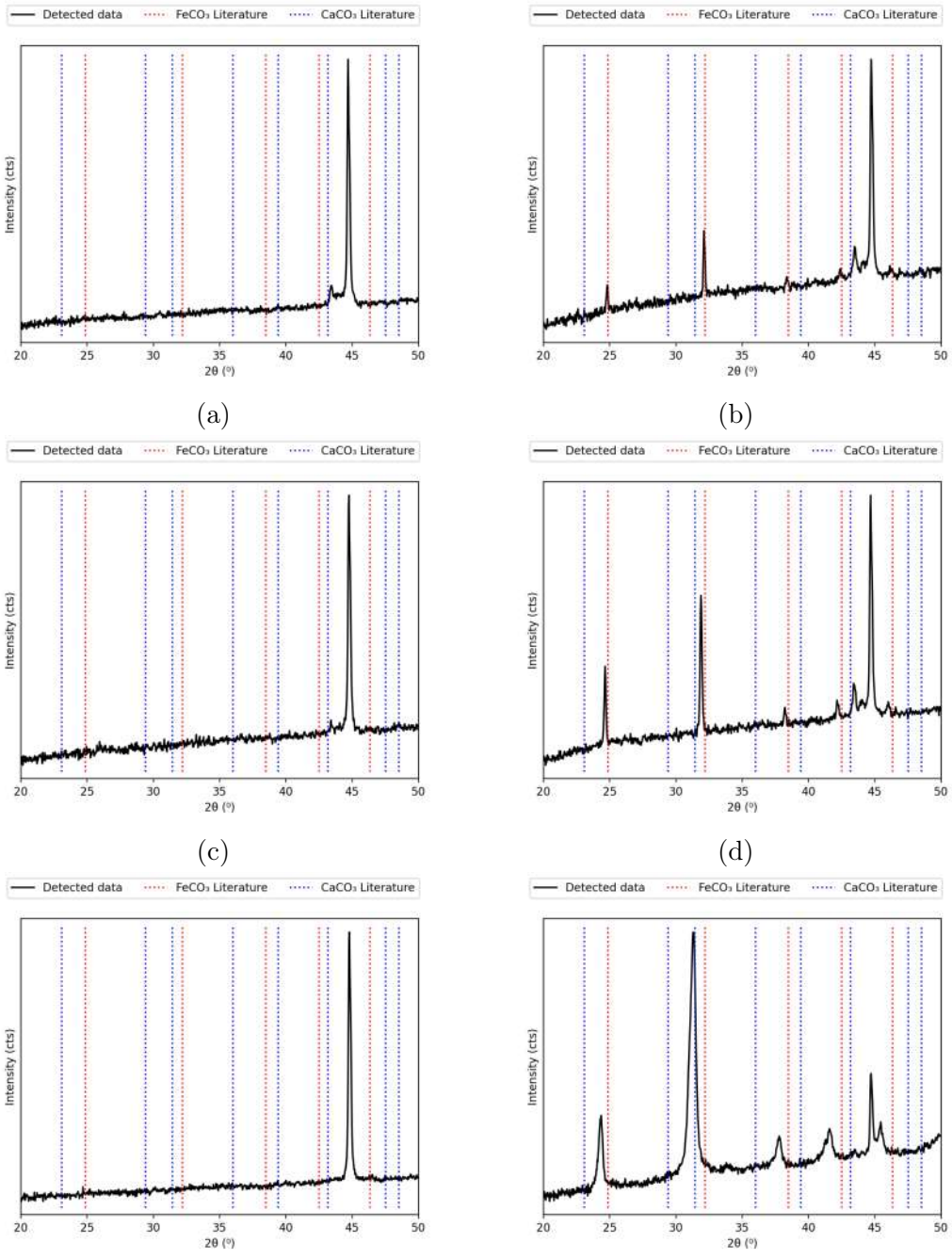

Figure 4.2: XRD patterns collected from X80 carbon steel surfaces exposed to a CO_2-saturated brines at 35 ^{o}C and 80 bar for different exposure time and brine composition, (a) 0 ppm Ca^{2+} for 48 h, (b) 0 ppm Ca^{2+} for 96 h, (c) 1000 ppm Ca^{2+} for 48 h, (d) 1000 ppm Ca^{2+} for 96 h, (e) 5000 ppm Ca^{2+} for 48 h, (f) 5000 ppm Ca^{2+} for 96 h and a flow of 0.5 m/s.

in the inter-planar spacing, that therefore, shifts the peaks position associated with those crystalline planes towards lower values of 2ϑ. Based on this, Equation 3.4 can be used to calculate the mole fraction of Ca within the mixed iron-calcium carbonate based on the shift in the (104) peak as shown in Figure 4.15. Confirming not only

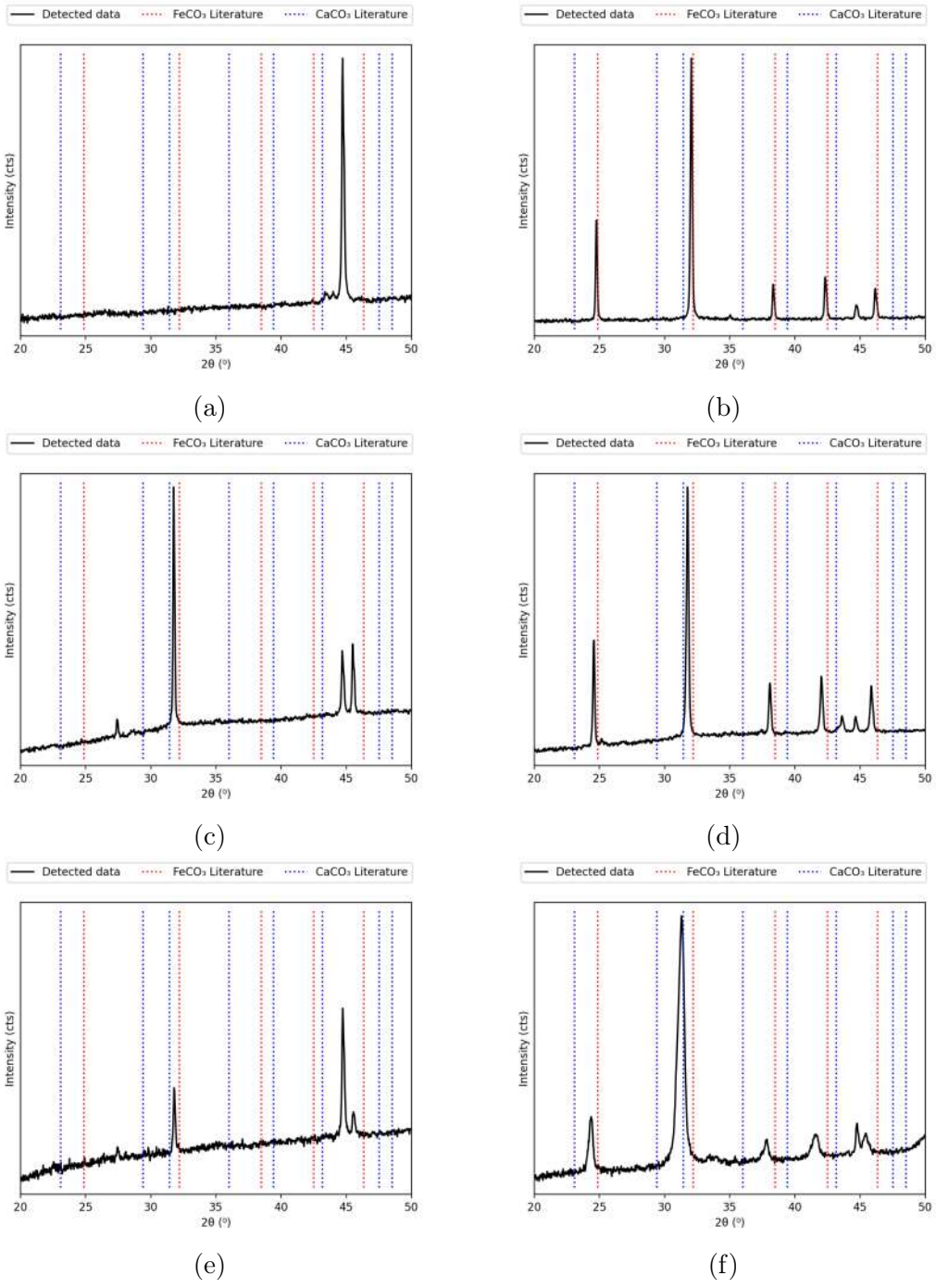

Figure 4.3: XRD patterns collected from X80 carbon steel surfaces exposed to a CO_2-saturated brines at 35 ^oC and 80 bar for different exposure time and brine composition, (a) 0 ppm Ca^{2+} for 48 h, (b) 0 ppm Ca^{2+} for 96 h, (c) 1000 ppm Ca^{2+} for 48 h, (d) 1000 ppm Ca^{2+} for 96 h, (e) 5000 ppm Ca^{2+} for 48 h, (f) 5000 ppm Ca^{2+} for 96 h and a flow of 1.0 m/s.

the co-precipitation of $FeCO_3$ and $CaCO_3$ after 96 h of exposure, but also that the ratio of carbonates in the scale composition is influenced by the brine composition.

4.1.1.2 Scanning electron microscopy

Figures 4.4, 4.5 and 4.6 shows SEM images of the surface of corroded X80 steel samples immersed in brines with different Ca^{2+} concentrations (0, 1000 and 5000 ppm) at 35 ^{o}C and 80 bar for 48 or 96 h and exposed to distinct fluid flow velocities.

After 48 h regions with two distinct morphologies can be observed on the sample surface regardless of the fluid flow conditions they were exposed to. An inner layer associated with a porous iron carbide (Fe_3C) structure created in the initial steps of the CO_2 corrosion of steels, by a selective dissolution of the ferrite phase within the steel microstructure [87]. On top of that a thin amorphous layer rich in Fe, C and O (based on EDX measurements) partially covers the Fe_3C network, which appears to be more homogeneous as Ca^{2+} content in the brine increases. Both of these layers couldn't be resolved by the XRD measurements, where only the substrate $\alpha - Fe$ peaks could be perceived.

However, after 96 h the samples exposed to the brine without flow exhibited a partial coverage of prismatic crystals whose morphology is typical of carbonate crystals [5, 100] growing on top of the amorphous layer. This also indicates that the surface scale might not be fully developed yet, and for exposure times longer than the considered in this study the film would have more opportunity to grow, further reducing the measured corrosion rates.

The growth of this crystalline $FeCO_3$ layer becomes more apparent when exposed to a fluid flow for 96 h, where some of the samples exhibited a fully $FeCO_3$ coverage, such as the samples exposed to: a fluid flow velocity of 0.5 m/s and a brine composition of 5000 ppm Ca^{2+} (Figure 4.5f) and fluid flow velocity of 1.0 m/s and a brine composition of 0, 1000 and 5000 ppm Ca^{2+} (Figures 4.6b, 4.6d and 4.6f, respectively). This result is in agreement with previous literature observations [61] that bellow a certain critical velocity, the fluid flow can enhance transport of species towards and away from the metal surface, leading to an increased corrosion rate as observed in Figure 4.10, due to the decrease of local pH near the surface. However, no chemical (dissolution) or mechanical damage could be observed, indicating that the fluid flows condition tested were bellow the critical velocity required to damage the $FeCO_3$ scale.

After 96 h of exposure time the samples were taken for further analysis of its corrosion product composition and morphology through the use of Focused Ion Beam (FIB) etching. Figures 4.7, 4.8 and 4.9 shows SEM images of the cross-sections of the corrosion product scales on X80 steel samples exposed to brines containing different Ca^{2+} concentrations (0, 1000 and 5000 ppm) at 35 ^{o}C and 80 bar for 96 h.

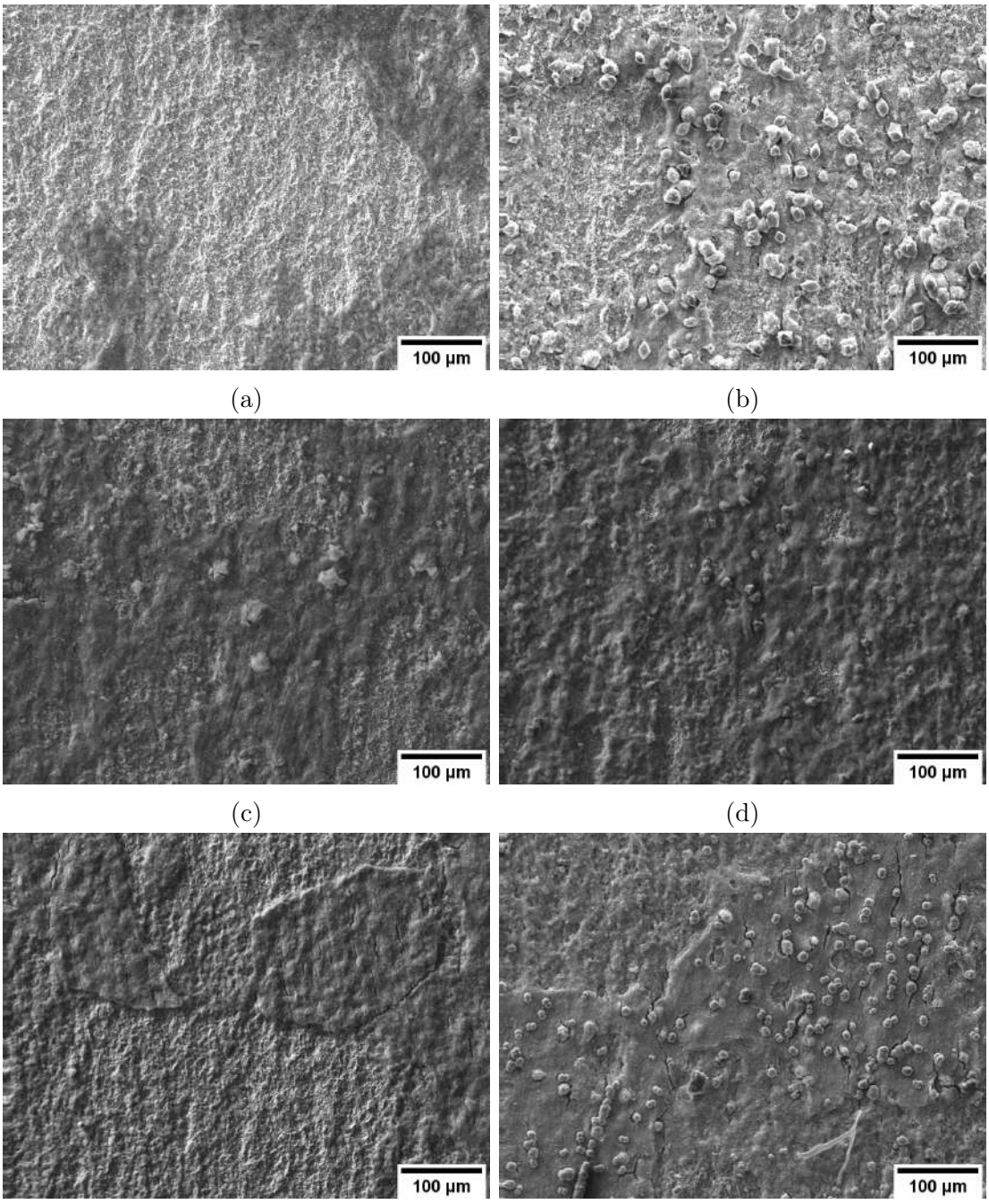

Figure 4.4: SEM images of X80 carbon steel exposed to a CO_2-saturated brines at 35 ^{o}C and 80 bar for different exposure times and brine composition, (a) 0 ppm Ca^{2+} for 48 h, (b) 0 ppm Ca^{2+} for 96 h, (c) 1000 ppm Ca^{2+} for 48 h, (d) 1000 ppm Ca^{2+} for 96 h, (e) 5000 ppm Ca^{2+} for 48 h, (f) 5000 ppm Ca^{2+} for 96 h without fluid flow.

All samples exhibited voids at the interface between the corrosion product film and steel substrate. This is most likely, a result of the continued steel surface corrosion under the film, indicative of film undermining [101], a process known to form porous and unprotective films.

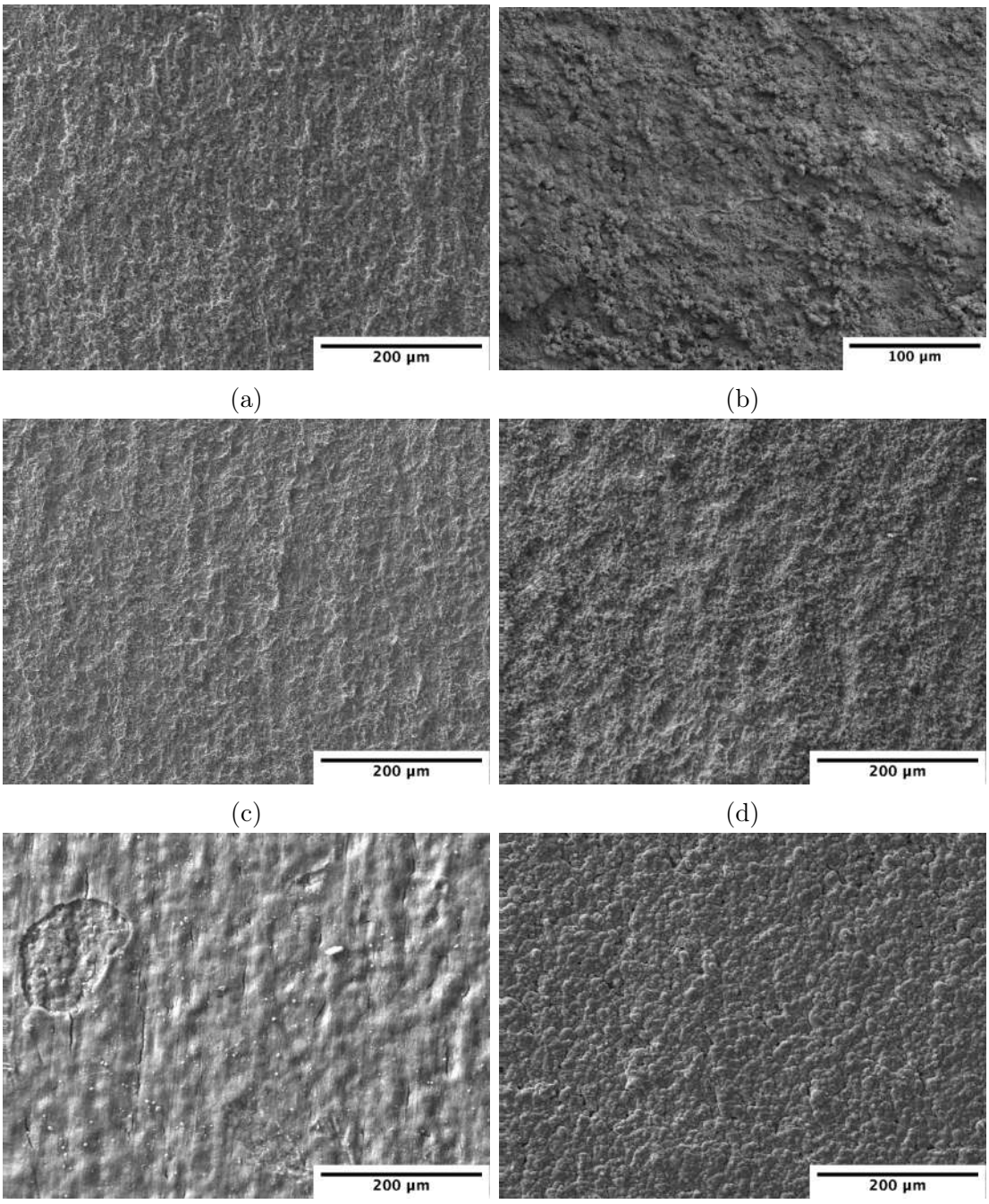

(a) (b)

(c) (d)

(e) (f)

Figure 4.5: SEM images of X80 carbon steel exposed to a CO_2-saturated brines at 35 ^{o}C and 80 bar for different exposure times and brine composition, (a) 0 ppm Ca^{2+} for 48 h, (b) 0 ppm Ca^{2+} for 96 h, (c) 1000 ppm Ca^{2+} for 48 h, (d) 1000 ppm Ca^{2+} for 96 h, (e) 5000 ppm Ca^{2+} for 48 h, (f) 5000 ppm Ca^{2+} for 96 h and a flow of 0.5 m/s.

Samples tested without flow exhibited a highly porous corrosion product film rich in Fe, C and O (based on EDX measurements). The film ranged from 1.8 to 9.4 µm in thickness. The porous morphology is not noticeable from SEM images of the top view, but it is commonly considered unprotective because it allows the species

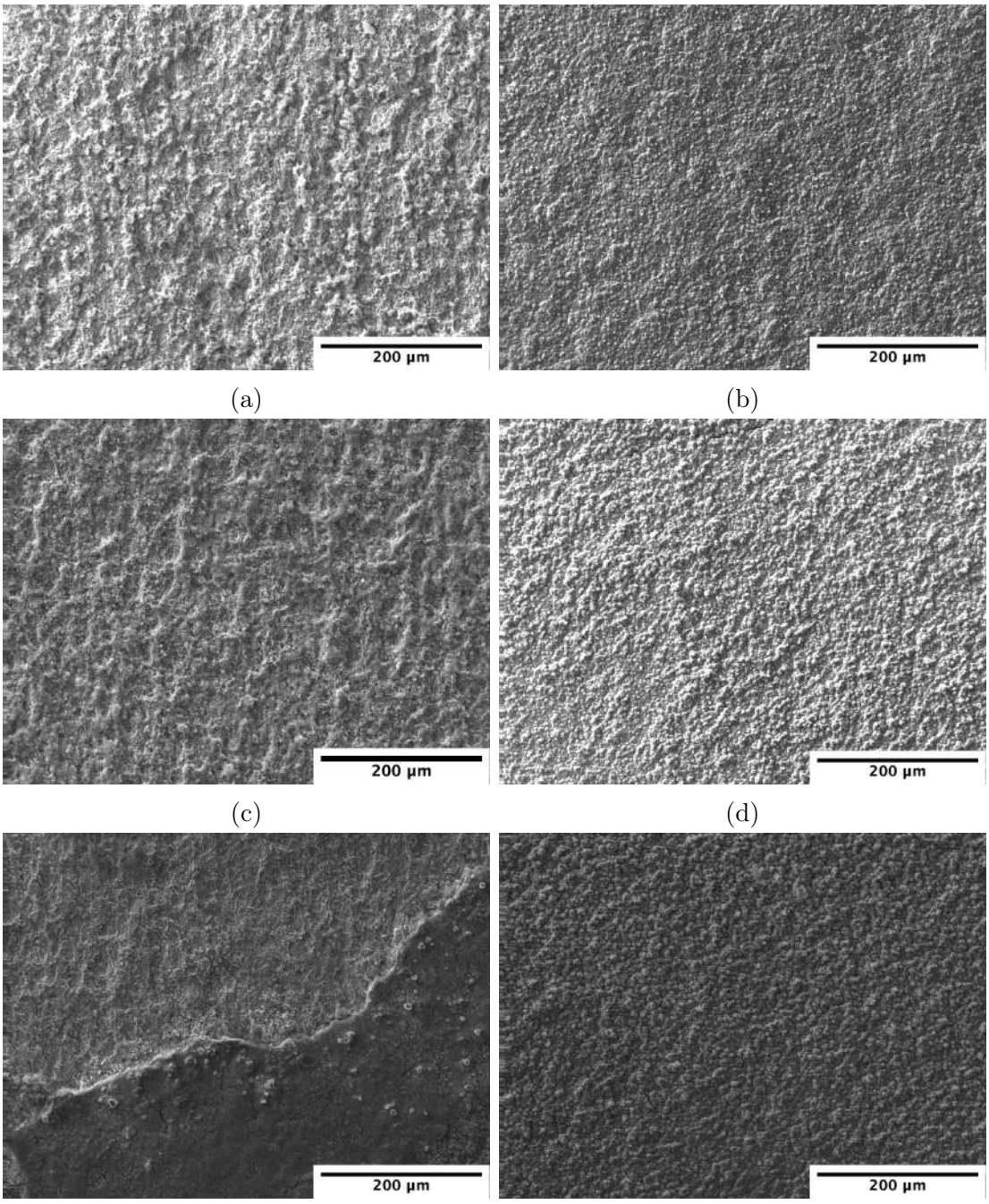

(a) (b)

(c) (d)

(e) (f)

Figure 4.6: SEM images of X80 carbon steel exposed to a CO_2-saturated brines at 35 ^{o}C and 80 bar for different exposure times and brine composition, (a) 0 ppm Ca^{2+} for 48 h, (b) 0 ppm Ca^{2+} for 96 h, (c) 1000 ppm Ca^{2+} for 48 h, (d) 1000 ppm Ca^{2+} for 96 h, (e) 5000 ppm Ca^{2+} for 48 h, (f) 5000 ppm Ca^{2+} for 96 h and a flow of 1.0 m/s.

to easily diffuse through this layer.

When increasing the fluid flow velocity to 0.5 m/s, the corrosion product film changed so that it consisted of a thinner porous layer, ranging from 0.9 to 4.1 µm, combined with some compact $FeCO_3$ crystals distributed on top of the porous

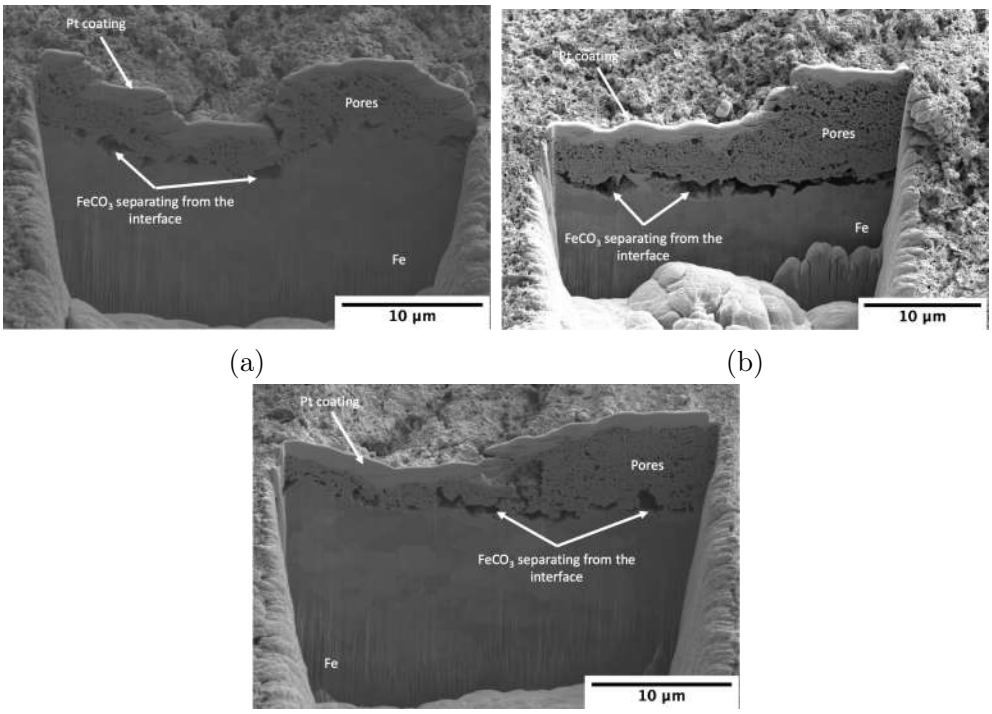

Figure 4.7: SEM cross-section images of X80 carbon steel exposed to a CO_2-saturated brines with different composition, (a) 0 ppm, (b) 1000 ppm and (c) 5000 ppm Ca^{2+} without fluid flow at 35 ^{o}C and 80 bar for 96 h.

layer. The amount of these $FeCO_3$ crystals appears to increase as Ca^{2+} content in the brine increases to the point that at 5000 ppm Ca^{2+} the corrosion product scale is composed almost entirely of $FeCO_3$ crystals.

When exposed to a fluid flow of 1.0 m/s, the SEM images show that the film formed is considerable thicker (>5.9 µm) and more compact than those at lower fluid flows, agreeing with the measured scale XRD peak intensities relative to the steel substrate XRD peak intensities. No traces of the inner porous layer could be observed, suggesting that either its formation was inhibited by the fluid flow or that the mechanical erosion forces generated by fluid flow was able to clear the brittle porous layer allowing the $FeCO_3$ crystals to deposit directly on top of the bare steel substrate.

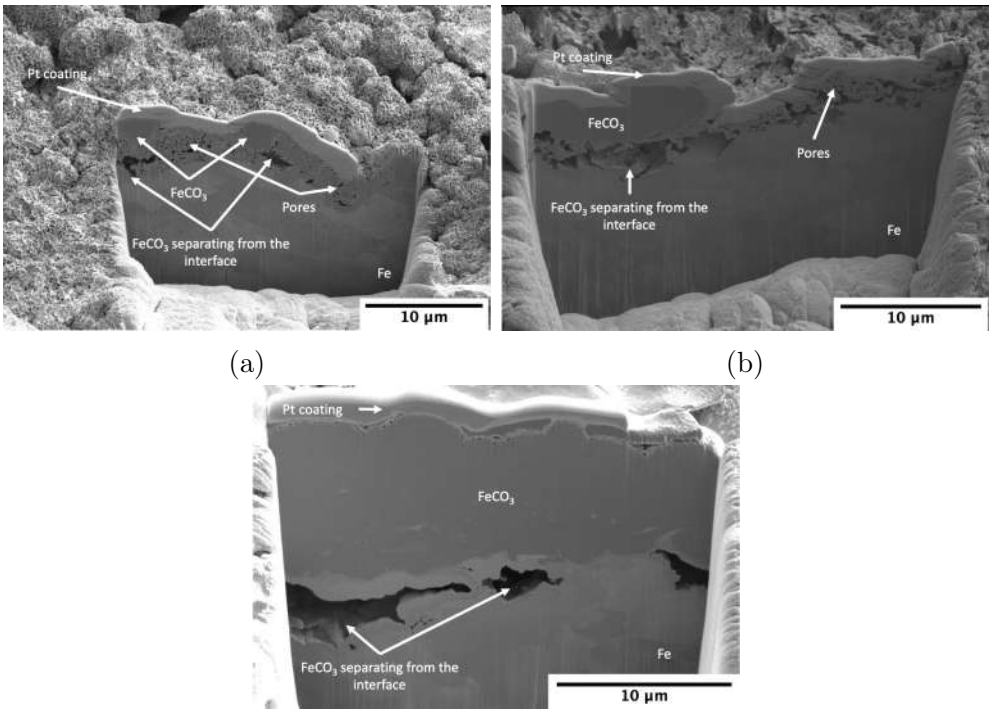

(a) (b)

(c)

Figure 4.8: SEM cross-section images of X80 carbon steel exposed to a CO_2-saturated brines with different composition, (a) 0 ppm, (b) 1000 ppm and (c) 5000 ppm Ca^{2+} and a fluid flow velocity of 0.5 m/s at 35 ^{o}C and 80 bar for 96 h.

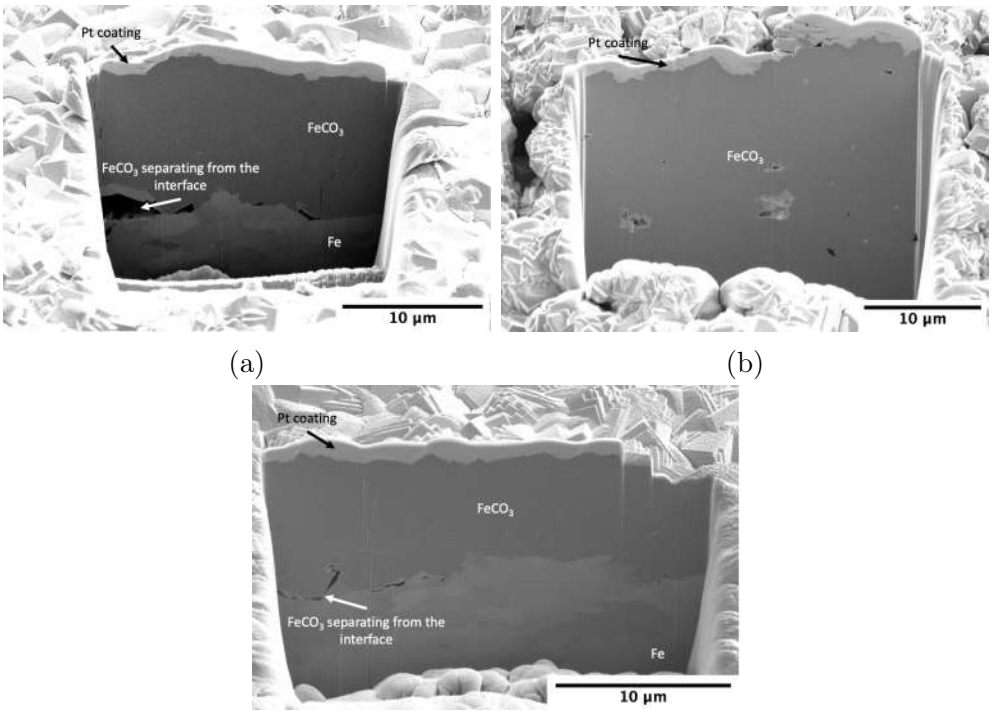

(a) (b)

(c)

Figure 4.9: SEM cross-section images of X80 carbon steel exposed to a CO_2-saturated brines with different composition, (a) 0 ppm, (b) 1000 ppm and (c) 5000 ppm Ca^{2+} and a fluid flow velocity of 1.0 m/s at 35 ^{o}C and 80 bar for 96 h.

4.1.2 Mass loss measurements

Figure 4.10 shows the calculated corrosion rates and corrosion product mass determined from mass loss measurements as a function of time and Ca^{2+} content in the brine for X80 carbon steel exposed to a CO_2-saturated brine at 35 ^{o}C and 80 bar. All conditions exhibited a very high average corrosion rate over the entire test duration.

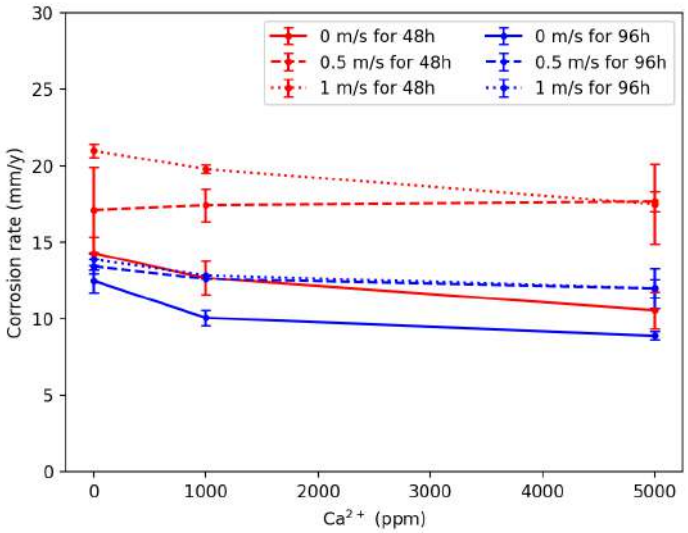

Figure 4.10: Average corrosion rates of X80 steel exposed to a CO_2-saturated brine at 35 ^{o}C and 80 bar as a function of time, Ca^{2+} content in the brine and fluid flow velocities.

After 48 h without flow, the addition of 1000 or 5000 ppm Ca^{2+} reduced the corrosion rate from 14.8 mm/year to 13.3 and 10.9 mm/year, respectively. The decrease of average corrosion rate in the brines containing a higher Ca^{2+} content seems to indicate that the presence of Ca^{2+} is either increasing the kinetics of corrosion scale formation or modifying the corrosion scale morphology to be more compact and protective. The presence of Ca^{2+} in the brine is also expected to promote the co-precipitation of $CaCO_3$ and $FeCO_3$, modifying the morphology and chemical properties of the corrosion product [51, 56]. It can be observed that the total scale mass increase from 0.008 to 0.011 g as the Ca^{2+} content in the brine increases from 0 to 5000 ppm for the same test condition. The corrosion rate is also shown to decrease in conjunction with an increase corrosion scale mass as the Ca^{2+} content in the brine increases. Therefore, it can be deduced that one of the key factors controlling the reduction of corrosion rate may be the precipitation and growth of corrosion scale on the surface of the material.

This assumption is further corroborated by the longer exposure tests (96 h), which show an increased corrosion product mass on the surface combined with a

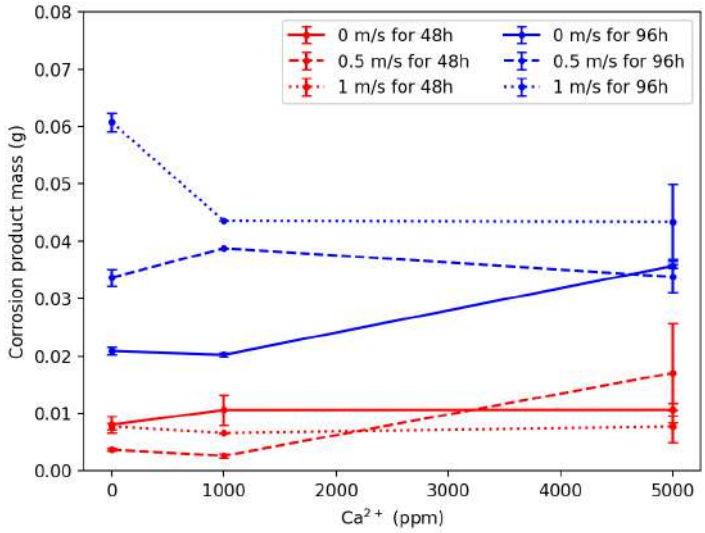

Figure 4.11: Total corrosion product mass on the surface of X80 steel exposed to a CO_2-saturated brine at 35 ^{o}C and 80 bar as a function of time, Ca^{2+} content in the brine and fluid flow velocities.

reduction in average corrosion rate in contrast to the tests carried out for 48 h for all Ca^{2+} contents and fluid flow velocities. Suggesting that the precipitation and growth of the corrosion product scale for longer exposure times is assisting in the reduction of the average corrosion rates.

4.1.3 Electrochemical properties of corrosion scales

As the test time progresses, the species formed/consumed in the corrosion electrochemical reactions are expected to change the brine chemistry, surface pH and bulk pH over time [84]. Such that at the end of the test period the test cell will have a complex chemical composition which is highly dependent on the initial conditions. This scenario would impose a challenge to compare the electrochemical properties corrosion scales formed under different test conditions. Therefore, to eliminate influence from brine chemistry, it was decided that after each test, one of the corroded samples was transferred to a cell containing a standardized brine (CO_2-saturated 30 g/L NaCl solution at 25 ^{o}C, room pressure and pH 3.8), to investigate the electrochemical properties of the corrosion scales using linear polarization resistance and potentiodynamic polarization techniques. The polarization curves of corrosion scales formed in brines with different Ca^{2+} content for 48 and 96 h at 35 ^{o}C and 80 bar are shown in Figure 4.12 and the average corrosion rate calculated from the electrochemical measurements are show in Figure 4.13 while corrosion potential (E_{corr}), corrosion current density (i_{corr}), anodic Tafel slopes (B_a), cathodic Tafel slope (B_c) and polarization resistance (R_p) are shown in Table 4.1.

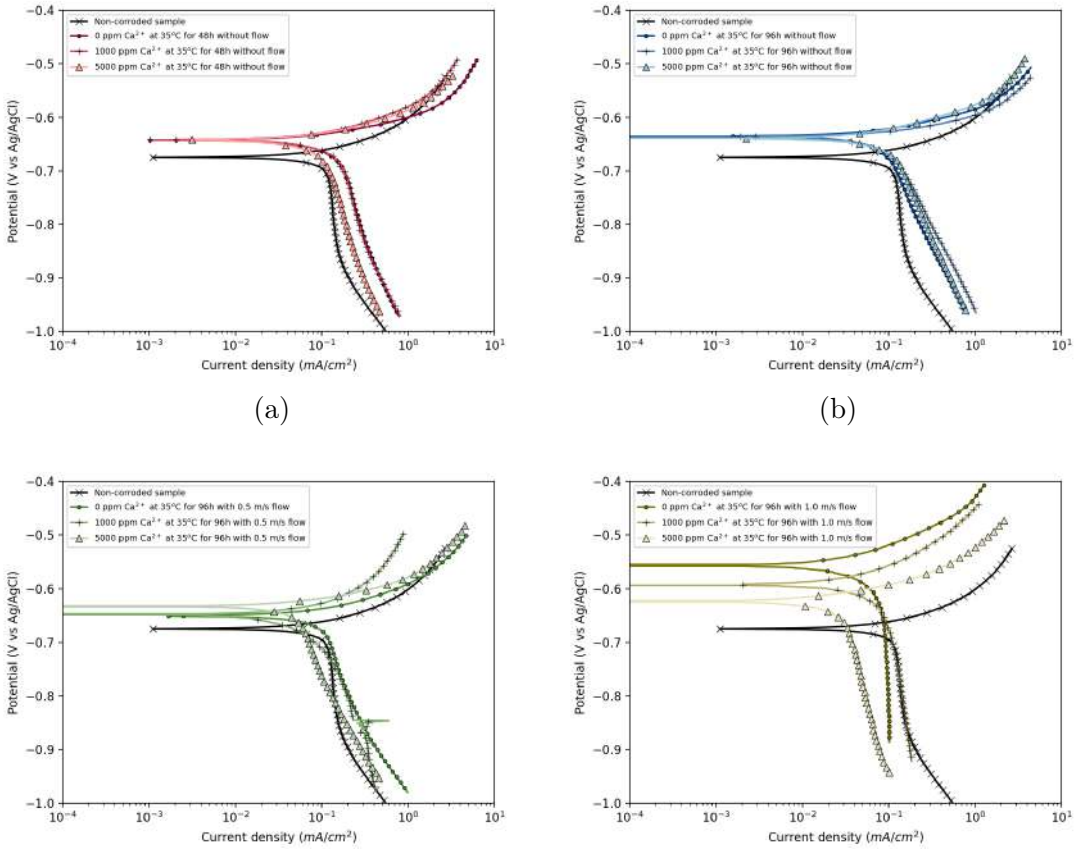

Figure 4.12: Potentiodynamic polarization curves carried out in 30g/L NaCl solution at 25 ^{o}C of X80 steel samples pre-corroded at 35 ^{o}C and 80 bar in brines containing 0, 1000 or 5000 ppm Ca^{2+}.

Table 4.1: Potentiodynamic electrochemical parameters for the corrosion of X80 steel in 30g/L NaCl solution at 25 ^{o}C.

Pre-corrosion condition				E_{corr} (mV) vs Ag/AgCl	i_{corr} (mA/cm^2)	Ba (mV/dec)	Bc (mV/dec)	R_p ($\Omega \cdot$ cm^2)
T (^{o}C)	t (h)	P (bar)	Ca^{2+} (ppm)					
Non-corroded sample				-675	0.071 ± 0.003	80	600	184 ± 8
35	48	80	0	-643	0.149 ± 0.012	61	277	169 ± 4
			1000	-642	0.109 ± 0.018	56	225	179 ± 12
			5000	-642	0.094 ± 0.020	55	225	208 ± 31
	96		0	-635	0.116 ± 0.023	55	220	168 ± 34
			1000	-636	0.111 ± 0.032	75	180	216 ± 63
			5000	-640	0.084 ± 0.007	50	250	221 ± 19
			0	-651	0.139 ± 0.012	60	290	155 ± 14
			1000	-648	0.086 ± 0.031	100	130	306 ± 110
			5000	-633	0.066 ± 0.002	60	250	319 ± 13
			0	-557	0.089 ± 0.008	67	210	250 ± 23
			1000	-593	0.064 ± 0.010	75	300	409 ± 64
			5000	-623	0.018 ± 0.002	50	290	1011 ± 132

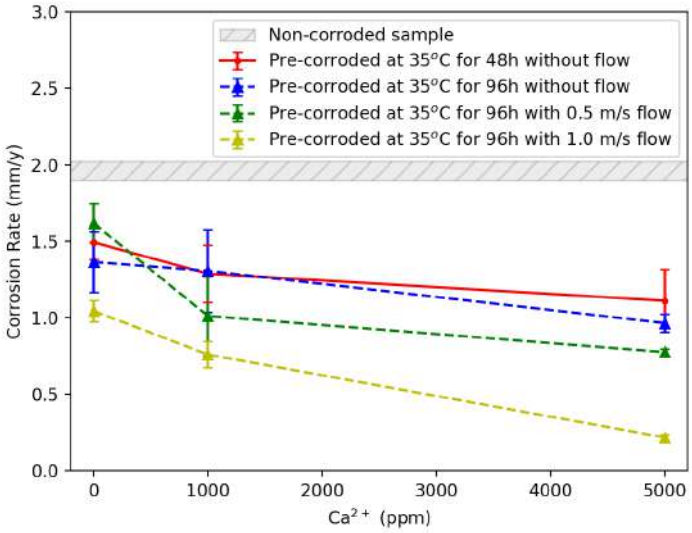

Figure 4.13: Average corrosion rate calculated from electrochemical measurements in 30g/L NaCl solution at 25 ^{o}C of X80 steel samples pre-corroded at 35 ^{o}C and 80 bar in brines containing 0, 1000 or 5000 ppm Ca^{2+}.

The corrosion potential of the pre-corroded samples is shown to be shifted to nobler regions when compared to a non-corroded sample. This can be indicative of the presence of a corrosion product layer formation at the steel-electrolyte interface. But, no signs of passivation could be observed for the anodic potential range scanned.

The potentiodynamic polarization curves seem to overlap for the samples pre-corroded without flow, suggesting that neither the Ca^{2+} content up to 5000 ppm nor the longer exposure time (from 48 to 96 h) influenced the anodic or cathodic reaction process in this environment. However, the samples pre-corroded with fluid flow exhibited potentiodynamic curves shifted to lower current densities indicating a higher degree of corrosion resistance when compared to the samples pre-corroded without flow.

Figure 4.13 shows that the corrosion rate slightly decreased for higher Ca^{2+} content in the pre-corrosion brine and for higher flow rates. The corrosion rate of the samples covered by a scale formed after 96 h without flow and with a 1.0 m/s fluid flow dropped from 1.49 to 1.11 and 1.04 to 0.22 mm/year, respectively, when immersed in a brine containing 0 and 5000 ppm of Ca^{2+} respectively. This decrease in corrosion rate is assumed to be the result of the formation of a protective scale composed of mixed iron-calcium carbonate ($Fe_xCa_yCO_3$), which slows down the corrosion rate, by acting as a diffusion barrier for the species involved in the electrochemical reactions, preventing the substrate from undergoing further dissolution [54].

4.1.4 Discussion

Based on the information provided in in this work, the contribution of the fluid flow on the corrosion of carbon steel in high CO_2 partial pressure environments can be divided in a number of steps depending on the main phase present.

4.1.4.1 Corrosion process

Understanding the nucleation and growth mechanism of the corrosion product film and its characteristics is essential in assessing pipelines lifetime. From the results presented in Section 4.1, the effect of fluid flow and brine chemical composition on the development and protectiveness of the carbonate corrosion product layer have been studied. The CO_2 corrosion mechanisms of carbon steel under flow conditions is illustrated in Figure 4.14.

1. Equilibrium in CO_2 systems:

In CO_2 – H_2O systems, CO_2 can dissolve in water, where it is hydrated to form carbonic acid H_2CO_3, which then dissociates to HCO_3^- and H^+, as shown in Equations 2.1 to 2.3. Since these chemical reactions are linked via common species (such as H^+) changing any one concentration will shift the equilibrium concentration for all the others.

2. Selective dissolution:

When a carbon steel is in contact with such aqueous environment the corrosion processes will occur in accordance with two types (anodic and cathodic) of reactions, as shown in Equations 2.4 to 2.6, releasing Fe^{2+}. In the early stages of the corrosion process, due to the dual-phase structure nature of carbon steels, such as the X80 steel, it was shown that microgalvanic coupling occurs between ferrite (α-Fe) and cementite (Fe_3C) phases of the pearlite, leading to a selective dissolution of ferrite [102, 103]. This process leaves behind a porous cementite (Fe_3C) structure on the surface of the steel as observed in Figure 4.7.

3. Stability of the porous network:

Figures 4.7 to 4.9 showed the cross-sectional morphologies of the samples where the thickness of the porous layer varied considerably through changing the fluid flow velocity. After 96 h, the samples tested without flow showed an extensive porous network on the surface. The samples tested under 0.5 m/s fluid flow showed a thinner porous network combined with sparse $FeCO_3$ crystals. On the other hand, the samples tested under 1.0 m/s fluid flow showed no sign of the porous network, and only a thick $FeCO_3$ layer was visible. Which, as similarly observed

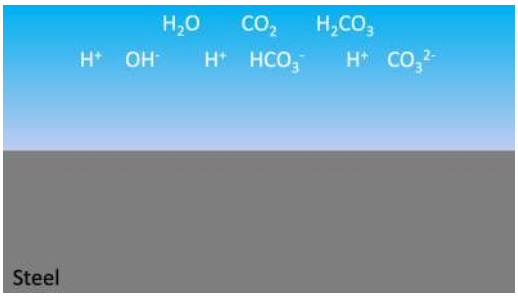

Step 1: Equilibria for CO_2 systems

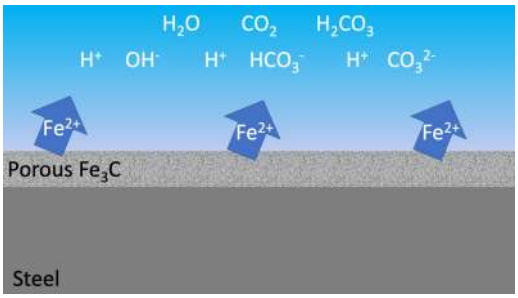

Step 2: Selective dissolution of ferrite

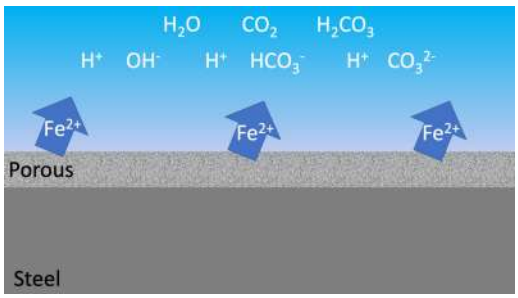

Step 3a: Flow bellow critical velocity

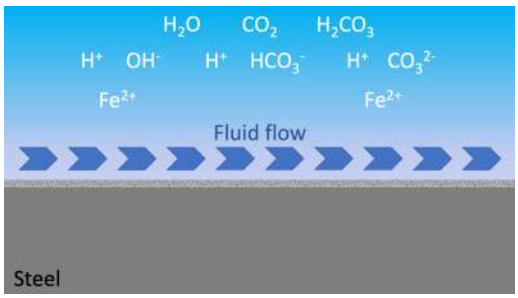

Step 3b: Flow above critical velocity

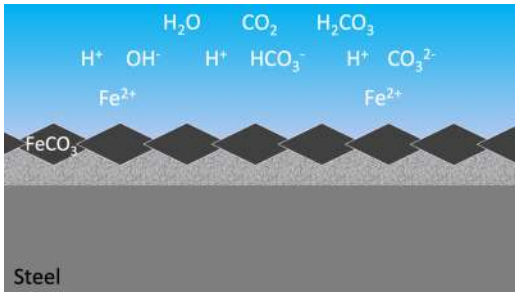

Step 4a: Corrosion film formation

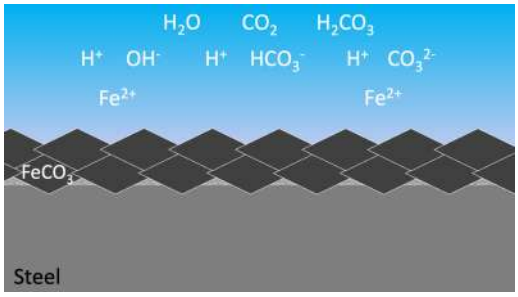

Step 4b: Corrosion film formation

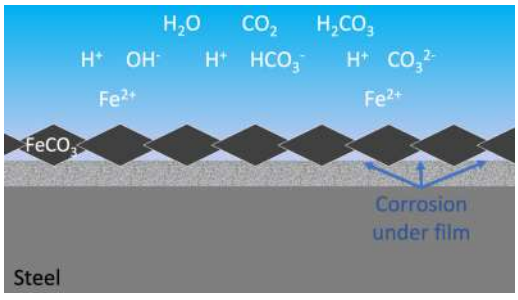

Step 5a: Undermining effect under film

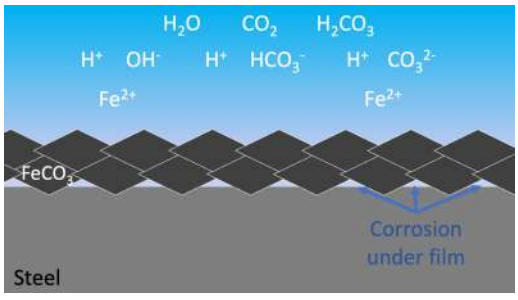

Step 5b: Undermining effect under film

Figure 4.14: CO_2 corrosion mechanism

by Bonaventura et al. [104], indicate that above a certain critical fluid velocity the porous and brittle layer can be removed from the surface by the influence of the fluid flow. This study has demonstrated that the porous $FeCO_3$ layer was partially removed when the sample was exposed to a 0.5 m/s flow velocity, and fully removed when the sample was exposed to a 1.0 m/s flow velocity.

4. Corrosion product film formation:

Results indicate that the main by-product in the corrosion of carbon steel in presence of only CO_2 is the precipitation of iron carbonate ($FeCO_3$) crystals on the surface. Evidenced by the peaks associated with the corrosion products of the samples exposed to the brine without Ca^{2+} being aligned with the $FeCO_3$ peaks from the literature, as shown in Figure 4.1.

As the corrosion process progresses, the electrochemical reactions happening at the surface releases Fe^{2+} into the solution. Gradually, the solution that already contains HCO_3^- and CO_3^{2-} from the CO_2 dissolving in water, becomes saturated with Fe^{2+} and ultimately, when supersaturation is reached, the precipitation of $FeCO_3$ becomes thermodynamically favourable [105].

Once the $FeCO_3$ crystals precipitate on the surface, the Fe^{2+} concentration in the bulk solution decreases. For lower saturation ratios (SS_{FeCO_3} close to 1) crystal growth is more favourable than the nucleation. Nucleation is then followed by crystal growth, which reduces the rate of precipitation. When relative supersaturation is high, nucleation dominates and a nano-crystalline or even amorphous film can develop. [106]

The addition of Ca^{2+} was shown to result in the $FeCO_3$ peaks position shifting to lower values of 2Θ with increasing Ca^{2+} addition. Given that $FeCO_3$ and $CaCO_3$ share a hexagonal lattice structure, the introduction of Ca into $FeCO_3$ matrix increases in the inter-planar spacing, that therefore, shifts the peaks position associated with those crystalline planes towards lower values of 2Θ. Based on this, Equation 3.4 can be used to calculate the mole fraction of Ca within the mixed iron-calcium carbonate based on the shift in the (104) peak as shown in Figure 4.15. Confirming not only the co-precipitation of $FeCO_3$ and $CaCO_3$ after 96 h of exposure, but also that the ratio of carbonates in the film is influenced by the brine composition.

It also evidenced a slight increase in $CaCO_3$ mole fraction in the corrosion product for increased fluid flows (from 5.7 to 9.5 and 17.7 to 25.6 % $CaCO_3$ when exposed to 1000 and 5000 ppm Ca^{2+} brines, respectively). Which may be partly attributed to the increased mass transfer rate at higher flow velocities. However, further evidence is required to back up this hypothesis.

5. Undermining effect under film:

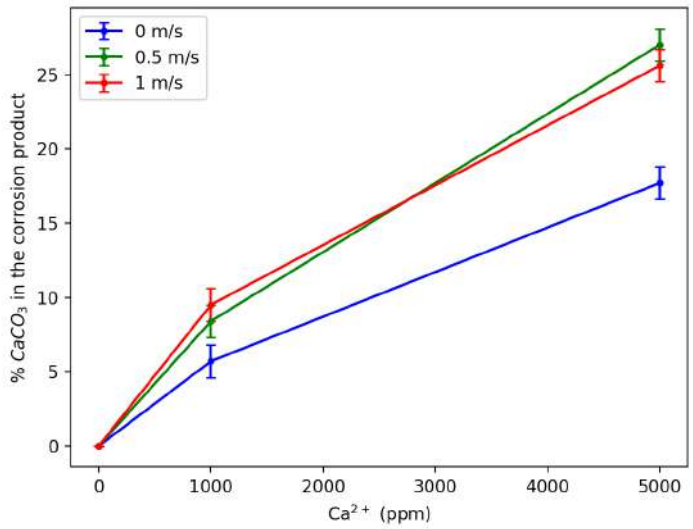

Figure 4.15: Variation of the $CaCO_3$ content in the corrosion product with increasing Ca^{2+} content in the brine and fluid flow.

Even though the $FeCO_3$ layers is seen as diffusion barrier to species involved in the cathodic reaction, which reduces the corrosion rate. It doesn't have the characteristics of a passive film, so the corrosion process can continue under the film, but at a slower pace. This continuously create a void between the film and the steel surface, a process commonly known as "film undermining". It happens when the corrosion rate exceeds the film precipitation rate. [101]

4.1.4.2 Protectiveness of corrosion product films

Previous authors have linked the reduction in corrosion rate over time in these environments to the formation of dense crystalline $FeCO_3$ layers capable of blocking active sites on the surface of the sample and acting as a diffusion barrier to species involved in the cathodic reaction. This layer can protect sample surface, by reducing the rate of the electrochemical reactions taking place on the surface, reducing the corrosion rate.

However, upon examining the electrochemical properties of corrosion scales (Figure 4.13), the corrosion rate was shown to decrease even in the presence of the presence of a porous plus a thin amorphous layer on the surface when compared to the non-corroded sample, although, being far less protective than the dense $Fe_xCa_yCO_3$ film.

The values calculated from the electrochemical measurements can't be readily compared to those measured using mass loss technique, because: (i) the electrochemical measurements were carried out under different thermodynamical condition compared to the condition where the corrosion scales were formed, and also (ii)

because the data obtained from mass loss tests are an average for the whole test period, while the electrochemical measurements show instantaneous values at the end of the test period. But both results may indicate the trend of how the corrosion rate changes over time.

Figure 4.16 compares the corrosion rates obtained by mass loss and electrochemical measurements methods. Both measurements reveal a decrease in corrosion rate for higher Ca^{2+} content, indicating that the corrosion scale formed in brines containing Ca^{2+} can be more protective. They show a strong correlation between both measurements, as 0.993, 0.833, 0.984 and 0.974 for the tests carried out without flow for 48 h, without flow for 96 h, 0.5 m/s fluid flow for 96 h and 1.0 m/s fluid flow for 96 h, respectively. Therefore, from the observations above, it was found that the addition of calcium promoted the growth of a mixed film iron-calcium carbonate ($Fe_xCa_{1-x}CO_3$), which was more protective than the pure iron carbonate $FeCO_3$ film.

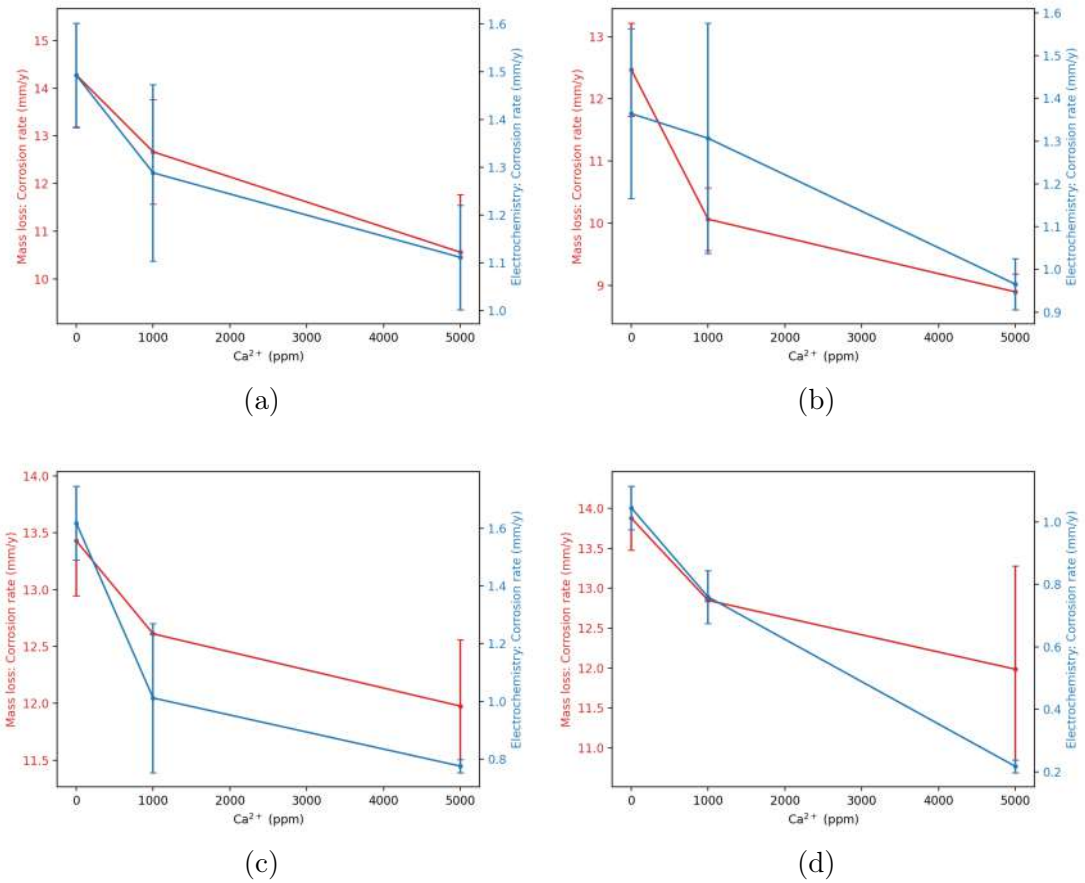

Figure 4.16: Comparison of corrosion rates measured by mass loss and electrochemical measurements as a function of the Ca^{2+} content in the brine for the tests carried out at 35 ^{o}C and 80 bar (a) without flow for 48 h, (b) without flow for 96 h, (c) 0.5 m/s fluid flow for 96 h and (d) 1.0 m/s fluid flow for 96 h

On the other hand when the same approach was used as a function of the fluid

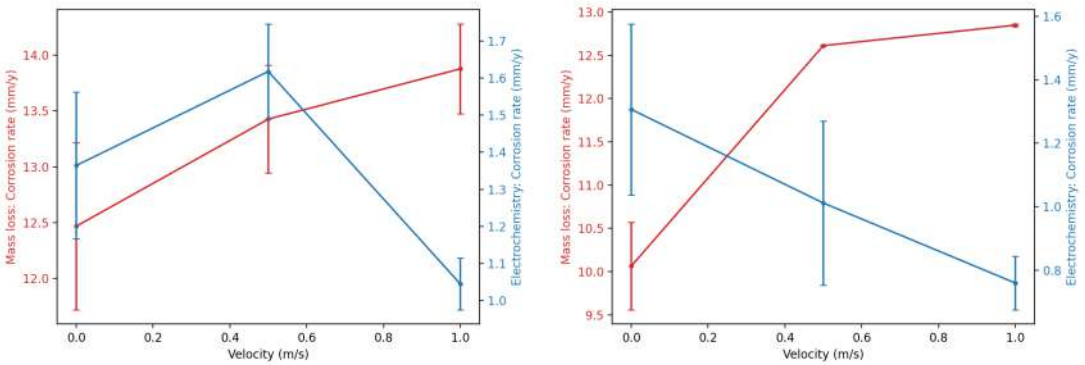

(a) (b)

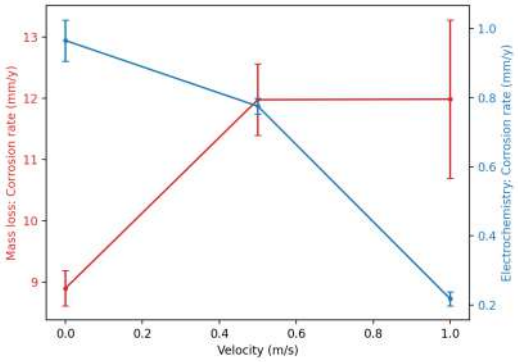

(c)

Figure 4.17: Comparison of corrosion rates measured by mass loss and electrochemical measurements for the tests carried out at 35 ^{o}C and 80 bar as a function of the fluid flow in a brine containing (a) 0, (b) 1000 and (c) 5000 ppm Ca^{2+} for 96 h.

flow velocity (Figure 4.17), it showed a weaker correlation of -0.377, -0.919 and -0.698 for the tests carried out in brines containing 0, 1000 and 5000 ppm Ca^{2+}. But most importantly all the correlation values exhibited a negative value, where the a more protective film (based on the electrochemical measurements) would correspond to a higher average corrosion rate throughout the whole test duration. This result implies that the enhanced mass transport induced by the fluid flow in first few hours made the corrosion rate so high that it shifted the average corrosion rate to higher values in comparison to the tests without flow. The latter would indicate that the mass loss measurements may not be an accurate reflection of the corrosion rate in the presence of a protective corrosion product scale, i.e., the corrosion rate under these conditions is over-estimated.

4.2 Samples exposed to water-saturated supercritical CO_2

This section focus on understanding the effect of the supercritical CO_2 stream flow on both general and localised corrosion of X80 steel in water-saturated CO_2 environments representative of those encountered in CO_2 transport in CCS. It focus on the role of the supercritical CO_2 stream flow and how this parameter influences the distribution and displacement of water droplets on the X80 steel surface. The overall aim of this section is to understand whether this parameter can enhance or reduce the overall corrosion in water-saturated CO_2 systems.

4.2.1 Mass loss measurements

Figure 4.18 shows the calculated corrosion rates determined from mass loss measurements in autoclave tests carried out at 35 ^{o}C, 80 bar and exposed to distinct supercritical CO_2 flow rate conditions for 48 h. No substantial difference in corrosion rate was observed between the samples of the tests carried out under static (with a fast rotation in the beginning) or dynamic conditions: 0.069 ± 0.017, 0.049 ± 0.018, 0.081 ± 0.021, 0.061 ± 0.006, 0.065 ± 0.020 mm/year for the tests carried out at 0, 0.15, 0.3, 0.5 and 1 m/s, respectively.

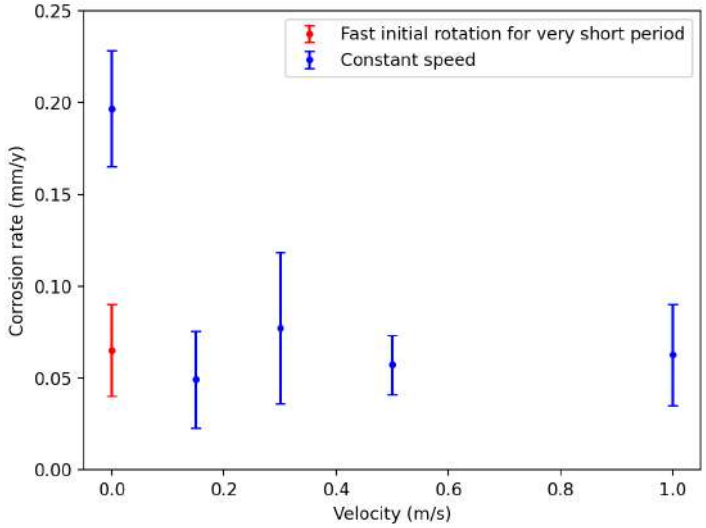

Figure 4.18: Variation of the corrosion rate of X80 steel immersed in water-saturated supercritical CO_2 at 35 ^{o}C and 80 bar after 48 h of immersion with increasing flow rate.

However, the corrosion rate measured under static condition without a fast rotation in the beginning was 3-4 times (0.207 mm/year) higher than those observed

under dynamic conditions. Assuming that the corrosion rate is proportional to the wet area [14, 29, 107], the corrosion rate measured indicates that the water wetting was more extensive on the samples tested in this condition. Morland and Svenningsen [82] reported that wetting of the surface may happen in the initial step of the test setup and can contribute to misleading corrosion rates.

In order to reduce the artefacts created during the initial step of the test setup, either due to accidental splashing of the water located at the bottom of the autoclave, caused by the injection of CO_2 or condensation that may have happened during decompression step of the purge to remove oxygen from the autoclave, it was decided to carry out the static test by letting it rotate at the maximum speed (600 rpm) for 1 h at the beginning of the test to displace these artefact water droplets that may eventually form during the test setup. In this particular test the measured corrosion rate was 0.069 mm/year, which, as mentioned previously, is analogous to those observed under dynamic conditions.

The similarities between the measured results indicate that under the tested conditions the forces acting on the water droplets volume due to the supercritical CO_2 flow are less than the minimum required to displace or affect the droplet size distribution on the surface. Therefore, it is likely that the average condensed water droplet size is much smaller than the critical size.

4.2.2 Surface analysis

4.2.2.1 Scanning electron microscopy

Figure 4.19 shows SEM images and photographs of the X80 steel samples exposed to water-saturated supercritical CO_2 at 35 ^{o}C, 80 bar and distinct velocity fields. The samples showed milder signs of discolouration over the entire surface (when compared to the samples exposed to CO_2-saturated water), in addition to darker localised patches of indicating areas where water had condensed on the steel surface.

SEM images shows that for both with or without initial rotation, the "no-flow" condition samples exhibited a surface almost fully covered by a thin layer of $FeCO_3$ crystals. However, as the rotating speed increases, the corrosion product does not form a continuous layer anymore, instead, thin patches can be observed, similar to morphologies previously observed in the literature [108, 109]. Upon closer inspection, the SEM images (Figure 4.20) revealed that the morphology of the corrosion product patches observed previously on X80 steel samples exposed to water-saturated supercritical CO_2 at 35 ^{o}C, 80 bar and distinct velocity fields for 48 h under different flow conditions consisted of stacked cubic $FeCO_3$ crystals.

The corrosion in supercritical CO_2 systems is expected to occur in the wetted

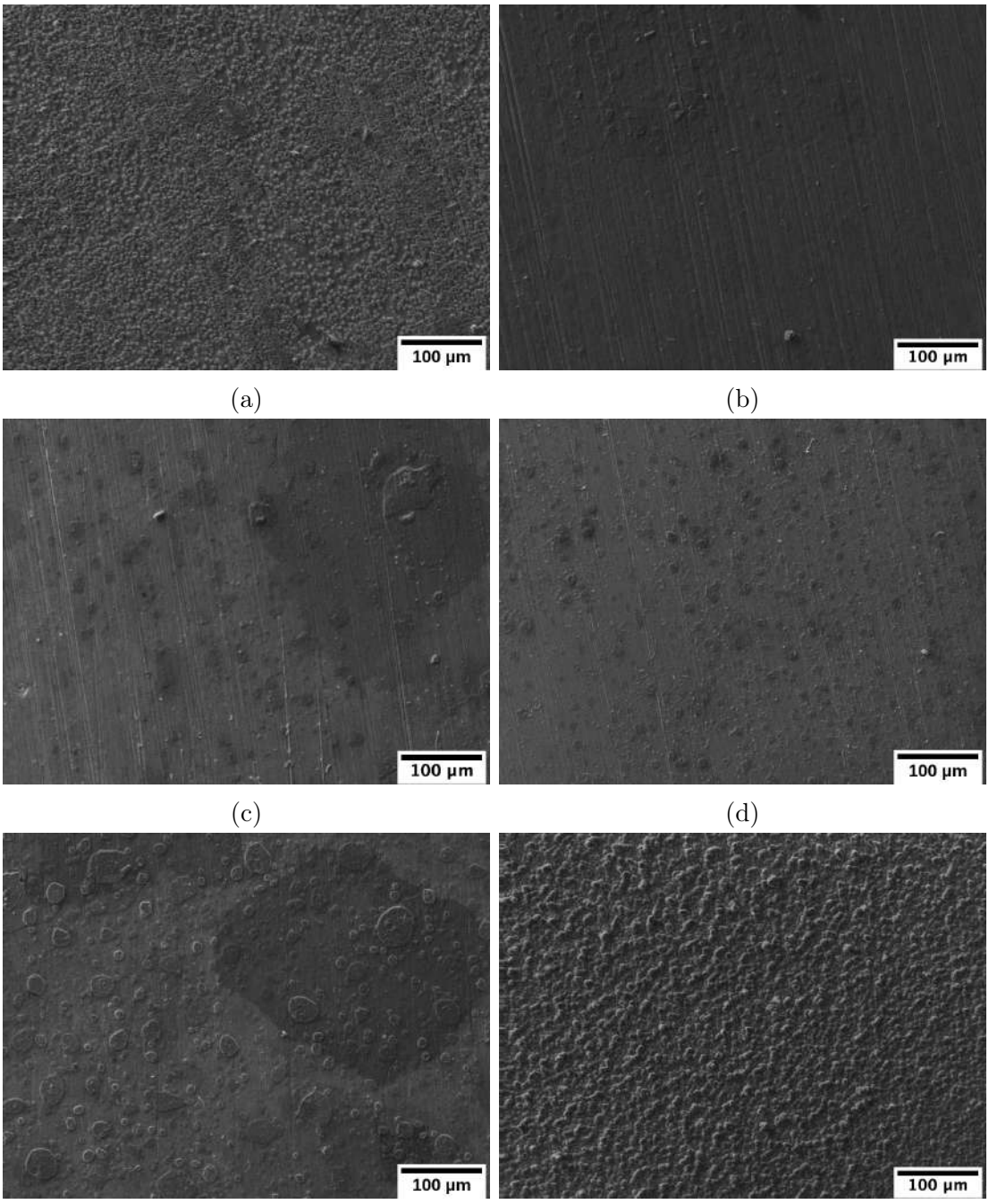

Figure 4.19: Surface morphologies of the corrosion products on X80 steel immersed in water-saturated supercritical CO_2 at 80 bar and 35 ^{o}C exposed to flow rates of (a) 0 m/s, (b) 0.15 m/s, (c) 0.3 m/s, (d) 0.5 m/s and (e) 1.0 m/s and (f) fast initial rotation for short period then 0 m/s for 48 h.

areas, leaving a footprint of corrosion features (patches) indicating the areas that were wetted during the tests. Therefore, it was reasonable to assume the area of those patches as the area of a hemispherical droplet that was present there during the test. Research into the displacement of liquid droplets on a surface by a shearing air flow was performed by Fan et al. [110]. Their research indicated three modes

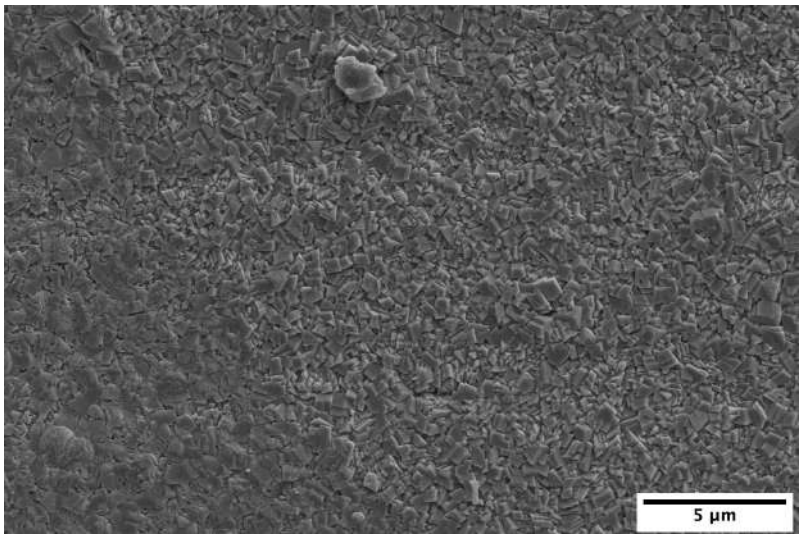

Figure 4.20: SEM morphology of the corrosion patches on X80 steel exposed to water-saturated supercritical CO_2 at 80 bar and 35 ^{o}C and a flow rate of 1.0 m/s for 48 h.

of droplet motion: (i) the droplets retaining the shape during motion, (ii) droplets developing a tail that moves at the same speed and (iii) the tail breaking up to form smaller droplets. The absence of signs of droplet tail found in the SEM images, indicates that if any motion is happening during the test, it is likely of type (i).

Due to the number of patches observed on each SEM image, ImageJ [86] version 1.53c software was used to process the images allowing a statistical analysis of the size distribution of corrosion patches on the sample surface. Figure 4.21 shows the droplet size distribution on the surface of the X80 steel samples exposed to water-saturated supercritical CO_2 at 35 ^{o}C, 80 bar and distinct velocity fields for 48 h. It shows that the flow velocity (up to 1 m/s) barely affected the size distribution of corrosion product scale on the surface of the samples, with the average being 7.7, 9.5, 9.2 and 9.7 µm for the samples exposed to flow rates of 0.15, 0.3, 0.5 and 1.0 m/s, respectively. It also shows an average droplet size two orders of magnitude smaller than the calculated critical size shown in Figure 3.12, indicating that the droplets are not expected to be displaced by the tested flow conditions and should remain stationary on the surface.

The sample exposed to a flow rate of 1 m/s for 48 h was selected for focused ion beam (FIB) sectioning for further analysis of its corrosion product chemical composition and morphology through the cross section. An energy dispersive X-ray (EDX) elemental analysis of this area was carried out, indicating that the film consisted mainly of iron, oxygen and carbon. The morphology and the elemental distributions of the corrosion product scale demonstrated that this layer consisted of iron carbonate ($FeCO_3$). This is consistent with previous observations in the literature from tests carried out in similar conditions [4, 46, 108, 109]. In addition, the $FeCO_3$

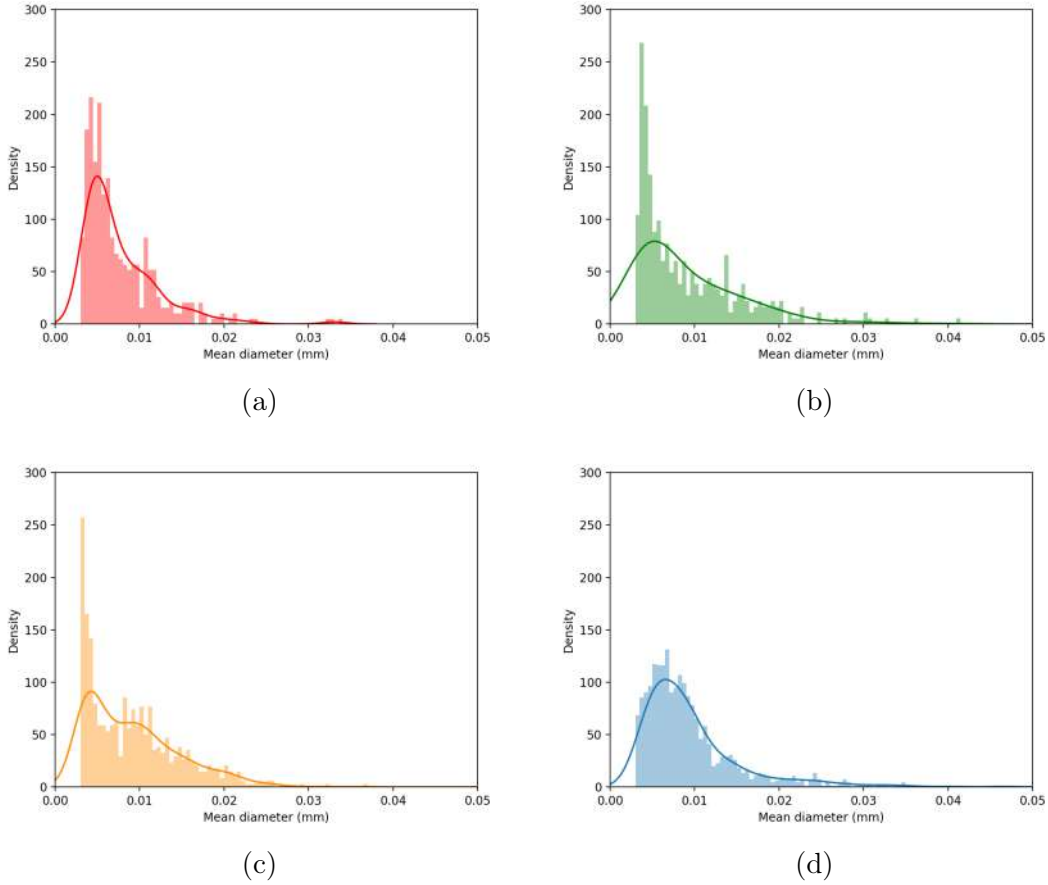

Figure 4.21: Droplet size distribution on the surface of the X80 samples exposed to water-saturated supercritical CO_2 at 80 bar and 35 ^{o}C and flow rates of (a) 0.15 m/s, (b) 0.3 m/s, (c) 0.5 m/s and (d) 1.0 m/s for 48 h.

layer was observed to have a thickness up to 5 μm.

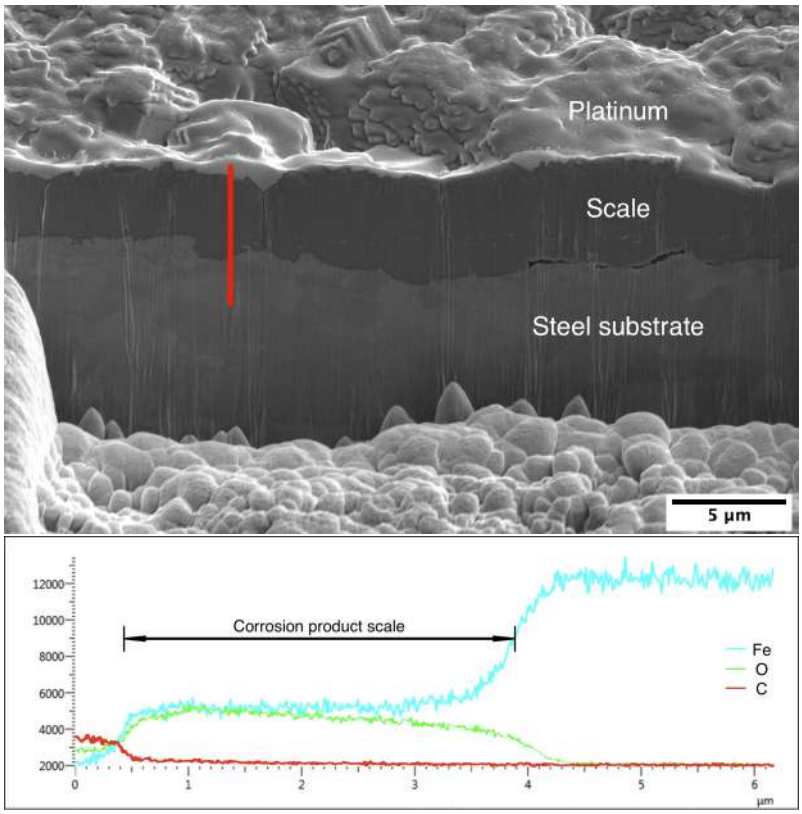

Figure 4.22: SEM image showing the location where the corrosion product layer was sliced using the FIB and an EDX analysis for the corrosion product layer area highlighted in red.

4.2.2.2 Surface profilometry

To supplement the surface analysis data, profilometry measurements were made to assess the extent of pitting. For each test one sample was selected for the scan, Figure 4.23 shows examples of the profilometry measurements taken from the samples exposed to the water-saturated supercritical CO_2 at 35 ^oC for 48 h under different flow conditions. For each of those samples, three $1 \times 1mm^2$ areas were randomly scanned on the surface. The pits in the combined three areas for each sample were measured, then the Equation 3.5 was used to assess the extent of the pitting damage, and the result is shown in Figure 4.24.

The results show that in water-saturated supercritical CO_2 at 80 bar and 35 ^oC, the average pitting rate was 0.59 ± 0.13, 0.55 ± 0.15, 0.59 ± 0.09, 0.76 ± 0.16 and 0.70 ± 0.17 mm/y for the tests carried out under 0, 0.15, 0.3, 0.5 and 1 m/s flow rates, respectively. The maximum pit depth measured were akin to the corrosion product layer thickness observed using FIB/SEM. However, the calculated pit penetration rates (Equation 3.5) are up to one order of magnitude higher than the uniform corrosion rates obtained through mass loss tests. Which suggests that the corrosion rates calculated from mass loss measurements may not be accurate in terms of assessing the true threat associated with the corrosion process. These

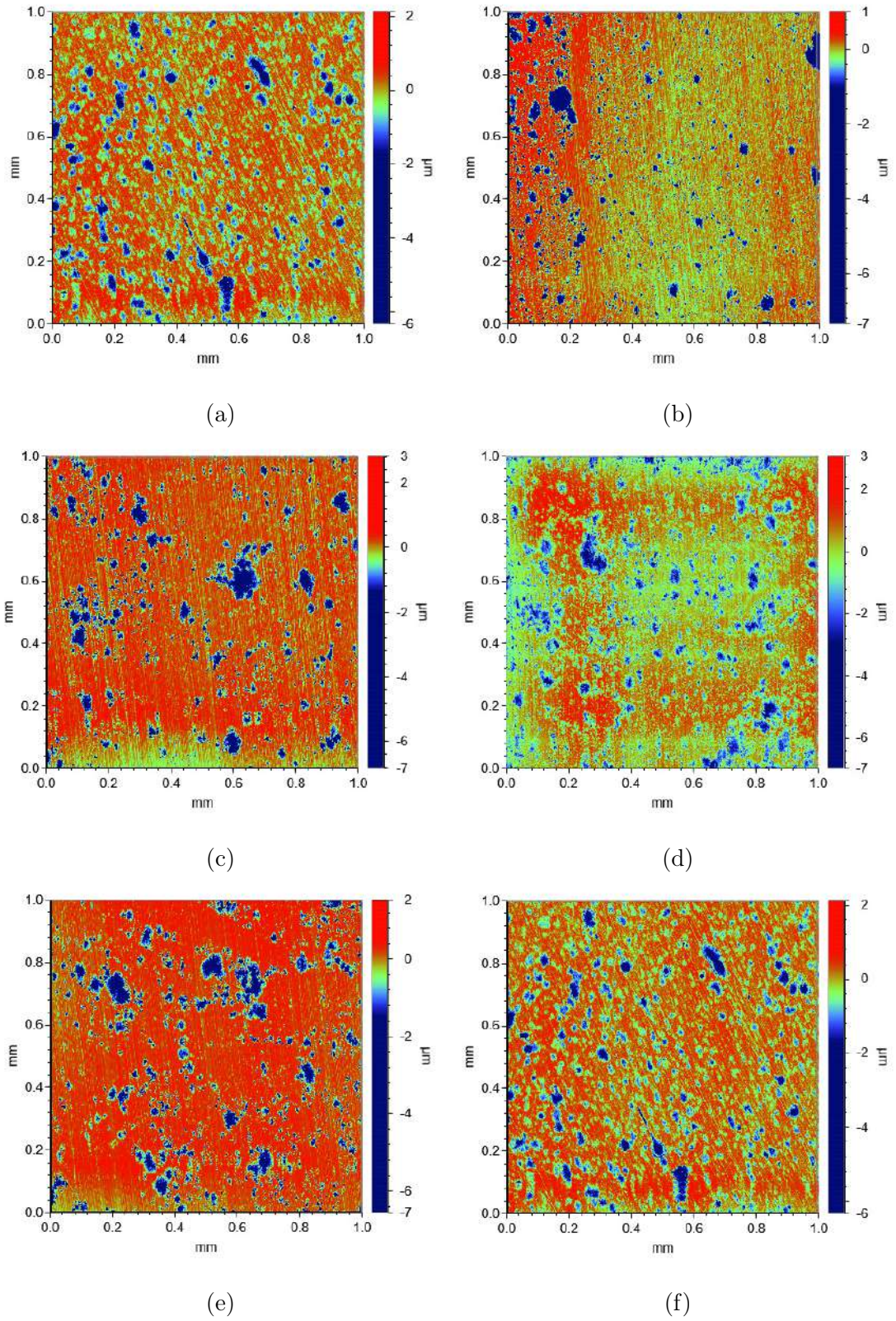

Figure 4.23: Surface profilometry of X80 steel exposed to water-saturated supercritical CO_2 at 80 bar and 35 ^{o}C and a flow rate of (a) 0 m/s, (b) 0.15, (c) 0.3, (d) 0.5 and (e) 1 m/s for 48 h and then cleaned with Clarke solution.

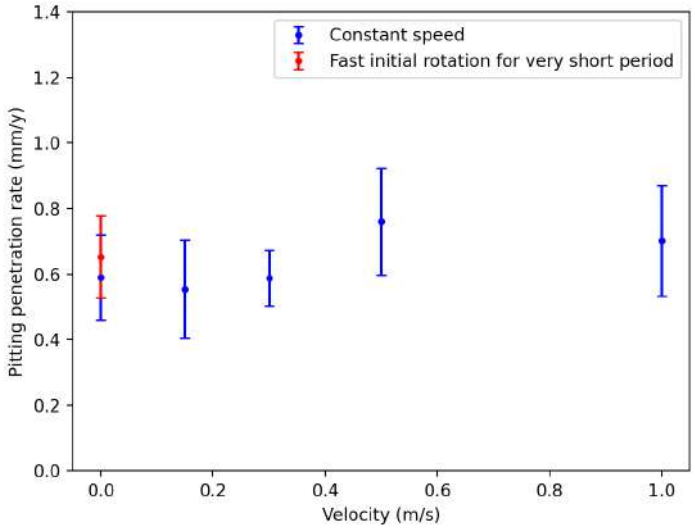

Figure 4.24: Variation of the pitting penetration rate of X80 steel exposed to water-saturated supercritical CO_2 at 80 bar, 35 ^{o}C and 48 h of immersion at different flow rates.

results are in accordance with the observations by Farelas et al. [42] and Hua et al. [111], who carried out tests in static conditions at 80 bar in liquid CO_2 at 25 ^{o}C and supercritical CO_2 at 35 ^{o}C, respectively. Both results presented in this work and the previous results from the literature indicate that mass loss tests may underestimate the risk represented by pitting corrosion of carbon steel in supercritical CO_2, even in the absence of impurities. But, despite that, it is also worth mentioning that the results indicate that, just as observed in the uniform corrosion measurements, the presence of a supercritical CO_2 flow has no significant effect on the pit penetration rate within the range studied.

4.2.3 Discussion

From the results presented in Section 4.2, the effect of supercritical CO_2 fluid flow on the corrosion rate have been studied. In supercritical CO_2 systems, the corrosion electrochemical reaction are the same as the ones in aqueous systems discussed in Section 4.1. However, the mechanism is substantially different to that encountered in aqueous systems, and more akin to corrosion in condensate/wet-gas systems. The supercritical CO_2 corrosion mechanisms of carbon steel under flow conditions is illustrated in Figure 4.25.

1. Surface wetting

Although dry CO_2 is not corrosive to steels, some CO_2 applications admit the presence of water, so the presence of it in small quantities is expected. In this

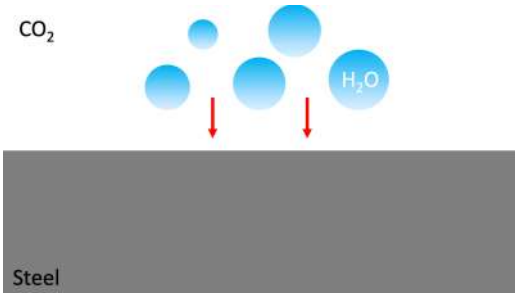

Step 1: Water-rich clusters impact or condensate on the steel surface

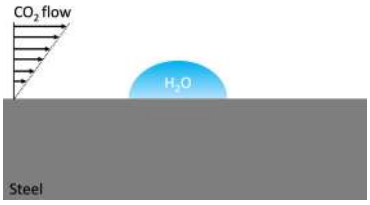

Step 2a: Droplet not affected by the gas flow

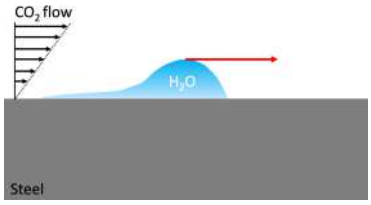

Step 2c: Droplet with tail that moves with it

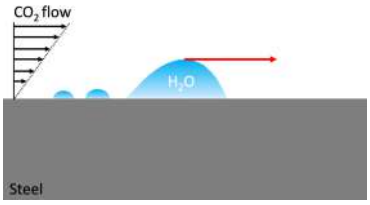

Step 2b: Droplet tail breaking up into smaller droplets

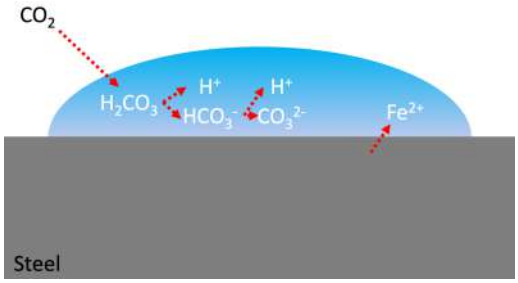

Step 3a: Electrochemical reaction inside the water droplet

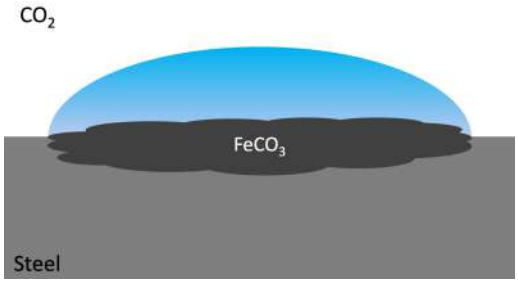

Step 3b: Corrosion product film formation in the wetted area

Figure 4.25: Supercritical CO_2 corrosion mechanism

scenario, the water can locally exceed the solubility limit and condense via a dropwise or film-wise mechanisms onto the steel surface. The condensation of water droplets in the supercritical CO_2 phase is still not fully understood and was beyond the scope of this study. However, some authors believe the water droplets condense directly on the steel surface similarly to atmospheric corrosion [112]. While others believe that a variation of temperature or pressure is required for the condensation [37]. A third option is related to the water condensing in the bulk supercritical CO_2 phase to create an emulsion where the droplets would eventually hit and adhere to the steel surface [14].

2. Water droplet displacement

Regardless of the water condensation mechanism operating, at any given time the steel samples inside the autoclave are expected to be covered by a distribution of water droplets with different sizes. Their size distribution is controlled by the nucleation and growth rate (condensation rate) and by the forces acting on them

(such as: gravity, drag and centrifugal forces), that may lead to their removal from the surface.

Zhang et al. [99] developed a mechanistic droplet formation model that allows the calculation of the lifetime, or critical radius of the droplets before they slide away, fall down or detach from a surface based on the forces acting on its volume. Figure 3.12 showed the calculated critical radius in each direction as a function of the supercritical CO_2 tangential velocity. The direction in which the critical radius (R_c) has the lowest value will control the motion mechanism. Under the experimental conditions considered (35 ^oC and 80 bar), the droplets that reach the critical size are expected to be displaced due to the gravity (fall down) at velocities bellow 0.34 m/s or due to the drag force (slide away) at velocities above 0.34 m/s but the water droplets smaller than the critical size shouldn't be affected.

Research into the displacement of liquid droplets on a surface by a shearing gas flow was performed by Fan et al. [110]. Their research indicated three modes of droplet motion that depends on the contact angle: (i) the droplets retaining the shape during motion, (ii) droplets developing a tail that moves at the same speed and (iii) the tail breaking up to form smaller droplets. In mode (i) the wetted area should stay the same, while in mode (ii) the water droplet is spread into a thin layer in the flow direction, increasing the wetted area, on the other hand, in mode (iii) the main water droplet would be removed from the surface and the total wetted area of the trail left behind should be smaller.

3. Corrosion process

The corrosion in such these systems is expected to be controlled by the electrochemical reaction occurring at the interface between the steel and the free water. Consequently, the corrosion rate measured would be influenced by the extent of the wetted area. Therefore, understanding the condensation and displacement of water droplets is very important for the prediction of the extent of corrosion in CO_2 injection wells.

The corrosion in supercritical CO_2 systems is expected to occur in the wetted areas, leaving a footprint of corrosion features (patches) indicating the areas that were wetted during the tests. Therefore, it was reasonable to assume the area of those patches as the area of a hemispherical droplet that was present there during the test.

Figure 4.21 showed that for the experimental conditions tested, the supercritical CO_2 flow velocity (up to 1 m/s) barely affected the size distribution of corrosion product patches on the surface of the samples. It also showed an average droplet size two orders of magnitude smaller than the calculated critical size shown in Figure 3.12, indicating that the droplets should remain stationary on the surface and the

wetted area wasn't modified. The average corrosion rate measured from mass loss for the same conditions shown in Figure 4.18 corroborates the assumption that it is controlled by the wetted area.

In spite of that, it is speculated that parameters that may affect either the water droplet size or the critical size may have an influence on the corrosion rates measured. Imposing conditions such as temperature gradient could favour water condensation [99], leading to the increasingly larger water droplet that may reach the critical size. Likewise, the critical water droplet size decreases for faster fluid flow rates, therefore smaller water droplets can be displaced. Both scenarios illustrate conditions where the influence of the supercritical CO_2 flow could be more easily noticed.

5. Conclusions

In this study the effect of the CO_2-saturated water and water-saturated supercritical CO_2 flow on the corrosion behaviour of X80 steel at a temperature of 35 ^oC and pressure of 80 bar, to simulate conditions that may occur in the CO_2 injection field conditions for CO_2-EOR, was investigated. It focused on the role of the fluid flow and brine chemistry and how these parameters influences the corrosion product scale morphology and its protectiveness in reducing the overall X80 steel corrosion rates.

In Section 4.1, the presence of a fluid flow velocity:

- Of 0.5 m/s partially removed the porous network from the surface, while 1.0 m/s fully removed the porous network from the surface, indicating a critical flow velocity that is able to damage or remove the brittle and porous layer.
- Favoured the formation of a crystalline carbonate layer on the surface of the X80 steel by removing the porous substrate and enhancing the carbonate precipitation.
- Increased the corrosion rate in the absence of a corrosion product film, but later favoured the precipitation of a dense and more protective crystalline carbonate layer.

In Section 4.1, the presence of Ca^{2+} in the brine:

- Favoured the precipitation of a mixed iron-calcium carbonate ($Fe_xCa_{1-x}CO_3$) film with increasingly calcium molar mass.
- Shifted the carbonate crystals morphology from prismatic crystals to a globular structure.
- Reduced the average corrosion rate, indicating that under the tested conditions the mixed iron-calcium carbonate scale offered better protectiveness to the carbon steel.
- Despite that, all the measured corrosion rates were very high, suggesting that a flooded pipeline scenario represents a potential concern for the integrity of carbon steel pipelines used in CO_2 transportation and injection conditions.

In Section 4.2, in the presence of a supercritical CO_2 fluid flow:

- The size of the corrosion patches on the surface of the samples, which were assumed as being the size of the condensed water droplets, were two orders of magnitude smaller than the calculated critical droplet size. Therefore, the drag force generated by the supercritical CO_2 flow was below the threshold required to displace the observed droplets size on the steel surface.
- A fluid flow up to 1 m/s did not enhance uniform general corrosion rate of X80 steel in water-saturated supercritical CO_2 environments, corroborating the assumption that it is controlled by the wetted area.
- The measured pitting penetration rates were up to one order of magnitude higher than the uniform corrosion rates obtained through mass loss tests, indicating that it may represent a potential concern for the integrity of carbon steel pipelines used in CO_2 transportation and injection conditions.

5.1 Recommendations for future studies

- Investigate the formation of free water in supercritical CO_2 systems.

There exists considerable controversy in the literature regarding the formation of free water in supercritical CO_2 systems. Some authors believe the water droplets condense directly on the steel surface similarly to atmospheric corrosion [112]. While others believe that a variation of temperature or pressure is required for the condensation [37]. A third option is related to the water condensing in the bulk supercritical CO_2 phase to create an emulsion where the droplets would eventually hit and adhere to the steel surface [14]. The corrosion in supercritical CO_2 systems has been associated with the formation of free water on the steel surface and is, by a certain extent proportional to the wetted area. Therefore, understanding the formation of free water is very important for the prediction of the extent of corrosion in CO_2 injection wells as well as developing techniques to mitigate it from happening.

- Further investigate the displacement of water droplets in conditions that favour larger droplets.

The next proposed study is to consider field conditions that may favour the condensation of water droplets, such as a temperature gradient. Akin to the condensation of water vapour at the upper side of the inner wall of the pipelines in Top of the Line Corrosion (TLC). This scenario can lead to increasingly larger water droplets that may reach the critical size, and the influence of the supercritical CO_2 flow could be more easily noticed.

References

[1] VEGA, L. F. "Perspectives on molecular modeling of supercritical fluids: From equations of state to molecular simulations. Recent advances, remaining challenges and opportunities", *The Journal of Supercritical Fluids*, v. 134, pp. 41–50, 2018. doi: 10.1016/j.supflu.2017.12.025.

[2] KNEZ, Z., MARKOCIC, E., LEITGEB, M., et al. "Industrial applications of supercritical fluids: A review", *Energy*, v. 77, pp. 235–243, 2014. doi: 10.1016/j.energy.2014.07.044.

[3] METZ, B., DAVIDSON, O., DE CONINCK, H., et al. *IPCC special report on carbon dioxide capture and storage. Prepared by Working Group III of the Intergovernmental Panel on Climate Change*. Relatório técnico, Cambridge University Press, 2005.

[4] HUA, Y., BARKER, R., NEVILLE, A. "The influence of SO_2 on the tolerable water content to avoid pipeline corrosion during the transportation of supercritical CO_2", *International Journal of Greenhouse Gas Control*, v. 37, pp. 412–423, 2015. doi: 10.1016/j.ijggc.2015.03.031.

[5] BARKER, R., HUA, Y., NEVILLE, A. "Internal corrosion of carbon steel pipelines for dense-phase CO_2 transport in carbon capture and storage (CCS)–a review", *International Materials Reviews*, v. 62, n. 1, pp. 1–31, 2017. doi: 10.1080/09506608.2016.1176306.

[6] JENSEN, M. D., SCHLASNER, S. M., SORENSEN, J. A., et al. "Operational flexibility of CO_2 transport and storage", *Energy Procedia*, v. 63, pp. 2715–2722, 2014. doi: 10.1016/j.egypro.2014.11.294.

[7] JOHNSEN, K., HOLT, H., HELLE, K., et al. *Mapping of potential HSE issues related to large-scale capture, transport and storage of* CO_2. Relatório técnico, Det Norsk Veritas, 2008.

[8] BOOT-HANDFORD, M. E., ABANADES, J. C., ANTHONY, E. J., et al. "Carbon capture and storage update", *Energy & Environmental Science*, v. 7, n. 1, pp. 130–189, 2014. doi: 10.1039/C3EE42350F.

[9] EDWARDS, R. W., CELIA, M. A. "Infrastructure to enable deployment of carbon capture, utilization, and storage in the United States", *Proceedings of the National Academy of Sciences*, v. 115, n. 38, pp. E8815–E8824, 2018. doi: 10.1073/pnas.1806504115.

[10] DNV. *Recommended Practice DNV-RP-J202; Design and Operation of* CO_2 *Pipelines*. Relatório técnico, Det Norske Veritas, 2010.

[11] SMITH, L., BILLINGHAM, M., BARRACLOUGH, C., et al. *Corrosion and Materials Selection in CCS Systems*. Relatório técnico, International Energy Agency Greenhouse Gas, 2010.

[12] MEYER, J. P. *Summary of Carbon Dioxide Enhanced Oil Recovery (*CO_2*-EOR) Injection Well Technology*. Relatório técnico, American Petroleum Institute, 2005.

[13] VERMA, M. K. *Fundamentals of carbon dioxide-enhanced oil recovery (*CO_2*-EOR): A supporting document of the assessment methodology for hydrocarbon recovery using* CO_2*-EOR associated with carbon sequestration*. Relatório técnico, US Department of the Interior, 2015.

[14] LIU, A. Q., BIAN, C., WANG, Z. M., et al. "Flow dependence of steel corrosion in supercritical CO_2 environments with different water concentrations", *Corrosion Science*, v. 134, pp. 149–161, 2018. doi: 10.1016/j.corsci.2018.02.027.

[15] "Risk analysis for CO_2 sequestration at enhanced oil recovery sites". `https://phys.org/news/2017-04-analysis-co2-sequestration-oil-recovery.html`, 2017. Accessed: 2019-09-30.

[16] HASSANI, S., VU, T. N., ROSLI, N. R., et al. "Wellbore integrity and corrosion of low alloy and stainless steels in high pressure CO_2 geologic storage environments: An experimental study", *International Journal of Greenhouse Gas Control*, v. 23, pp. 30–43, 2014. doi: 10.1016/j.ijggc.2014.01.016.

[17] WEI, L., GAO, K., LI, Q. "Corrosion of low alloy steel containing 0.5% chromium in supercritical CO_2-saturated brine and water-saturated supercritical CO_2 environments", *Applied Surface Science*, v. 440, pp. 524–534, 2018. doi: 10.1016/j.apsusc.2018.01.181.

[18] HUA, Y., BARKER, R., NEVILLE, A. "Comparison of corrosion behaviour for X-65 carbon steel in supercritical CO_2-saturated water and water-

saturated/unsaturated supercritical CO_2", *The Journal of Supercritical Fluids*, v. 97, pp. 224–237, 2015. doi: 10.1016/j.supflu.2014.12.005.

[19] SUN, C., WANG, Y., SUN, J., et al. "Effect of impurity on the corrosion behavior of X65 steel in water-saturated supercritical CO_2 system", *The Journal of Supercritical Fluids*, v. 116, pp. 70–82, 2016. doi: 10.1016/j.supflu.2016.05.006.

[20] HU, X., RAHEEM, K. A., NEVILLE, A., et al. "Effect of Different Types of Corrosion Films Formed in CO_2 Saturated Conditions on the In-Situ Corrosion of X65 Pipeline Steel Under Liquid-Solid Impingement". In: *CORROSION 2013*. NACE International, 2013.

[21] NEŠIĆ, S., POSTLETHWAITE, J., OLSEN, S. "An Electrochemical Model for Prediction of Corrosion of Mild Steel in Aqueous Carbon Dioxide Solutions", *Corrosion*, v. 52, n. 4, pp. 280–294, 1996. doi: 10.5006/1.3293640.

[22] HURLEN, T., GUNVALDSEN, S., TUNOLD, R., et al. "Effects of carbon dioxide on reactions at iron electrodes in aqueous salt solutions", *Journal of Electroanalytical Chemistry*, v. 180, n. 1-2, pp. 511–526, 1984. doi: 10.1016/0368-1874(84)83604-7.

[23] LI, W., BROWN, B., YOUNG, D., et al. "Investigation of pseudo-passivation of mild steel in CO_2 corrosion", *Corrosion*, v. 70, n. 3, pp. 294–302, 2014. doi: 10.5006/0950.

[24] LIU, Q. Y., MAO, L. J., ZHOU., S. W. "Effects of chloride content on CO_2 corrosion of carbon steel in simulated oil and gas well environments", *Corrosion Science*, v. 84, pp. 165–171, 2014. doi: 10.1016/j.corsci.2014.03.025.

[25] NEŠIĆ, S., LUNDE., L. "Carbon dioxide corrosion of carbon steel in two-phase flow", *Corrosion*, v. 50, n. 9, pp. 717–727, 1994. doi: 10.5006/1.3293548.

[26] PESSU, F., BARKER, R., NEVILLE., A. "Understanding pitting corrosion behaviour of X-65 (UNS K03014) carbon steel in CO_2 saturated environments: The temperature effect", *Corrosion*, 2014. doi: 10.5006/1338.

[27] SPYCHER, N., PRUESS, K. "CO_2-H_2O Mixtures in the Geological Sequestration of CO_2. II. Partitioning in Chloride Brines at 12–100 C and up to 600 bar", *Geochimica et Cosmochimica Acta*, v. 69, n. 13, pp. 3309–3320, 2005. doi: 10.1016/j.gca.2005.01.015.

[28] CHOI, Y. S., HASSANI, S., VU, T. N., et al. "Effect of H_2S on the corrosion behavior of pipeline steels in supercritical and liquid CO_2 environments", *Corrosion*, v. 72, n. 8, pp. 999–1009, 2016. doi: 10.5006/2026.

[29] XIANG, Y., LI, C., HESITAO, W., et al. "Understanding the pitting corrosion mechanism of pipeline steel in an impure supercritical CO_2 environment", *The Journal of Supercritical Fluids*, v. 138, pp. 132–142, 2018. doi: 10.1016/j.supflu.2018.04.009.

[30] WEI, L., ZHANG, Y., PANG, X., et al. "Corrosion behaviors of steels under supercritical CO_2 conditions", *Corrosion Reviews*, v. 13, n. 3-4, pp. 151–174, 2015. doi: 10.1515/corrrev-2014-0067.

[31] ZHANG, Y., PANG, X., QU, S., et al. "The relationship between fracture toughness of CO_2 corrosion scale and corrosion rate of X65 pipeline steel under supercritical CO_2 condition", *International Journal of Greenhouse Gas Control*, v. 5, n. 6, pp. 1643–1650, 2011. doi: 10.1016/j.ijggc.2011.09.011.

[32] DUGSTAD, A. "The importance of $FeCO_3$ supersaturation on the CO_2 corrosion of carbon steels". In: *Corrosion 92*. NACE International, 1992.

[33] INGHAM, B., KO, M., KEAR, G., et al. "In situ synchrotron X-ray diffraction study of surface scale formation during CO_2 corrosion of carbon steel at temperatures up to 90^{o}C", *Corrosion Science*, v. 52, n. 9, pp. 3052–3061, 2010. doi: 10.1016/j.corsci.2010.05.025.

[34] CHOI, Y. S., NEŠIĆ, S. "Corrosion behavior of carbon steel in supercritical CO_2-water environments". In: *Corrosion 2009*. NACE International, 2009.

[35] ARNE, D. "Fundamental aspects of CO_2 metal loss corrosion, Part I: mechanism". In: *CORROSION 2015*. NACE International, 2015.

[36] LI, W. F., ZHOU, Y. J., XUE, Y. "Corrosion behavior of 110S tube steel in environments of high H_2S and CO_2 content", *Journal of Iron and Steel Research International*, v. 19, n. 12, pp. 59–65, 2012. doi: 10.1016/S1006-706X(13)60033-3.

[37] CHOI, Y. S., NEŠIĆ, S. "Determining the corrosive potential of CO_2 transport pipeline in high pCO_2–water environments", *International Journal of Greenhouse Gas Control*, v. 5, n. 4, pp. 788–797, 2011. doi: 10.1016/j.ijggc.2010.11.008.

[38] CHOI, Y. S., FARELAS, F., NEŠIĆ, S., et al. "Corrosion behavior of deep water oil production tubing material under supercritical CO_2 environment: part

1—effect of pressure and temperature", *Corrosion*, v. 70, n. 1, pp. 38–47, 2014. doi: 10.5006/1019.

[39] DUGSTAD, A., MORLAND, B., CLAUSEN, S. "Corrosion of transport pipelines for CO_2 effect of water ingress", *Energy Procedia*, v. 4, pp. 3063–3070, 2011. doi: 10.1016/j.egypro.2011.02.218.

[40] CHOI, Y. S., NEŠIĆ, S., YOUNG, D. "Effect of impurities on the corrosion behavior of CO_2 transmission pipeline steel in supercritical CO_2-water environments", *Environmental science & technology*, v. 44, n. 23, pp. 9233–9238, 2010. doi: 10.1021/es102578c.

[41] HALSEID, M., DUGSTAD, A., MORLAND, B. "Corrosion and bulk phase reactions in CO_2 transport pipelines with impurities: review of recent published studies", *Energy Procedia*, v. 63, pp. 2557–2569, 2014. doi: 10.1016/j.egypro.2014.11.278.

[42] FARELAS, F., CHOI, Y. S., NEŠIĆ, S. "Effects of CO_2 phase change, SO_2 content and flow on the corrosion of CO_2 transmission pipeline steel". In: *CORROSION 2012*. NACE International, 2012.

[43] RUHL, A. S., KRANZMANN, A. "Investigation of corrosive effects of sulphur dioxide, oxygen and water vapour on pipeline steels", *International Journal of Greenhouse Gas Control*, v. 13, pp. 9–16, 2013. doi: 10.1016/j.ijggc.2012.12.007.

[44] RUHL, A. S., GOEBEL, A., KRANZMANN, A. "Corrosion behavior of various steels for compression, transport and injection for carbon capture and storage", *Energy Procedia*, v. 23, pp. 216–225, 2012. doi: 10.1016/j.egypro.2012.06.074.

[45] XIANG, Y., WANG, Z., LI, Z., et al. "Effect of exposure time on the corrosion rates of X70 steel in supercritical $CO_2/SO_2/O_2/H_2O$ environments", *Corrosion*, v. 69, n. 3, pp. 251–258, 2012. doi: 10.5006/0769.

[46] CHOI, Y. S., NEŠIĆ, S. "Effect of water content on the corrosion behavior of carbon steel in supercritical CO_2 phase with impurities". In: *Corrosion 2011*. NACE International, 2011.

[47] AYELLO, F., EVANS, K., THODLA, R., et al. "Effect of impurities on corrosion of steel in supercritical CO_2". In: *Corrosion 2010*. NACE International, 2010.

[48] DUGSTAD, A., HALSEID, M., MORLAND, B. "Effect of SO_2 and NO_2 on corrosion and solid formation in dense phase CO_2 pipelines", *Energy Procedia*, v. 37, pp. 2877–2887, 2013. doi: 10.1016/j.egypro.2013.06.173.

[49] BROWN, J., GRAVER, B., GULBRANDSEN, E., et al. "Update of DNV recommended practice RP-J202 with focus on CO_2 corrosion with impurities", *Energy Procedia*, v. 63, pp. 2432–2441, 2014. doi: 10.1016/j.egypro.2014.11.265.

[50] DUGSTAD, A., HALSEID, M., MORLAND, B. "Testing of CO_2 specifications with respect to corrosion and bulk phase reactions", *Energy Procedia*, v. 63, pp. 2547–2556, 2014. doi: 10.1016/j.egypro.2014.11.277.

[51] HUA, Y., SHAMSA, A., BARKER, R., et al. "Protectiveness, morphology and composition of corrosion products formed on carbon steel in the presence of Cl^-, CA^{2+} and Mg^{2+} in high pressure CO_2 environments", *Applied Surface Science*, v. 455, pp. 667–682, 2018. doi: 10.1016/j.apsusc.2018.05.140.

[52] TAVARES, L. M., DA COSTA, E. M., ANDRADE, J. J. D. O., et al. "Effect of calcium carbonate on low carbon steel corrosion behavior in saline CO_2 high pressure environments", *Applied Surface Science*, v. 359, pp. 143–152, 2015. doi: 10.1016/j.apsusc.2015.10.075.

[53] DING, C., GAO, K.-W., CHEN, C.-F. "Effect of Ca^{2+} on CO_2 corrosion properties of X65 pipeline steel", *International Journal of Minerals, Metallurgy and Materials*, v. 16, n. 6, pp. 661–666, 2009. doi: 10.1016/S1674-4799(10)60009-X.

[54] NAVABZADEH ESMAEELY, S., CHOI, Y.-S., YOUNG, D., et al. "Effect of Calcium on the Formation and Protectiveness of Iron Carbonate Layer in CO 2 Corrosion", *Corrosion*, v. 69, n. 9, pp. 912–920, 2013. doi: 10.5006/0942.

[55] ESMAEELY, S., YOUNG, D., BROWN, B., et al. "Effect of incorporation of calcium into iron carbonate protective layers in CO_2 corrosion of mild steel", *Corrosion*, v. 73, n. 3, pp. 238–246, 2017.

[56] SHAMSA, A., BARKER, R., HUA, Y., et al. "The role of Ca^{2+} ions on Ca/Fe carbonate products on X65 carbon steel in CO_2 corrosion environments at 80 and 150 ^{o}C", *Corrosion Science*, v. 156, pp. 58–70, 2019. doi: 10.1016/j.corsci.2019.05.006.

[57] NEŠIĆ, S. "Key issues related to modelling of internal corrosion of oil and gas pipelines–A review", *Corrosion Science*, v. 49, pp. 4308–4338, 2007. doi: 10.1016/j.corsci.2007.06.006.

[58] SCHMITT, G. "Fundamental aspects of CO_2 metal loss corrosion. Part II: Influence of different parameters on CO_2 corrosion mechanism". In: *CORROSION 2015*. NACE International, 2015.

[59] RUZIC, V., VEIDT, M., NEŠIC, S. ""Protective iron carbonate films—Part 1: Mechanical removal in single-phase aqueous flow", *Corrosion*, v. 62, n. 5, pp. 419–432, 2006. doi: 10.5006/1.3278279.

[60] LI, W., POTS, B. F. M., BROWN, B., et al. ""A direct measurement of wall shear stress in multiphase flow—Is it an important parameter in CO_2 corrosion of carbon steel pipelines?" *Corrosion Science*, v. 110, pp. 35–45, 2016. doi: 10.1016/j.corsci.2016.04.008.

[61] TANUPABRUNGSUN, T. *Thermodynamics and Kinetics of Carbon Dioxide Corrosion of Mild Steel at Elevated Temperatures*. Tese de Doutorado, Ohio University, 2013.

[62] COMSOL. *COMSOL Multiphysics® CFD User's Guide, version 5.4*. COMSOL Inc., Stockholm, Sweden, 2018.

[63] JOHNS, A. S. *Computational fluid dynamic modelling and optimisation of internal twist-drill coolant channel flow*. Tese de Doutorado, University of Leeds, 2015.

[64] STOKES, G. G. *On the effect of the internal friction of fluids on the motion of pendulums*. Cambridge, Pitt Press, 1851.

[65] TENNEKES, H., LUMLEY, J. L., LUMLEY, J. L. *A first course in turbulence*. Massachusetts, MIT Press, 1972.

[66] BATCHELOR, C. K., BATCHELOR, G. K. *An introduction to fluid dynamics*. Cambridge University Press, 2000.

[67] REYNOLDS, O. "On the Dynamical Theory of Incompressible Viscous Fluids and the Determination of the Criterion", *Philosophical Transactions of the Royal Society of London A*, v. 186, pp. 123–164, 1895. doi: 10.1098/rsta.1895.0004.

[68] BOUSSINESQ, J. *Théorie de l'écoulement tourbillonnant et tumultueux des liquides dans les lits rectilignes a grande section*. Gauthier-Villars, 1897.

[69] CHOU, P. Y. "On velocity correlations and the solutions of the equations of turbulent fluctuation", *Quarterly of Applied Mathematics*, v. 3, n. 1, pp. 38–54, 1945.

[70] LAUNDER, B. E., SHARMA, B. I. "Application of the energy-dissipation model of turbulence to the calculation of flow near a spinning disc", *Letters in heat and mass transfer*, v. 1, n. 2, pp. 131–137, 1974. doi: 10.1016/0094-4548(74)90150-7.

[71] "Modeling Turbulent Flows". `http://www.southampton.ac.uk/~nwb/lectures/GoodPracticeCFD/Articles/Turbulence_Notes_Fluent-v6.3.06.pdf`, 2006. Accessed: 2020-05-21.

[72] FREI, W. "Which Turbulence Model Should I Choose for My CFD Application?" `https://br.comsol.com/blogs/which-turbulence-model-should-choose-cfd-application/`, 2017. Accessed: 2020-05-21.

[73] KOLMOGOROV, A. N. "The equation of turbulent motion in an incompressible viscous flow", *Izv. Akad. Nauk. SSSR*, v. VI 1-2, 1942. doi: 10.4213/rm697.

[74] WILCOX, D. C. "Reassessment of the scale-determining equation for advanced turbulence models", *AIAA journal*, v. 26, n. 11, pp. 1299–1310, 1988. doi: 10.2514/3.10041.

[75] WILCOX, D. C. *Turbulence Modeling for CFD*. DCW Industries, 2006.

[76] LYU, P. "Simulating Turbulent Flow in COMSOL Multiphysics®". `https://www.comsol.com/video/simulating-turbulent-flow-in-comsol-multiphysics`, 2016. Accessed: 2020-05-21.

[77] "Law of the wall". `https://en.wikipedia.org/wiki/Law_of_the_wall`, 2021. Accessed: 2020-05-21.

[78] BAKKER, A. "Lecture 11 – Boundary Layers and Separation Applied Computational Fluid". `http://www.bakker.org/dartmouth06/engs150/11-bl.pdf`. Accessed: 2020-05-21.

[79] LIU, F. "A Thorough Description Of How Wall Functions Are Implemented In OpenFOAM". In: *Proceedings of CFD with OpenSource Software*, 2016. Accessed: 2020-05-21.

[80] NIU, J., QI, L. H., LIU, Y. L., et al. "Tempering microstructure and mechanical properties of pipeline steel X80", *Transactions of Nonferrous Metals Society of China (English Edition)*, v. 19, n. 3, pp. s573–s578, 2009. doi: 10.1016/S1003-6326(10)60111-2.

[81] XUE, H. B., CHENG, Y. F. "Characterization of inclusions of X80 pipeline steel and its correlation with hydrogen-induced cracking", *Corrosion Science*, v. 53, n. 4, pp. 1201–1208, 2011. doi: 10.1016/j.corsci.2010.12.011.

[82] MORLAND, B. H., SVENNINGSEN, G. "Pitfalls and Artefacts in Corrosion Experiments with Dense Phase CO_2". In: *CORROSION 2021*, n. 2027, NACE Corrosion, 2021.

[83] ASTM. *G1 - Standard Practice for Preparing, Cleaning, and Evaluating Corrosion Test Specimens*. American Society for Testing and Materials, 2003.

[84] NING, J., ZHENG, Y., BROWN, B., et al. "A thermodynamic model for the prediction of mild steel corrosion products in an aqueous hydrogen sulfide environment", *Corrosion*, v. 71, n. 8, pp. 945–960, 2015. doi: 10.5006/1566.

[85] ASTM. *G102 - Standard Practice for Calculation of Corrosion Rates and Related Information from Electrochemical Measurements*. American Society for Testing and Materials, 2015.

[86] SCHINDELIN, J., ARGANDA-CARRERAS, I., FRISE, E., et al. "Fiji: An open-source platform for biological-image analysis", *Nature Methods*, v. 9, n. 7, pp. 676–682, 2012. doi: 10.1038/nmeth.2019.

[87] HUA, Y. *An Experimental Study of Corrosion for Long Distance Carbon Transportation Pipelines*. Tese de Doutorado, University of Leeds, 2015.

[88] WEI, L., PANG, X., GAO, K. "Effect of small amount of H_2S on the corrosion behavior of carbon steel in the dynamic supercritical CO_2 environments", *Corrosion Science*, v. 103, n. 2, pp. 132–144, 2016. doi: 10.1016/j.corsci.2015.11.009.

[89] BAHADORI, A., VUTHALURU, H. B., MOKHATAB, S. "New correlations predict aqueous solubility and density of carbon dioxide", *International Journal of Greenhouse Gas Control*, v. 3, n. 4, pp. 474–480, 2009. doi: 10.1016/j.ijggc.2009.01.003.

[90] HEIDARYAN, E., HATAMI, T., RAHIMI, M., et al. "Viscosity of pure carbon dioxide at supercritical region: Measurement and correlation approach", *Journal of Supercritical Fluids*, v. 56, n. 2, pp. 144–151, 2011. doi: 10.1016/j.supflu.2010.12.006.

[91] KUMAR, A., PACHECO, J., LING, S., et al. "Effects of Autoclave Designs on Shear Stress and Flow Pattern". In: *CORROSION 2013*. NACE International, 2013.

[92] RUNSTEDTLER, A., HUANG, J., BOISVERT, P., et al. "Parametric Wall Shear Stress Characterization of the Rotating Cage Test Method", *Corrosion*, v. 75, n. 6, pp. 580–586, 2019. doi: 10.5006/2864.

[93] NEŠIĆ, S., KAHYARIAN, A., CHOI, Y. S. "Implementation of a comprehensive mechanistic prediction model of mild steel corrosion in multiphase oil and gas pipelines", *Corrosion*, v. 75, n. 3, pp. 274–291, 2019. doi: 10.5006/3093.

[94] YABUKI, A. "Mass Transfer Equation and Hydrodynamic Effects in Erosion-Corrosion", *Advanced Topics in Mass Transfer*, 2011. doi: 10.5772/13929.

[95] GAO, K., YU, F., PANG, X., et al. "Mechanical properties of CO_2 corrosion product scales and their relationship to corrosion rates", *Corrosion Science*, v. 50, n. 10, pp. 2796–2803, 2008. doi: 10.1016/j.corsci.2008.07.016.

[96] SCHMITT, G. A., GUDDE, T., STROBEL-EFFERTZ, E. "Fracture Mechanical Properties of CO_2 Corrosion Product Scales and Their Relation to Localized Corrosion". In: *CORROSION 2003*, NACE Corrosion, 03 1996.

[97] SCHMITT, G. A., MUELLER, M., PAPENFUSS, M., et al. "Understanding Localized CO_2 Corrosion of Carbon Steel from Physical Properties of Iron Carbonate Scales". In: *CORROSION 99*, NACE Corrosion, 04 1999.

[98] SCHMITT, G. A., MUELLER, M. "Critical wall shear stresses in CO_2 corrosion of carbon steel". In: *CORROSION 99*. NACE International, 1999.

[99] ZHANG, Z., HINKSON, D., SINGER, M., et al. "A mechanistic model of top-of-the-line corrosion", *Corrosion*, v. 63, n. 11, pp. 1051–1062, 2007. doi: 10.5006/1.3278321.

[100] CUI, G., YANG, Z., LIU, J., et al. "A comprehensive review of metal corrosion in a supercritical CO_2 environment", *International Journal of Greenhouse Gas Control*, v. 90, n. 66, 2019. doi: 10.1016/j.ijggc.2019.102814.

[101] NEŠIĆ, S., LEE, K. L. "A mechanistic model for carbon dioxide corrosion of mild steel in the presence of protective iron carbonate films - Part 3: Film growth model", *Corrosion*, v. 59, n. 7, pp. 616–628, 2003. doi: 10.5006/1.3277592.

[102] SÁNCHEZ, J., FULLEA, J., ANDRADE, C., et al. "AFM study of the early corrosion of a high strength steel in a diluted sodium chloride solution", *Corrosion Science*, v. 50, n. 7, pp. 1820–1824, 2008. doi: 10.1016/j.corsci.2008.03.013.

[103] MURASE, Y., MASUDA, H., KATAYAMA, H. "Corrosion Resistance of Finer/Coarser Pearlitic Structures of Carbon Steel", *Journal of The Electrochemical Society*, v. 168, n. 4, 2021. doi: 10.1149/1945-7111/abf185.

[104] BONAVENTURA, M. D., BROWN, B., NEŠIĆ, S., et al. "Removal of Iron Carbide in Turbulent Flow Conditions and Influence on Iron Carbonate Formation in Aqueous CO_2 Corrosion of Mild Steel". In: *CORROSION 2020*, n. 15148, NACE Corrosion, pp. 1–13, 2020.

[105] SUN, W., NEŠIĆ, S. "Kinetics of corrosion layer formation: Part 1 - Iron carbonate layers in carbon dioxide corrosion", *Corrosion*, v. 64, n. 4, pp. 334–346, 2008. doi: 10.5006/1.3278477.

[106] BURKLE, D. P. *Understanding the Formation of Protective* $FeCO_3$ *on to Carbon Steel Pipelines during* CO_2 *Corrosion*. Tese de Doutorado, University of Leeds, 2017.

[107] JIANG, X., QU, D., SONG, X., et al. "Critical water content for corrosion of X65 mild steel in gaseous, liquid and supercritical CO_2 stream", *International Journal of Greenhouse Gas Control*, v. 85, pp. 11–22, 2019. doi: 10.1016/j.ijggc.2019.03.020.

[108] HUA, Y., BARKER, R., NEVILLE, A. "Effect of temperature on the critical water content for general and localised corrosion of X65 carbon steel in the transport of supercritical CO_2", *International Journal of Greenhouse Gas Control*, v. 31, pp. 48–60, 2014. doi: 10.1016/j.ijggc.2014.09.026.

[109] HUA, Y., BARKER, R., CHARPENTIER, T., et al. "Relating iron carbonate morphology to corrosion characteristics for water-saturated supercritical CO_2 systems", *Journal of Supercritical Fluids*, v. 98, pp. 183–193, 2015. doi: 10.1016/j.supflu.2014.12.009.

[110] FAN, J., WILSON, M. C., KAPUR, N. "Displacement of liquid droplets on a surface by a shearing air flow", *Journal of Colloid and Interface Science*, v. 356, n. 1, pp. 286–292, 2011. doi: 10.1016/j.jcis.2010.12.087.

[111] HUA, Y., BARKER, R., NEVILLE, A. "Understanding the influence of SO2 and O2 on the corrosion of carbon steel in water-saturated supercritical CO_2", *Corrosion*, v. 71, n. 5, pp. 667–683, 2015. doi: 10.5006/1504.

[112] XIANG, Y., WANG, Z., XU, M., et al. "A mechanistic model for pipeline steel corrosion in supercritical CO_2 – SO_2 – O_2 – H_2O environments", *Journal of Supercritical Fluids*, v. 82, pp. 1–12, 2013. doi: 10.1016/j.supflu.2013.05.016.